Investigation of fluidized bed systems using coupled DEM-CFD framework

Surya Deb

Dissertation submitted to the faculty of the Virginia Polytechnic Institute and State University in partial fulfillment of the requirements for the degree of

Doctor of Philosophy
In
Mechanical Engineering

Danesh K. Tafti, Chair
Brian Lattimer
Francine Battaglia
Mark R. Paul
Christopher Roy

October 29th 2013
Blacksburg, Virginia

Keywords: Computational fluid dynamics (CFD), Discrete element method, Multiphase flows, Fluidized beds, Void fraction, Solid velocity, Granular temperature

Investigation of fluidized bed systems using coupled DEM-CFD framework

Surya Deb

ABSTRACT

Fluidized beds have widespread industrial applications ranging from chemical industries to power plants. The flow inside a fluidized bed system consists of two main phases, a particle phase and the fluid phase. The two phases are strongly coupled to each other through various forces like drag and pressure. Capturing this multiphase phenomenon requires modeling strategies that possess good fidelity over a range of scales. Discrete Element Modeling (DEM) coupled with Computational Fluid Dynamics (CFD) provides a good platform to analyze the complex coupled multiphase hydrodynamics inside fluidized bed systems. Conventional DEM-CFD framework suffers from contradictory spatial resolution requirements for the particle and fluid phases, respectively. This prevents the conventional DEM-CFD method to be applied to geometries that have features comparable to the particle diameter of the solid phase. The novelty of this work lies in the development and validation of a two-grid formulation that removes the resolution restrictions of the conventional DEM-CFD framework. The results obtained from this new framework agree reasonably well with the experiments showing the capability of the new scheme to simulate conditions not possible with conventional DEM-CFD framework. In addition, this research also focuses on performing both 2D and 3D jetting fluidized bed simulations having millions of particles; validate/compare results with experiments and to perform heat transfer studies in a jetting fluidized bed system. The results suggest convective and diffusive mixing for a single jet at higher superficial velocity to be better than the mixing obtained in a multiple jet framework. The comparison with experimental results obtained in a multiple jetting setup shows that a 2D simulation captures the essential jet characteristics near the distributor plate reasonably well while a 3D simulation is needed to capture proper bubble dynamics near the freeboard of the bed. These results give insight into the detailed dynamics of fluidized bed systems and provide a foundation for a better design of these systems.

Dedicated to my family

ACKNOWLEDGEMENTS

First and foremost, I would like to thank my advisor Dr. Danesh Tafti, W. S. Cross Professor of Mechanical Engineering, to whom I owe my deepest gratitude. Dr. Tafti motivated and supported me in overcoming all the obstacles in the completion of this research work. I would like to thank my PhD Committee Dr. Brian Lattimer, Dr. Francine Battaglia, Dr. Mark Paul, and Dr. Christopher Roy for their support towards the completion of my research goals.

I would like to thank the Institute for Critical Technology and Applied Sciences (ICTAS) for supporting part of this work. The support of HPC resources of TeraGrid (now XSEDE) and ARC at Virginia Tech is greatly appreciated.

I would also like to thank the staff of the Mechanical Engineering Department for their help during the course of this work. I also thank my lab-mates and friends for the continuous encouragement, intriguing discussions and moral support.

Last but not the least; I would like to thank my family for offering me unconditional support in completing this work.

TABLE OF CONTENTS

LIST OF FIGURES

LIST OF TABLES

NOMENCLATURE

C_D Coefficient of drag.

$\vec{F}_p$ Total force acting on particle due to collision (N).

I_p Moment of Inertia of a particle (kg.m^2).

$\vec{T}_p$ Total torque acting on a particle (Nm).

U_{mf} Minimum Fluidization Velocity (ms^{-1}).

V_p Volume of a particle (m^3).

$\vec{g}$ Acceleration due to gravity (ms^{-2}).

m_p Mass of a particle (kg).

k_n Spring constant along normal direction (Nm^{-1}).

k_t Spring constant along tangential direction (Nm^{-1}).

p Fluid pressure (Nm^{-2}).

r_p Radius of particle (m).

$\vec{u}$ Fluid velocity (ms^{-1}).

$\vec{v}_p$ Particle velocity (ms^{-1}).

$\vec{v}_{pq}$ Relative velocity between particles p and q (ms^{-1}).

$\vec{x}_p$ Particle position (m).

ε Void Fraction.

μ Coefficient of friction.

β Interphase momentum exchange coefficient (Nsm^{-4}).

ε_s Solid Fraction.

μ_g Fluid viscosity (Nsm^{-2}).

ρ_g Fluid density (kgm^{-3}).

ρ_p Particle density (kgm^{-3}).

$\vec{\omega}_p$ Particle rotational velocity (s^{-1}).

$\vec{\tau}_g$ Fluid shear stress (Nm^{-2}).

$\vec{\delta}_{n,pq}$ Normal overlap between particles p and q (m).

$\vec{\delta}_{t,pq}$ Tangential overlap between particles p and q (m).

η_n Viscous damping along normal direction (Nsm^{-1}).

η_t Viscous damping along tangential direction (Nsm^{-1}).

Chapter 1 Introduction

Brief Overview

Fluidized beds have wide spread industrial applications. They are mainly used for their efficient mixing properties. Some of the varied applications of a fluidized bed include coal gasification, particle coating, heat exchange and gas-solid reactions (Kunii and Levenspiel, 1991). Massive commercialization of fluidized beds dates back to the 1940's by the petroleum industry to aid in the cracking of heavy hydrocarbons to fuel oil (Swarbrick J, 1992). In a fluidized bed, hot gas is passed through a bed of stationary particles. With a low flow rate, the gas starts percolating through the particle gaps. As the flow rate is increased, the gas starts moving the particles from their initial equilibrium positions. The particles start to fluidize and with further increase in flow rate, the particles start to move up the bed. This is known as an expanded bed.

Hydrodynamics of fluidized beds have been studied from as early as the 1960's. The motion of two different phases in a fluidized bed is complicated because it is transient and unknown. A proper understanding of the interactions exist only for limited conditions (Gilbertson and Yates, 1996). Resolving the two phase problem by treating each phase separately and using boundary and jump conditions across the interface has been looked into previously (Ishii, 1975). The non-linearity of the equations and movement of the boundary between two phases pose a serious challenge in getting accurate numerical solutions. Earlier models were mostly empirical in nature (Toomey and Johnstone, 1952). The first seminal work on the reduction of empiricism and bringing flow dynamics as governing equations was done by (Anderson and Jackson, 1967b). They treated the fluid and particle phases as interpenetrating media and essentially introduced separate fluid and particle phase momentum equations. In their work, the local point variables like particle velocity, fluid pressure, fluid velocity etc. were replaced by local mean variables by averaging the point variables over regions having many particles.

With the advancement in computational capabilities, the field of computational fluid dynamics (CFD) has been emerging as an important tool for modeling complicated

multiphase flows. Sophisticated numerical tools have been developed to tackle the complexities involved in gas-solid flows. Two such methods are Two Fluid Model (TFM) and Discrete Element Modeling (DEM), respectively. In TFM, the various different phases are considered to be interpenetrating continua and are solved in an Eulerian-eulerian framework. In this method, a continuum is assumed for a collection of particles. Each of the phases has its own continuity, momentum and energy equations. Closure schemes are applied to make the set of equations complete. The interphase interaction is accounted for through source terms in the momentum and energy equations of each individual phase. In DEM, the particles are treated in a Lagrangian framework, whereas the fluid field is Eulerian. Motion of individual particles is tracked using Newton's laws, thus taking into account of all the collision forces with other particles and walls. The fluid-particle interaction is taken into account through drag forces.

The two approaches have been investigated by (Gera et al., 1998). In their work, they have used DEM and TFM to investigate the hydrodynamics of large particle fluidized bed, comparing bubble rise velocity, voidage variations, averaged particle and fluid velocities. Hybrid DEM-TFM method has been used to predict pressure drop, bed expansion and other dynamical characteristics of a fluidized bed by (Sun et al., 2007). Even stochastic methods like Direct Simulation Monte Carlo (DSMC) methods have been used to model particle collisions by (Shuyan et al., 2005) in order to investigate cluster formation in circulating fluidized beds.

Several researchers have used both TFM (Chapman and Cowling, 1970; Chiesa et al., 2005; Enwald and Almstedt, 1999; Gidaspow, 1994; Gidaspow et al., 2004; Kuipers et al., 1993; Patil et al., 2005a; Patil et al., 2005b) and DEM (Hoomans et al., 1996; Kafui et al., 2002; Kawaguchi et al., 2002; Kawaguchi et al., 1998; Peng et al., 2010; Tsuji et al., 1999; Tsuji et al., 1993; Zhou et al., 2010) to investigate the dynamics of fluidized beds. Comprehensive review on both the methods has been documented by (Deen et al., 2007; Hoef van der et al., 2008; Zhu et al., 2008). Discrete Element Modeling has been used for the present work in order to investigate a more fundamental particle scale dynamical behavior of fluidized beds.

Motivation

There has been extensive past and on-going research on various aspects of fluidized bed dynamics. Both experimental and computational efforts have been made in the literature to investigate important properties of fluidized systems like pressure distribution in the bed, void fraction profiles, particle velocity profiles etc. These results lay the foundation for better design of large scale fluidized bed systems used in a wide variety of industries.

Jetting fluidized beds are widely used in industries for their superior mixing performance. In that view, a thorough investigation of jetting beds is necessary to understand the important parameters that affect bed operation. One of the focuses of the present work is on the computational modeling of multiple jet interactions inside fluidized bed systems. The results serve as validations for in-house experimental investigation of multiple jets. The computational analysis also looks into important parameters of the bed which are difficult for the experiments to measure like granular temperature, which is a measure of particle fluctuations inside the bed. Knowledge of mixing characteristics in these jetting fluidized bed systems is essential for design purposes. The computations have been used to investigate various different paths of particle mixing. A different approach of particle mixing analysis has been investigated inside a flat bottomed spouted bed, wherein use of convective and diffusive characteristics inside the bed have been used to identify different mixing regimes.

DEM-CFD framework has been used since 1990's for capturing the complicated fluid-particle interactions inside a fluidized bed. Conventional DEM-CFD framework suffers from particle field instability issues with finer grid sizes. To avoid this, a single coarse grid is generally adopted, which enables a smooth particle field across fluid cells. This on the other hand is detrimental for fluid field resolution and prevents simulating intricate geometries as well as high speed fluid-particle flows requiring finer fluid cells. Apart from investigating jetting fluidized bed characteristics, the present work also focuses on the development of a novel two-grid formulation having separate particle field and fluid field grids which is capable of simulating cases not possible with conventional DEM-CFD framework.

Contributions of this Work

The main scientific and engineering contribution of this work is the development of a general framework to simulate complicated fluid-particle interactions inside fluidized beds systems as well as other granular flows. Development and implementation of a novel two-grid formulation to simulate fluid-particulate systems adds to the novelty of the work. With this new framework in place, it would be possible to simulate cases previously not possible with conventional DEM-CFD framework. To the best of our knowledge, this is the first time a two-grid technique has been adopted in simulating fluidized bed systems. The computational results have been validated with in-house experiments and the results show reasonable match with experiments in terms of void fraction profiles, particle velocity profiles, pressure drop inside the bed and particle flux. Finally, an effort has been made to capture the complicated transient heat transfer characteristics inside a jetting fluidized bed. Conjugate heat transfer analysis has been used along with the use of obstacle boundary conditions to investigate transient wall heat flux. This basic simulation forms the basis for further detailed heat transfer investigations.

The following journal articles and conference papers are an integral part of this dissertation:

- A Novel Two Grid Formulation for Fluid-Particle Systems using the Discrete Element Method, S. Deb, D. Tafti, Powder Technology, Volume 246, 2013, Page 601-616.
- Efficient parallel CFD-DEM simulations using OpenMP, Amit Amritkar, Surya Deb, Danesh Tafti, Journal of Computational Physics, Volume 256, 1 January 2014, Pages 501-519.
- Investigation of flat bottomed spouted bed with multiple jets using DEM-CFD framework"**,** S. Deb, D. Tafti, Powder Technology, **under review**
- Discrete Element Modeling and Validation of Fluidized Bed with Multiple Jets, Surya Deb, Danesh Tafti, **To be submitted**.
- Discrete element modeling of fluidized beds with multiple jets, S. Deb, D. Tafti, ASME 2012 Fluids Engineering Division Summer Meeting, July 2012, Puerto Rico**.**

- Particle Scale Heat Transfer Analysis in Rotary Kiln, A. Amritkar, D. Tafti, S. Deb , ASME Summer Heat Transfer Conference, July 2012, Puerto Rico.

Organization of Dissertation

The rest of the dissertation is organized as follows. The second chapter introduces the DEM-CFD formulation and validation with established experiments in literature. The investigation of flat bottomed spouted bed with DEM-CFD framework is discussed in Chapter 3. Chapter 4 presents the computational results and validations with in-house experiments performed on multiple jet fluidized bed setup. Chapter 5 presents the novel two-grid formulation along with validation results with experiments. This is followed by Chapter 6, which discusses the basic framework of conjugate transient heat transfer analysis performed inside a jetting fluidized bed with a single central jet. Finally, conclusions and future scope of this work are presented in Chapter 7.

Chapter 2 DEM Formulation and Validation

Discrete Element Modeling (DEM) coupled with our in-house code GenIDLEST (Generalized Incompressible Direct and Large Eddy Simulation of Turbulence) has been used to numerically model the solid-fluid interactions in the jetting fluidized bed. Originally (Cundall and Strack, 1979) developed the discrete element methodology for granular flows and (Tsuji et al., 1993) used it for the first time to simulate a 2D fluidized bed with a single jet. The volume averaged Navier-Stokes equations derived by (Anderson and Jackson, 1967a) are used for solving the fluid flow. DEM offers two different approaches for resolving the particle-particle collisions. They are the hard sphere and soft sphere approaches, respectively. In our analysis, the soft sphere approach is considered as it allows for multiple particle interaction which is more likely in a dense fluidized bed unlike the hard sphere technique which can only account for binary collisions.

Particle Governing Equations

The motion of each particle is tracked based on Newton's Law of motion as follows:

$$m_p \frac{d\vec{v}_p}{dt} = (\rho_p - \rho_g) V_p \vec{g} + \vec{F}_{p,Drag} + \vec{F}_{p,Collision} \tag{2.1}$$

$$I_p \frac{d\vec{\omega}_p}{dt} = \vec{T}_{p,Collision} \tag{2.2}$$

where $m_p, \vec{v}_p, V_p, \vec{F}_{p,Collision}$ are the particle mass, particle velocity, particle volume, and collision forces, respectively. $I_p, \vec{\omega}_p, \vec{T}_{p,Collision}$ represent particle moment of inertia, particle angular velocity, and total torque acting on the particle, respectively. Integrating Eq. (2.1) in time advances the linear position of the particle whereas integrating Eq. (2.2) updates the angular motion of the particle at each time step.

Particle-particle collision formulation

The soft sphere model handles particle-particle collisions as finite particle overlaps. Using the overlap, the inter-particle forces are calculated based on Hooke's Law (Tsuji et al., 1993), where a particular pair in collision is modeled as a normal and

tangential linear spring and dashpot arrangement. The deflection of the particles during a collision is governed by the spring, whereas the inelasticity of collisions is taken care by the dashpot through energy dissipation. An additional sliding element is placed in series with the spring mass damper in the tangential direction. The slider allows the particles to slide against each other as well, limiting the maximum magnitude of the tangential force. Spring constants and damping coefficients in the normal and tangential directions are used to calculate the normal and tangential forces, respectively due to the particle overlaps. Figure 2.1 shows the entire mechanism.

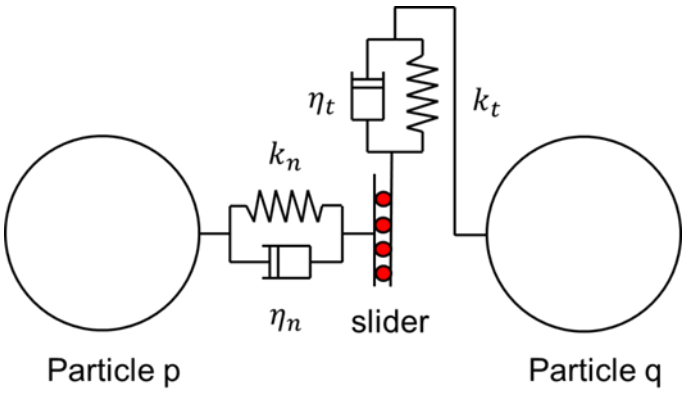

Figure 2.1: Diagram showing the mechanism of DEM during particle collisions

The following equations are used for the inter particle collisions. The equations deal with the motion of particle p when it collides with particle q.

$$\vec{f}_{n,pq} = -k_n \vec{\delta}_{n,pq} - \eta_n \vec{v}_{n,pq} \tag{2.3}$$

$$\vec{f}_{t,pq} = -k_t \vec{\delta}_{t,pq} - \eta_t \vec{v}_{t,pq} \tag{2.4}$$

where $\vec{f}_{n,pq}, \vec{f}_{t,pq}, k_n, k_t$ are the normal force, tangential force, normal spring constant and tangential spring constant, respectively. $\vec{\delta}_{n,pq}, \vec{\delta}_{t,pq}, \eta_n, \eta_t$ are the normal particle overlap, tangential particle overlap, normal coefficient of viscous dissipation and tangential coefficient of viscous dissipation, respectively. $\vec{v}_{n,pq}, \vec{v}_{t,pq}$ are the normal and tangential relative velocities of the particle, respectively. The relative velocities of particle in the normal and tangential directions are given as follows:

$$\vec{v}_{n,pq} = (\vec{v}_{pq} . \vec{n}_{pq}) \vec{n}_{pq} \tag{2.5}$$

$$\vec{v}_{t,pq} = \vec{v}_{pq} - \vec{v}_{n,pq} + r_p(\vec{\omega}_p + \vec{\omega}_q) \times \vec{n}_{pq} \tag{2.6}$$

where $\vec{v}_{pq}$ is the relative velocity between particles p and q. r_p is the particle radius and $\vec{n}_{pq}$ represents the normal unit vector pointing from the center of particle p to the center of particle q as shown below.

$$\vec{n}_{pq} = \frac{\vec{x}_p - \vec{x}_q}{|\vec{x}_p - \vec{x}_q|} \tag{2.7}$$

where $\vec{x}_p, \vec{x}_q$ represent the position of particle p and q, respectively in physical space. The tangential force is restricted by the frictional slider given by Coulomb's Law of friction as follows:

$$|\vec{f}_{t,pq}| \leq \mu |\vec{f}_{n,pq}| \tag{2.8}$$

where μ represents particle-particle coefficient of friction.

Finally, the net force and torque acting on the particle p due to all its neighbors is calculated, respectively as follows:

$$\vec{F}_{p,Collision} = \sum_q (\vec{f}_{n,pq} + \vec{f}_{t,pq}) \tag{2.9}$$

$$\vec{T}_{p,Collision} = \sum_q (r_p \vec{n}_{pq} \times \vec{f}_{t,pq}) \tag{2.10}$$

The same methodology has been used to account for particles colliding with walls. The wall is considered as a particle with an infinite diameter and its momentum is not affected during a collision. Since all the walls are stationary in the simulation, they maintain their zero velocity state throughout.

Particle-fluid drag formulation

The interstitial fluid velocity (fluid cell velocity for single grid) is used for calculating the drag forces on the particles. Ergun(Ergun, 1952) and Wen & Yu(Wen and Yu, 1966) drag correlations have been used in our analysis.

$$\beta_{ergun} = 150\frac{(1-\varepsilon)^2}{\varepsilon d_p^2} + 1.75(1-\varepsilon)\frac{\rho_g}{d_p}|\vec{u} - \vec{v}_p| \; if(\varepsilon < 0.80) \tag{2.11}$$

$$\beta_{wen} = \frac{3}{4} C_D \frac{\varepsilon(1-\varepsilon)}{d_p} \rho_g |\vec{u} - \vec{v}_p| \varepsilon^{-2.65} if(\varepsilon \geq 0.80) \tag{2.12}$$

To remove the discontinuity in the drag formulation at ε=0.8, a smoothing function has been used as follows (Huilin et al., 2003):

$$sm\_fac = (\arctan(150 \times 1.75(\varepsilon - 0.80))) / \pi + 0.50 \tag{2.13}$$

$$\beta = (1 - sm\_fac) \times \beta_{ergun} + sm\_fac \times \beta_{wen} \tag{2.14}$$

where $\beta, d_p, \vec{u}, \vec{v}_p$ represents interphase momentum exchange coefficient, particle diameter, interstitial fluid velocity in a fluid cell, and particle velocity, respectively. ρ_g, C_D stand for fluid density and coefficient of drag, respectively.

The coefficient of drag is calculated as follows:

$$C_D = \frac{24}{\mathrm{Re}_p}(1.0 + 0.15\mathrm{Re}_p^{0.687}), \mathrm{Re}_p \leq 1000 \tag{2.15}$$

$$C_D = 0.44, \mathrm{Re}_p > 1000 \tag{2.16}$$

where Re_p is the particle Reynold's number given by:

$$\mathrm{Re}_p = \frac{\varepsilon d_p |\vec{u} - \vec{v}_p| \rho_g}{\mu_g} \tag{2.17}$$

where μ_g denotes the fluid viscosity.

Once the interphase momentum exchange coefficient is obtained, the drag on a particle is calculated as shown below:

$$\vec{F}_{p,Drag} = \frac{V_p \beta}{(1-\varepsilon)}(\vec{u} - \vec{v}_p) \tag{2.18}$$

Fluid Governing Equations

The fluid field is coupled to the particles and the Navier-Stokes continuity and momentum equations as derived by (Anderson and Jackson, 1967a) are given by

$$\frac{\partial(\varepsilon\rho_g)}{\partial t} + \nabla.(\varepsilon\rho_g\vec{u}) = 0 \tag{2.19}$$

$$\frac{\partial(\varepsilon\rho_g\vec{u})}{\partial t}+\nabla.(\varepsilon\rho_g\vec{u}\vec{u})=-\nabla p-\nabla.(\varepsilon\bar{\tau}_g)+\frac{\vec{f}_{Drag}}{V_{fg}}+\rho_g\vec{g} \tag{2.20}$$

$$\vec{f}_{Drag}=-(\sum_N \vec{F}_{p,Drag}) \tag{2.21}$$

where $p,\bar{\tau}_g,\vec{g},V_{fg}$ represents pressure, the viscous stress tensor, acceleration due to gravity and volume of a fluid cell, respectively. $\vec{f}_{Drag}$ and N represent the drag acting on a fluid cell and number of particles present inside a fluid cell, respectively. The fluid equations are based on Model B (Gidaspow, 1994). Unlike Model A, in Model B, the pressure drop inside a fluid cell is considered only due to the fluid and not the particulate phase. This causes the pressure force acting on the particles in Model B to take the form of buoyant force. The above equations are solved in a generalized co-ordinate framework on a non-staggered grid using a finite-volume based fractional step method (Tafti, 2001). The inclusion of the unsteady term in Eq. (2.19) in the pressure equation formulation results in numerical instabilities and hence the term is neglected. The implications of this exclusion are tested in two validation cases with experiments and with simulations using our in-house code GenIDLEST (Tafti, 2001). Figure 2.2 shows the CFD-DEM coupling algorithm used.

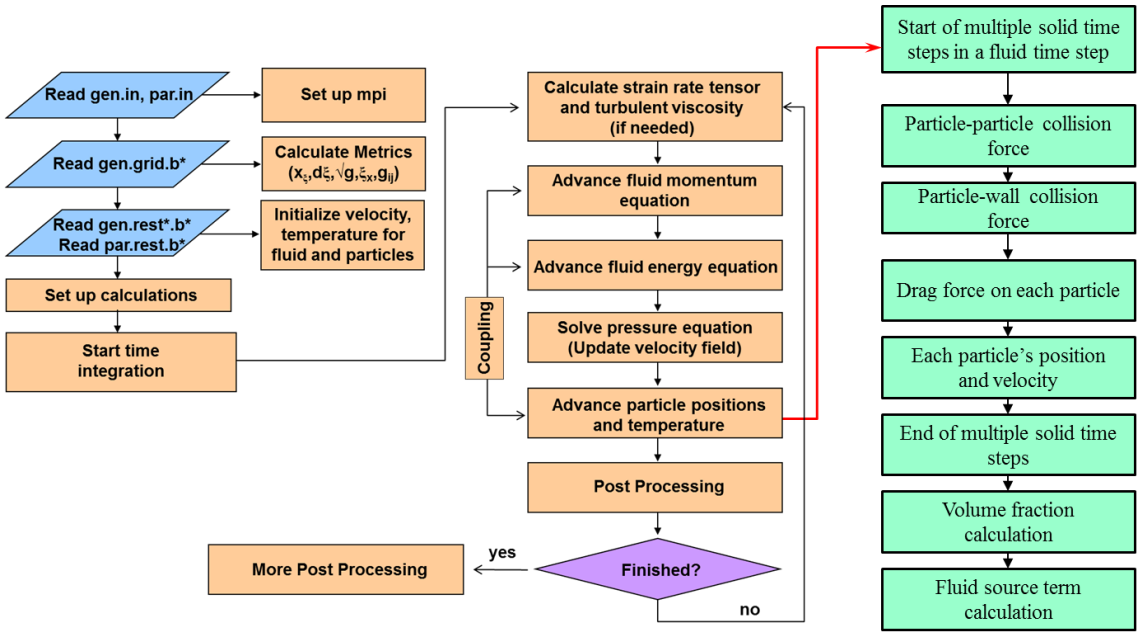

Figure 2.2: Flowchart showing CFD-DEM coupling used in GenIDLEST

Basic tests have been performed to check the correctness of DEM implementation in our in-house code GenIDLEST. Followed by this, is the section showing validation of DEM with established experimental results.

DEM Implementation Tests (Without Fluid)

The code is first tested for basic energy conservation of a single particle falling vertically under gravity from a certain height with coefficient of restitution for wall collision (e) set to 1. No other dissipative forces or horizontal forces act on the particle. Under these conditions, the particle should continue to bounce back to the same height after each collision with wall and continue to do that indefinitely. Figure 2.3 shows a particle of diameter 1.2 mm falling from a height of 10 mm and coefficient of restitution of 1.

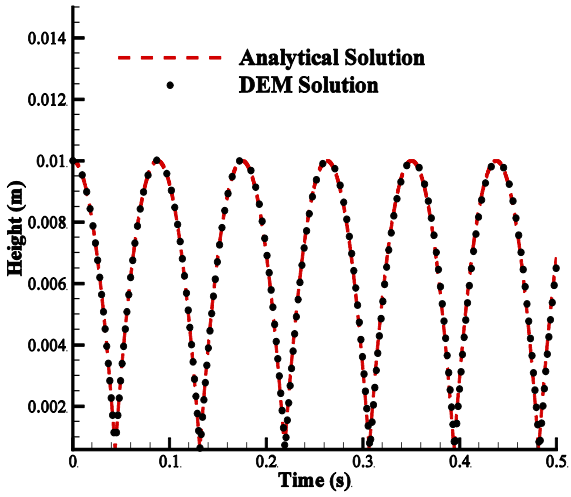

Figure 2.3: Comparison of particle-wall collision model with analytical solution for e = 1

DEM solution falls very close to the analytical solution, showing that the energy for the particle is being conserved for this basic test case. Next the same particle released from 10 mm height with a coefficient of restitution of 0.9. The maximum height of rebound of the particle will keep on decreasing with time. Figure 2.4 shows that DEM is able to capture the rebound heights, which compare well to the analytical solution. These formed the tests for correct implementation of DEM for the wall collision model.

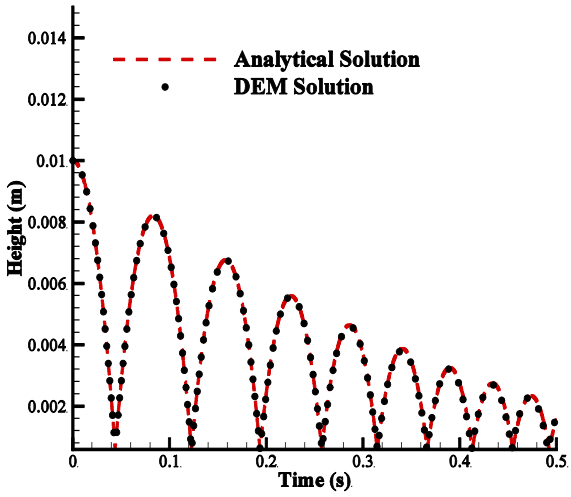

Figure 2.4: Comparison of particle-wall collision model with analytical solution for e = 0.9

Next the code is tested for a 2 particles system with the particles colliding head on along the x-axis without gravity. No rotation is considered in this case and no other dissipative forces act on the 2-particle system. The coefficient of restitution for wall collision (e) is again set to 1 to have perfectly elastic collisions without any energy loss. Under these conditions, the total system energy should be conserved. Figure 2.5 shows that the total system energy is conserved with conversion of kinetic energy of the particles into potential energy of the spring during collision and vice versa upon losing contact.

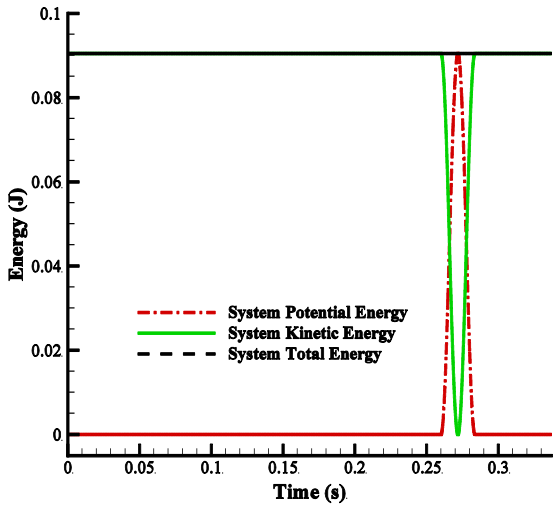

Figure 2.5: Energy variation during collision of 2 particles using DEM

In Figure 2.5, a single instance of the collision is depicted. This formed the test for correct implementation of DEM for particle-particle collision model being used in the code.

The time period of the collision can be found out theoretically based on the natural frequency of the spring used in collision modeling. The time step of DEM calculations is governed by this time period of particle-particle collision. In order to properly resolve the collisions, the simulation time scale must be at least $1/10^{th}$ of the collision time scale.

Single Grid Validation

Validations for the CFD-DEM solver have been carried out for two different fluidized bed cases. The code has been validated firstly with a uniformly fluidized bed (Muller et al., 2009) having a porous distributor plate. The dimensions of the fluidized bed in the experiment are 44 mm×10 mm×1500 mm (width, depth/transverse thickness, height). The height of the bed in our simulation was reduced to 160 mm in order to reduce the computational time involved. The experimental technique used to measure void fractions was Magnetic Resonance (MR). Superficial gas velocities of 0.6 m/s and 0.9 m/s were used to investigate the bed behavior. Poppy seeds were used as particles in the experiment. Details of the particle properties and modeling parameters are summarized in Table 2.1. The initial static height of the bed was 30 mm with 9240 particles.

Table 2.1: Simulation parameters and particle properties for (Muller et al., 2009)

Simulation parameters	Values
Bed	
Width (m)	0.044
Transverse Thickness (m)	0.010
Height (m)	0.160
Particles	
Material	Poppy seeds
Number	9240
Diameter (mm)	1.2
Density (kg/m^3)	1000
Coefficient of normal restitution	0.98
Minimum fluidization velocity (m/s)	0.30

Coefficient of friction	0.1
Spring stiffness coefficient (N/m)	800
Fluid Properties	
Material	Air
Density (kg/m^3)	1.205
Viscosity (kg/m-s)	1.8×10^{-5}
Grid Details	
Cells along width (along x)	12
Cells along height (along y)	32
Cells along depth (along z)	2

(Muller et al., 2009) also performed numerical simulations to validate their DEM code. They used 2D calculations for the fluid field because of the transverse thickness being 10 mm. In their simulations, the walls at z = 0 and z = 10 mm were set as full slip condition for the fluid phase, essentially not considering the fluid momentum equation along z direction. In our analysis, for the purpose of validating GenIDLEST, full 3D simulations have been performed for both the fluid field and DEM. The walls along the x and z axes have been set to no slip condition and the momentum equation along z direction has been taken into account in order to have a more realistic modeling of the experiments. Both the experiments and the simulations were time averaged for 23 seconds. (Muller et al., 2009) performed sensitivity analysis on the fluidized bed system by varying different parameters which influence the simulations. The base cases have been selected for the validation of our CFD-DEM code. Figure 2.6 shows the voidage profiles for the case with 0.6 m/s ($U/U_{mf} = 2$) at two different heights of 16.4 mm and 31.2 mm from the distributor plate, respectively.

Figure 2.6 shows close comparison of the voidage profile obtained from our simulation with experiments done by (Muller et al., 2009). At a height of 16.4 mm, the profile obtained from our simulation compares better to the experiment than the predicted voidage profile obtained by (Muller et al., 2009).

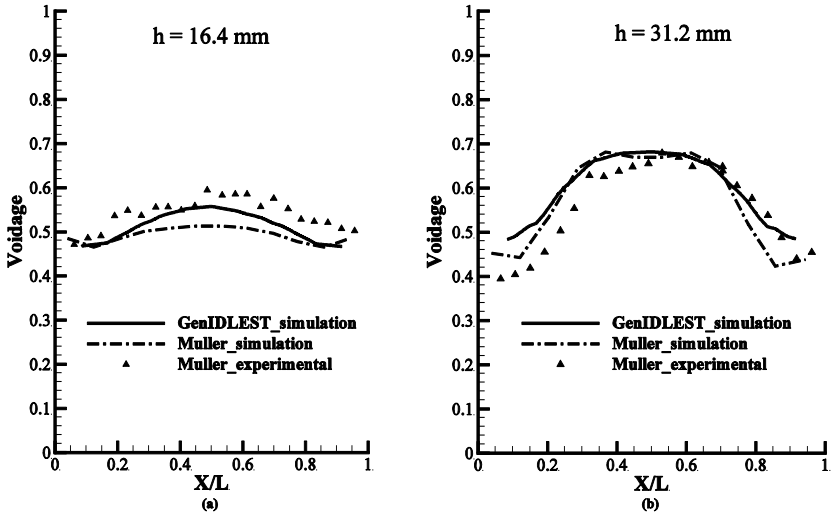

Figure 2.6: Voidage profiles at superficial velocity of 0.6 m/s (U/Umf = 2). (a) At a height of 16.4 mm from distributor plate, (b) At a height of 31.2 mm from the distributor plate

At a height of 31.2 mm, both the DEM simulations performed by us and (Muller et al., 2009) show some discrepancy with the experiments near the walls. DEM over predicts the void fraction values closer to the walls. A definite cause of this over prediction is difficult to provide but a possible reason might be that DEM over predicts bubble size near the walls giving rise to lower number of particles close to the walls. This in turn results in higher voidage values in close proximity to the walls. But overall GenIDLEST predicts the voidage profiles very well at the bed center. Figure 2.7 shows the voidage profiles for the case with 0.9 m/s ($U/U_{mf} = 3$) at two different heights of 16.4 mm and 31.2 mm from the distributor plate, respectively.

For the higher superficial velocity of 0.9 m/s, good predictions of the voidage values are obtained. In Figure 2.7(a), our simulations compare very well with the experimental values both near the center of the bed as well as near the walls. Figure 2.7(b) also shows that the voidage profiles predicted at $h = 31.2mm$ fall very close to the experimental results. The over prediction of voidage near the walls is much lower in our analysis as compared to that by (Muller et al., 2009). The reason behind this might be the full 3D simulation performed in our simulations.

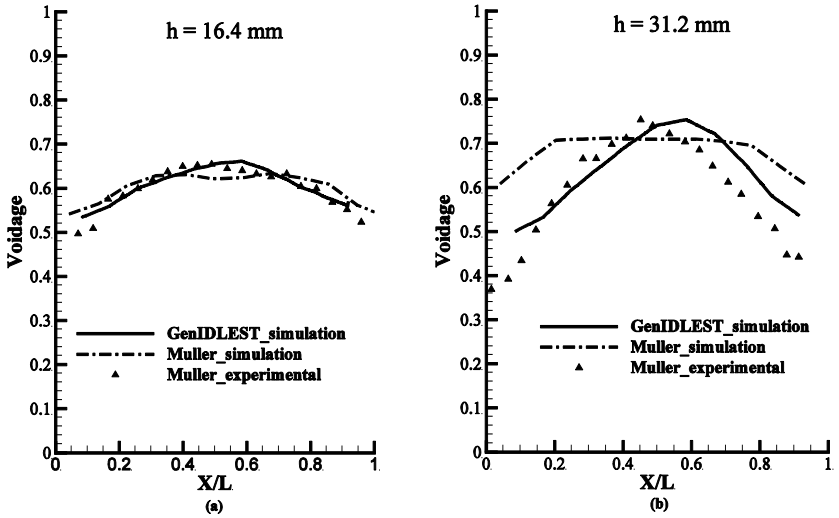

Figure 2.7: Voidage profiles at superficial velocity of 0.9 m/s (U/Umf = 3). (a) At a height of 16.4 mm from distributor plate, (b) At a height of 31.2 mm from the distributor plate

The lack of friction on the walls along the z-direction for the particles and for the fluid in the simulations of (Muller et al., 2009) could have resulted in the particles moving higher up the bed. This result in the voidage profiles at higher heights flatter compared to our simulations. Figure 2.8 shows the time averaged solid fraction and velocity contour for U = 0.6 m/s. The vectors represent fluid velocities and the legend shows the magnitude.

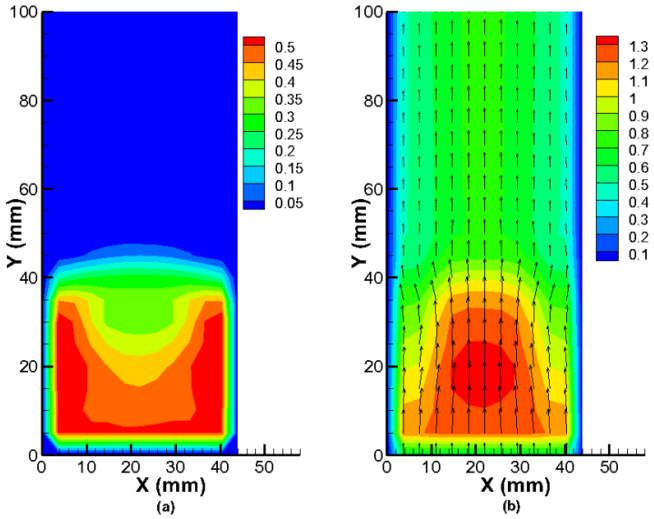

Figure 2.8: Contour plots of central plane along z direction for U = 0.6 m/s. (a) Solid Fraction, (b) Fluid Velocity in m/s

It can be seen from Figure 2.8(b), that the velocity in the center of the bed is higher as expected. The fluid takes the path of least resistance through the bubbles at the center of the bed. Figure 2.9(a) and (b) show the pressure distribution across the height of the bed for the 0.6 m/s and 0.9 m/s cases, respectively.

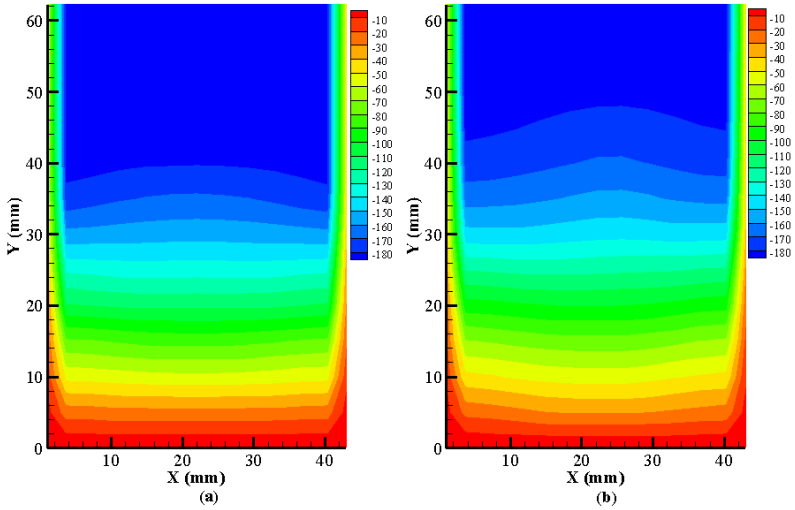

Figure 2.9: Pressure contours at superficial velocities of (a) 0.6 m/s (U/U_{mf} = 2), (b) 0.9 m/s (U/U_{mf} = 3)

The difference between the pressures near the freeboard and the distributor plate should be close to the weight of the particles present inside the bed. The weight of the particles used in the simulations is 0.0820 N. The pressure difference across the bed is about 184.22 N/m^2, which is equivalent to 0.0811 N of force across the cross-section of the fluidized bed setup. The pressure in the contours is displayed in terms of the pressure drop over the atmospheric operating pressure in Pascals.

Next the single grid CFD-DEM code has been tested with a fluidized bed having a single jet (Tsuji et al., 1993). Details of particle properties and simulation parameters are given in Table 2.2.

Table 2.2: Simulation parameters and particle properties for single jet validation

Simulation parameters	Values
Bed	
Width (m)	0.15
Transverse Thickness (m)	0.004
Height (m)	1

Particles	
Material	Aluminum
Number	2400
Diameter (mm)	4.0
Density (kg/m^3)	2700
Coefficient of normal restitution	0.90
Minimum fluidization velocity (m/s)	1.77
Coefficient of friction	0.30
Spring stiffness coefficient (N/m)	800
Fluid Properties	
Material	Air
Density (kg/m^3)	1.205
Viscosity (kg/m-s)	1.8×10^{-5}
Grid Details	
Cells along width (along x)	15
Cells along height (along y)	50
Cells along depth (along z)	1 (2D Simulation)

The initial static height of the fluidized bed is 220 mm. The transverse thickness of the bed was 22 mm in the actual experiments performed by (Tsuji et al., 1993). In order to reduce the number of particles and thus computational time, the transverse thickness in our analysis has been kept as 4 mm which is the particle diameter used. CFD-DEM was first developed by (Tsuji et al., 1993) and so their 2D simulation on this set up forms the first seminal work with DEM.

In the 2D simulations of (Muller et al., 2009), the fluid has been considered as inviscid and the superficial gas velocity ranged from 2.0 to 2.6 m/s. In order to validate results with GenIDLEST, a single case with superficial velocity of 2.6 m/s has been chosen. This leads to a jet velocity of 39 m/s with 10 mm as the jet width. Figure 2.10 shows the instantaneous snapshots of particles during the transient period within the first 1 second. It shows an initial bed expansion and bubble formation due to the injection of the jet. Subsequently, the bubble erupts and another one starts forming at the distributor plate. This bubble grows in size as it expands while moving up the bed near the freeboard. The subsequent formation and eruption of bubbles give rise to pressure fluctuations.

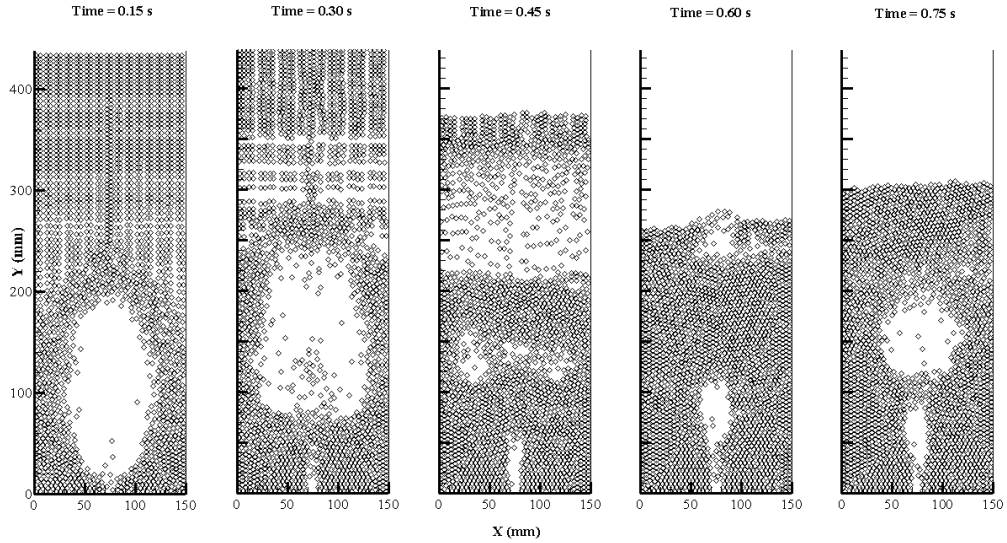

Figure 2.10: Instantaneous snapshots of particles in transient stage of bed operation

The pressure fluctuates with time and the fluctuations were measured in the experiments at a distance of 200 mm downstream from the distributor plate. In our analysis, fluctuations were measured using a probe at the center of the bed at a distance 200 mm from the distributor plate. The values of pressure variations have been compared as shown in Figure 2.11. The general trend of the fluctuations predicted in our simulation lies close to the experimental results. The amplitudes of pressure variation compare well with the experiment. The DEM pressure fluctuation amplitudes of (Tsuji et al., 1993) show some discrepancy with their experimental results. A proper reasoning for this has not been provided by (Tsuji et al., 1993).

This concludes the validation of the CFD-DEM methodology for a single grid framework. Good agreement with experimental values show that neglecting the transient term from Eq. (2.19) has no significant effect on the time averaged as well as instantaneous results. In later investigations, not included in this dissertation, inclusion of the unsteady term in Eq. (2.19) did not show any definite differences in void fraction and solid velocity distributions.

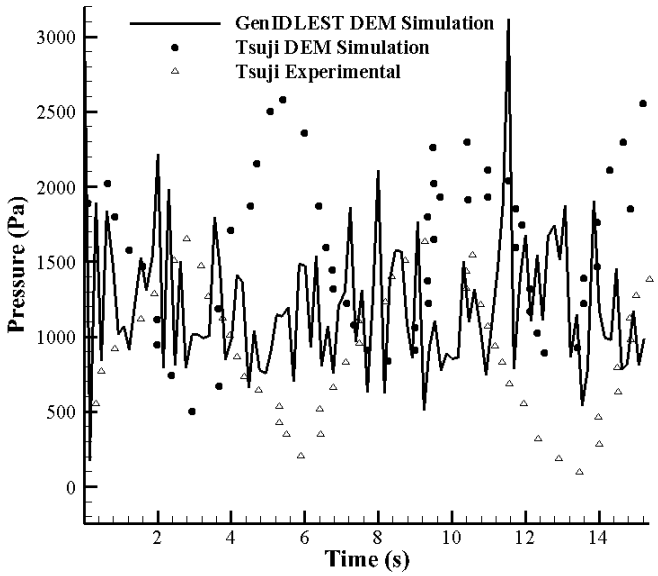

Figure 2.11: Pressure fluctuation profile

Chapter 3 Investigation of flat bottomed spouted bed with multiple jets using DEM-CFD framework

Introduction

The operation of spouted beds involves injection of narrow jets through a single or multiple slots/nozzles. Unlike conventional fluidized beds, where a porous distributor plate is used, the flow pattern of particles is more regular and orderly in spouted beds, giving rise to two distinct regions: a narrow and dilute phase known as "spout" containing upward flowing gas-particle mixture and a denser region surrounding the "spout" incorporating downward flowing particles. This unique flow pattern aids in achieving a better circulation and mixing for particles of different sizes. Wide spread applications of spouted beds exist in industries, ranging from drying of granular materials, coating, granulation of fertilizers, combustion and gasification (Epstein and Grace, 1997; Konduri et al., 1999; Mathur and Epstein, 1974). A good knowledge of gas and particle dynamics is essential for evaluating the important characteristics of a spouted bed like particle circulation rates and spout shapes. Getting detailed information about the entire space of the bed is difficult with experiments, which generally requires invasive procedures that can alter the flow and particle dynamics in the bed. A full scale numerical simulation is often desired to understand the complicated gas-particle dynamics inside a spouted bed.

With recent developments in computational facilities, high fidelity numerical simulations on granular flows could be performed to investigate particle-particle and particle-fluid interactions. Discrete Element Modeling (DEM) and Two-Fluid-Model (TFM) are the two most widely used numerical methodologies for modeling granular flows like fluidized beds and spouted beds. The two methods follow fundamentally different approaches. TFM considers the gas and solid to be two distinct interpenetrating media and solves for their interaction in an Eulerian-Eulerian approach. On the other hand, DEM is an Eulerian-Lagrangian approach where the fluid flow is solved in an Eulerian framework while tracking each individual particle in a Lagrangian fashion. A much higher resolution is provided by DEM compared to TFM as it resolves the

complete dynamics of each particle in the flow. TFM requires additional closure equations to account for the continuum description of particles. DEM does not require any closure laws due to its discrete treatment of individual particles. DEM was first developed by (Cundall and Strack, 1979) and later adopted for simulation of fluidized beds and coupled with CFD by (Tsuji et al., 1993). Since then, DEM has been used in investigating a wide variety of applications including surface diffusion problems (Kuwagi et al., 2000; Limtrakul et al., 2004), modeling behavior of cohesive particles (Iwadate and Horio, 1998; Mikami et al., 1998), segregation of binary particle mixtures (Feng et al., 2004; Feng and Yu, 2010), capturing bubble dynamics (Kobayashi et al., 2000; Pain et al., 2002; Rong et al., 1999) and so on. A comprehensive review focusing on the research work done using DEM has been given by (Deen et al., 2007; Zhou et al., 2010; Zhu et al., 2008).

Considerable efforts have been done in modeling the dynamics of spouted beds using DEM. DEM-CFD approach was first used by (Kawaguchi et al., 2000) to simulate a quasi-three dimensional spouted bed, and obtained typical flow patterns like stable spout, fountain and annulus. A flat bottomed spouted bed has been modeled in a 3D DEM framework by (Takeuchi et al., 2004). They reported self-similarity of the radial distribution of axial particle velocities and studied the effects of a vortex ring fixed at the bottom of the vessel on gas flow patterns. Two dimensional simulations of spouted beds have been tried by (Link et al., 2004; Swasdisevi et al., 2004). A low Reynolds number $k-\varepsilon$ turbulence model was used by (Zhao et al., 2008) to simulate a 2D spouted bed with draft tubes. (Limtrakul et al., 2004) modeled mass transfer in gas-solid catalytic spouted bed reactor for ozone decomposition and obtained results comparable with experiments. Recent simulations have been performed by (van Buijtenen et al., 2012; van Buijtenen et al., 2011), in which a combined experimental and computational approach using DEM has been adopted to study the effect of multiple spouts in a pseudo-2D multiple spout fluidized bed. The aim of this present work is to provide an understanding of multiple jet interactions inside a pseudo-2D rectangular spouted bed with a flat bottom. Two fluidization velocities are considered with one, two and three jet configurations. Solids velocity, granular temperature, and mixing characteristics of the bed are investigated.

This chapter is structured as follows. The following section describes the computational details followed by a section on results and discussions. The next section evaluates different measures of mixing in the bed followed by summary and conclusions.

Computational Details

The bed geometry with dimensions of $56.4mm \times 280mm \times 4.95mm$ in the x, y and z directions, respectively are shown in Figure 3.1.

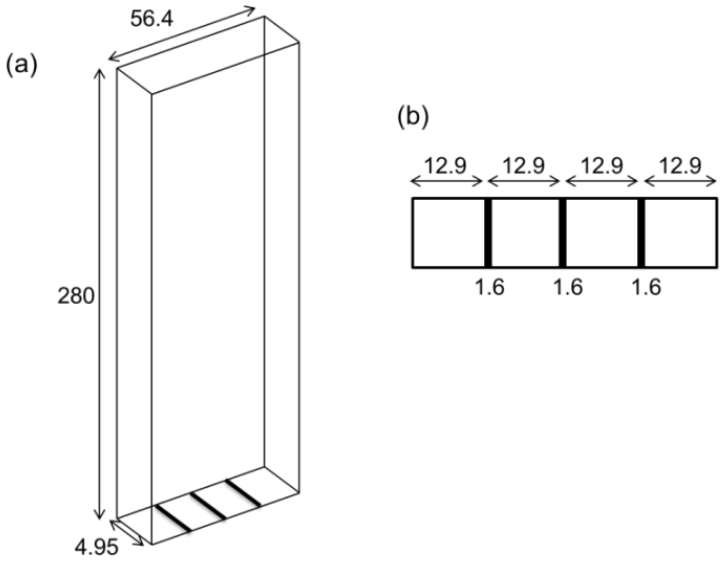

Figure 3.1: (a) Dimensions of the jetting fluidized bed (in mm), (b) Slit distribution on distributor plate

The jets (slits) are two dimensional with a width of 1.6 mm and a depth of 4.95 mm, thus extending through the entire depth of the bed. Single, double and triple jet configurations can be achieved using this setup depending on the number of jets activated.

Details of jets

The slits are placed at a distance of 12.9 mm from each other and the side walls in both the experiments and simulations. Two different superficial velocities of 1.6 and 3 times the minimum fluidization velocity have been used, respectively, for comparison with experiments. The minimum fluidization velocity is given as follows

$$U_{mf} = \frac{(\rho_p - \rho_g) g d_p^2}{150 \mu_g} \frac{\varepsilon^3}{1-\varepsilon} \tag{3.1}$$

The different cases that have been run and compared to the experiments are shown in Table 3.1.

Table 3.1: Details of Simulated Cases

Particle Diameter (μm)	No. of Jets	Superficial Velocity (m/s)	Jet Velocity (m/s)
550	1	0.388 (1.60 U_{mf})	13.58
550	1	0.725 (3.01 U_{mf})	25.38
550	2	0.725 (3.01 U_{mf})	12.69
550	3	0.725 (3.01 U_{mf})	8.46

Grid details

The dimensions of the fluid cells along the length, height and depth (x, y and z) of the bed, respectively are 1.61 mm, 1.75 mm and 1.65 mm. This corresponds to $35 \times 160 \times 3$ number of fluid cells in the entire domain of the bed. Each fluid cell almost resembles a cube with the dimension in each direction close to 3 times the particle diameter for 550 μm particles. This has been done in accordance with the numerical experiments performed by (Muller et al., 2009). According to their study, the dimensions of a fluid grid in DEM-CFD framework should be at least 3-4 times the particle diameter in order to have a smooth temporal and spatial variation of the particulate field.

Boundary conditions

The condition on all the walls for the fluid phase has been set to no slip. The jet velocity given in Table 3.1 has been imposed as an inlet boundary condition. The top outlet has been provided with a mass conserving uniform velocity profile.

Particle properties

Glass particles of diameter 550 μm have been used, respectively, in the simulations and the experiments. The density of the particles is 2500 kg/m^3. The particles fall in Geldart group B category. The number of particles for the 550 μm diameter is

about 100,000. The initial bed height for all the cases is close to 60 mm in both the experiments and the simulations. The important particle properties are listed in Table 3.2.

Table 3.2: Particle properties used in DEM

Diameter (μm)	Density (kg/m^3)	U_{mf} (m/s)	Number of particles
550	2500	0.24	100,000

DEM parameters for collision modeling

Modeling of inter-particle collisions require coefficient of restitution of particles, the spring constants in the normal and tangential directions and the coefficient of friction between the particles as input parameters. In our analysis, both the normal and the tangential spring constants are considered to be the same standard values. The walls have been treated as particles with infinite mass and the same property values have been used as for the particle-particle collisions. The parameters used for DEM collision model have been listed in Table 3.3.

Table 3.3: DEM Collisional Parameters

Coefficient of restitution (e)	Coefficient of friction (μ)	Spring constant (k_n, k_t)
0.90	0.10	800 N/m

Time step used

The time step is governed by the stability of inter-particle collisions. The maximum time step cannot exceed the collisional time scale for a particle pair. The critical time step for inter-particle collision is based on (Tsuji et al., 1993) as shown below

$$t_{cr} = \frac{\pi}{[k_n(1-\gamma^2)/m_{eff}]^{1/2}} \tag{3.2}$$

where γ is a constant given by

$$\gamma = \frac{-\ln(e)}{[\pi^2 + \{\ln(e)\}^2]^{1/2}} \tag{3.3}$$

where m_{eff} denotes the reduced or effective mass of the colliding particle pair. Using Eq. 3.2, the critical time step comes out to be 3.675×10^{-5} seconds. The particle and fluid time steps are kept the same at $1/10^{th}$ of the calculated critical time step.

Results and discussion

Single, double and triple jet configurations were tested with two different superficial velocities. Time averaging of the results has been performed for 3 seconds after leaving the first 5 seconds to let the bed reach a pseudo-steady state. Time averaged void fraction profiles have been compared to the experiments performed by (Brown, 2012). Noninvasive experimental techniques like Particle Image Velocimetry (PIV) and Digital Image Analysis (DIA) were used to measure bed solid fractions in the experiments. A predefined interrogation area is considered in PIV and the computations are done on statistically averaged displacement of a cluster of particles inside the interrogation area. The resolution provided by DEM is higher compared to PIV since it tracks each individual particle. Using Digital Image Analysis (DIA), the pixels obtained from PIV were converted into intensity matrices. The solid fraction values in the bed were calculated from the final intensity matrices obtained from DIA. Uncertainty in the experimentally calculated solid volume fractions are introduced through various correlation functions used in literature (Brown, 2012) to obtain solid volume fractions from intensity matrices.

Pressure Drop in the bed

Figure 3.2 shows the net pressure drop across the bed for the different jet configurations with two different superficial velocities. In a uniformly fluidized bed, the pressure drop across the bed is close to the weight of all the particles divided by the cross sectional area of the bed. But in a spouted/jetting bed, the pressure drop across the bed is lower because the whole bed is not mobilized. The particles in the dead zones do not participate in fluidization and mixing, and thus do not contribute to the pressure drop. The amount of dead zones forming is lower in multiple jet systems which give rise to a higher pressure drop across the bed compared to single jet systems.

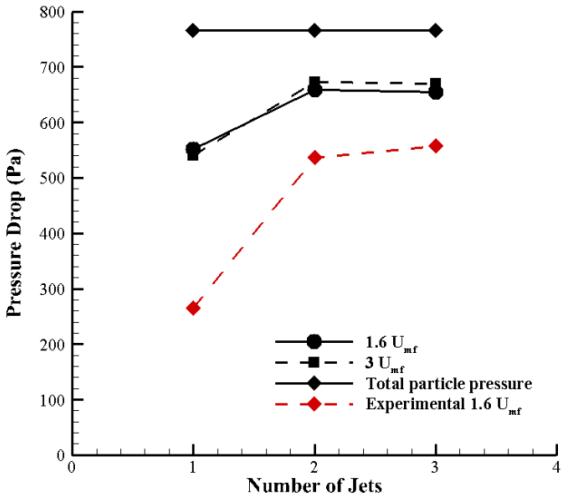

Figure 3.2: Net pressure drop across the bed

The pressure drop values are over-predicted by DEM-CFD simulations compared to experiments (Brown, 2012). This might be due to a larger channeling effect in the experiments, where the spout channels through the bed resulting in a reduced pressure drop across the bed. Conversely, it could also be caused by higher simulated drag forces leading to an increased pressure drop.

Single Jet System

Void Fraction

Figure 3.3 shows the time-averaged void fraction distribution for a single jet with 1.6 times the minimum fluidization velocity. The experimental void fraction profile matches closely with the profile obtained from the simulation. In both the experiment and the simulation, a central core of high void fraction values is observed. The core extends outwards with increasing height from the distributor plate. A small fountain is seen on the top of the jet core, which results from particles losing momentum and falling back into the bed. There are some differences between the experiments and computations, notably the larger fountain region in the computations, and the somewhat lower void fraction fanning out from the core region in the experiments.

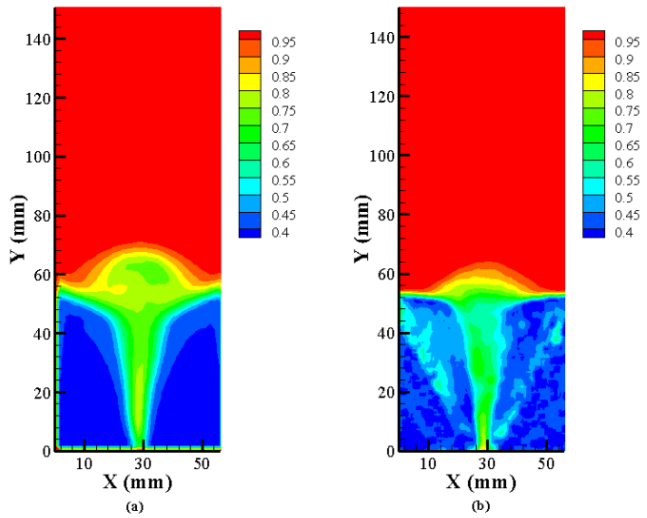

Figure 3.3: Void fraction contour plots for single jet and 1.6 U_{mf} (a) DEM Simulation, (b) Experimental (Brown, 2012)

Figure 3.4 shows an instantaneous snapshot of spout formation in the bed for the experiment and simulation, respectively for 3 U_{mf} single jet configuration. At this higher velocity, the spout penetrates higher into the freeboard and forms a distinct fountain. The corresponding time-averaged void fraction is plotted

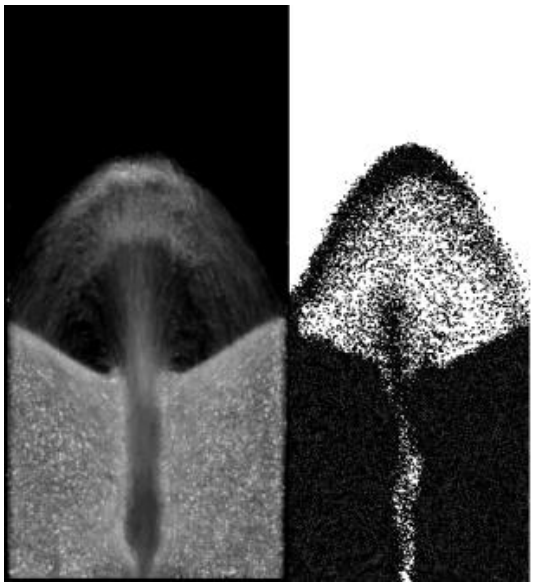

Figure 3.4: Instantaneous snapshot of spout formation in single jet configuration for 3 Umf (a) Experiment (Brown, 2012), (b) Simulation

in Figure 3.5. The simulations show a detached cloud of particles at a higher height compared to the continuous band of centrally located particles in the experiment. Considering the experimental uncertainty in obtaining the void fraction coupled with modeling uncertainties (in drag law), the void fraction agrees reasonably well between both procedures.

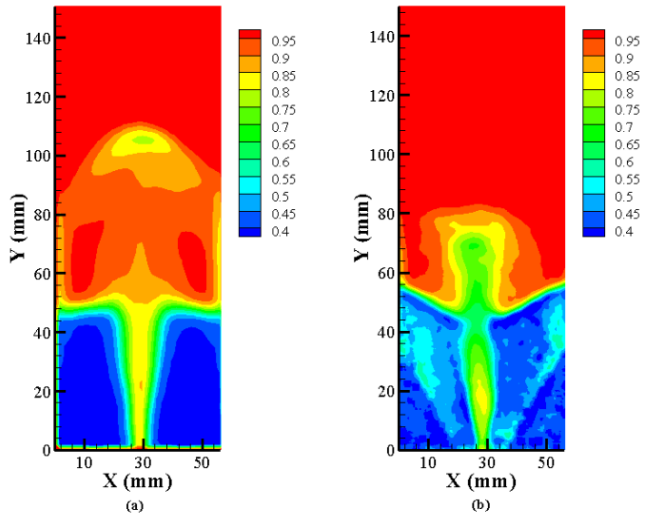

Figure 3.5: Void fraction contour plots for single jet and 3 U_{mf} (a) DEM Simulation, (b) Experimental (Brown, 2012)

Expanded Bed Height

The expanded bed height is measured based on the variation of cross-sectional average of solid fraction (ε_s) along the height of the bed. A representative cut off value of ε_s = 0.1 has been used in this study to identify the expanded bed height. Figure 3.6 shows the variation of averaged solid fraction along the height of the bed for single jet configuration with 1.6 U_{mf} and 3 U_{mf} , respectively. The expanded bed height for 1.6 U_{mf} comes out to be about 60.3 mm. For 3 U_{mf}, the cut-off void fraction of 0.1 is not representative of the expanded bed height because of fountain formation. Using this cut-off a value of 50 mm is obtained which is clearly not accurate at the higher superficial velocity. So, in order to calculate a more representative bed height, the total expanded volume in the bed is estimated. Summation of the volume of all the fluid cells having particles in them represents the total expanded volume of the bed.

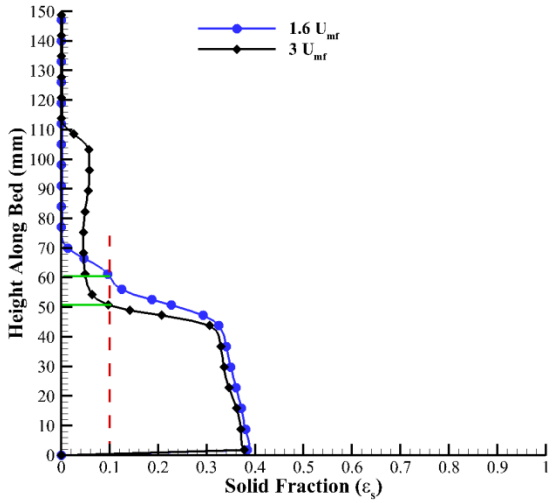

Figure 3.6: Variation of solid fraction along height for single jet

The expanded volume is then normalized by the total bed volume and multiplied by the total height of the bed setup to provide an estimate for the expanded bed height. The expanded bed height, following this technique, comes out to be about 88.5 mm for the 3 U_{mf} single jet configuration. Table 3.4 lists the expanded bed heights from the simulations and experiments.

Table 3.4: Expanded bed heights for single jet configuration

Expanded bed height, h_{exp} (mm)	1.6 U_{mf}	3 U_{mf}
From Simulation	60.3	88.5
From Experiment	55.4	-----

The comparison of expanded bed heights between simulation and experiment for 1.6 U_{mf} superficial velocities is fairly close with about 8% deviation between the two. The expanded bed height for the higher superficial velocity of 3 U_{mf} has not been documented in the experiments (Brown, 2012).

Particle Velocity

Having compared the general trend of fluidization with experiments, a detailed investigation of important fluidization properties such as particle velocity, solid

circulation rate and granular temperature is performed to gain a deeper insight into fluid-particle interactions in rectangular spouted beds. Figure 3.7 shows the particle velocity contour from the simulation for 1.6 and 3 times the minimum fluidization velocities, respectively.

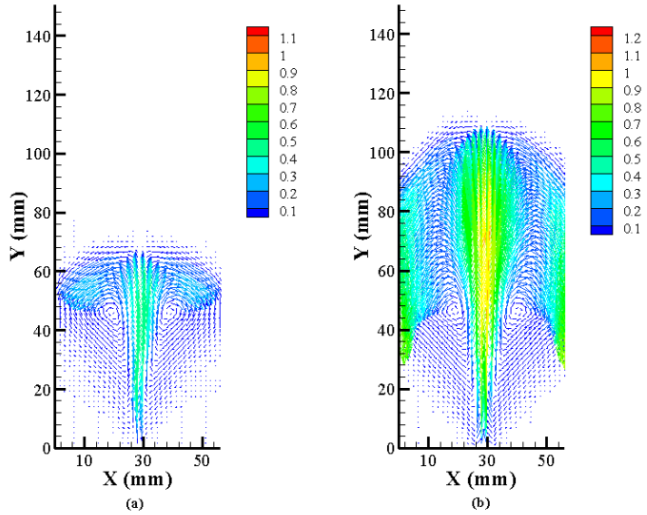

Figure 3.7: Velocity contour plots from simulation for single jet (a) 1.6 U_{mf}, (b) 3 U_{mf} (The colors represent the velocity magnitude)

From the figure, it is evident that the bed expansion for the higher velocity is considerably larger compared to the lower superficial velocity. The general trend of particle recirculation is similar for both superficial velocities, with a centrally rising core of high velocity particles giving way to downward falling particles in the annulus ($x \approx 45$ mm) region. A similar spouting pattern has been observed by (Takeuchi et al., 2004). This particle recirculation pattern is desired in jetting fluidized beds to aid in better heat and mass transfer through intense particle mixing. Comparing the dead zones in Figure 3.7, they show no significant difference between the two velocities considered. The dead zone region for the higher velocity is slightly smaller due to the higher downward velocities of the particles falling along the walls. The two counter rotating vortical structures present near the freeboard of the bed are considerably larger for the higher velocity. Figure 3.8 compares magnitudes of the axial velocities at different heights for the two different superficial velocities considered. For both superficial velocities,

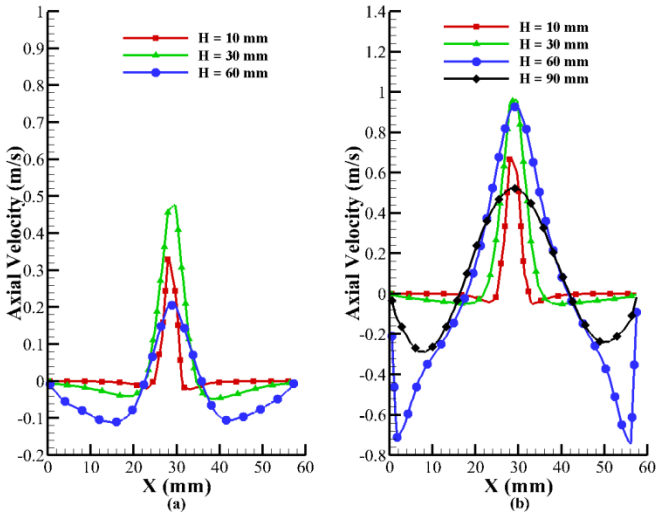

Figure 3.8: Axial particle velocity profiles at different heights for single jet (a) 1.6 U_{mf}, (b) 3 U_{mf}

the peak axial particle velocity at the jet core increases with height from the distributor plate to a value of approximately 4% of the jet velocity, before decreasing as more particles are entrained in the jet and they lose momentum with height. The bed height over which this happens is substantially larger for 3 U_{mf}. Similarly, the re-circulatory negative velocities increase in magnitude moving down from the freeboard, reaching a maximum in the annulus region (~4% of jet velocity) and then decreasing again as the particles get entrained in the jet or lose their downward momentum.

Granular Temperature

The granular temperature is a measure of particle randomness in the bed. The analogy could be made with the kinetic theory of gases, where the temperature of the gas is an average indicator of the kinetic energy possessed by the gas molecules. Similarly, in a granular medium, the granular temperature represents the average fluctuating kinetic energy possessed by the particulate medium. The following formulation has been used to calculate the granular temperature inside the bed.

$$\theta = \frac{1}{n} < C^2 > or\ \theta = \frac{1}{n}\frac{\sum_{i=1}^{N}(C_i^2)}{N} \tag{3.4}$$

where, θ, n, N represents the granular temperature in (m^2/s^2), the number of dimensions (n=2 for 2D and n=3 for 3D) and the number of particles inside a fluid cell, respectively. C_i represents the fluctuating component of the velocity of a particle over the average velocity of the particles contained inside a fluid cell.

A region having higher granular temperature is indicative of higher particle fluctuations and higher rate of inter-particle collisions. Knowledge of granular temperature distribution within the bed is important as it is a direct indicator of particle mixing and inter-particle heat transfer. Figure 3.9 shows the granular temperature distribution at different heights for single jet with varying superficial velocities. Unlike the axial velocity, granular temperature reaches a peak value in the jet core nearer to the distributor plate and decreases with height, while spreading laterally as the jet expands. The lateral spread of granular temperature is much larger at 3 U_{mf}, in the upper re-circulatory section of the bed due to the energetic downward falling particles.

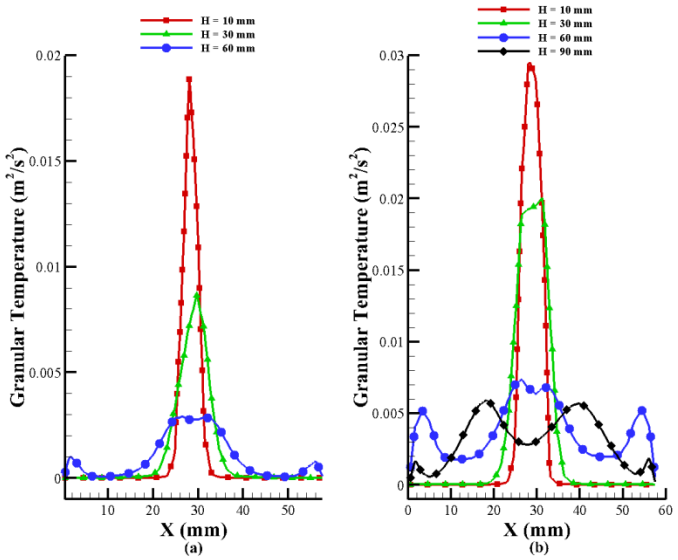

Figure 3.9: Granular temperature profiles at different heights for single jet (a) 1.6 U_{mf}, (b) 3 U_{mf}

The smaller magnitude of the granular temperature near the annulus zone for the 1.6 U_{mf} indicates a lack of inter-particle collisions for the particles falling down the sides of the walls. On the other hand, comparatively higher values of granular temperature can be seen in the annulus region for the 3 U_{mf} case. This indicates that mixing properties of a spouted/jetting fluidized bed depends strongly on the superficial velocities used for fluidization. Figure 3.10 shows the variation of granular temperature and axial velocity

with height at the jet center and in the annulus region for 1.6 U_{mf} and 3 U_{mf}, respectively. Both the axial velocity and the granular temperature rise sharply inside the jet core. The axial velocity levels out and then drops to zero at a higher height. The granular temperature on the other hand reaches a maximum at 10-15 mm from the distributor plate and drops sharply after that. This happens because the leveling out of the axial velocity leads to a decrease in the randomness of particle motion, thus reducing the amount of particle collisions at those heights. The increase in the granular temperature near the freeboard at the center of the jet is due to the collapse of the fountain at the top of the bed and increased collision between upward and downward moving particles. In the annulus region near the walls, the axial velocity drops to negative values due to the downward draft of particles moving along the walls. The granular temperature remains mostly at zero in the annulus zone at heights close to the distributor plate due to the presence of dead zones.

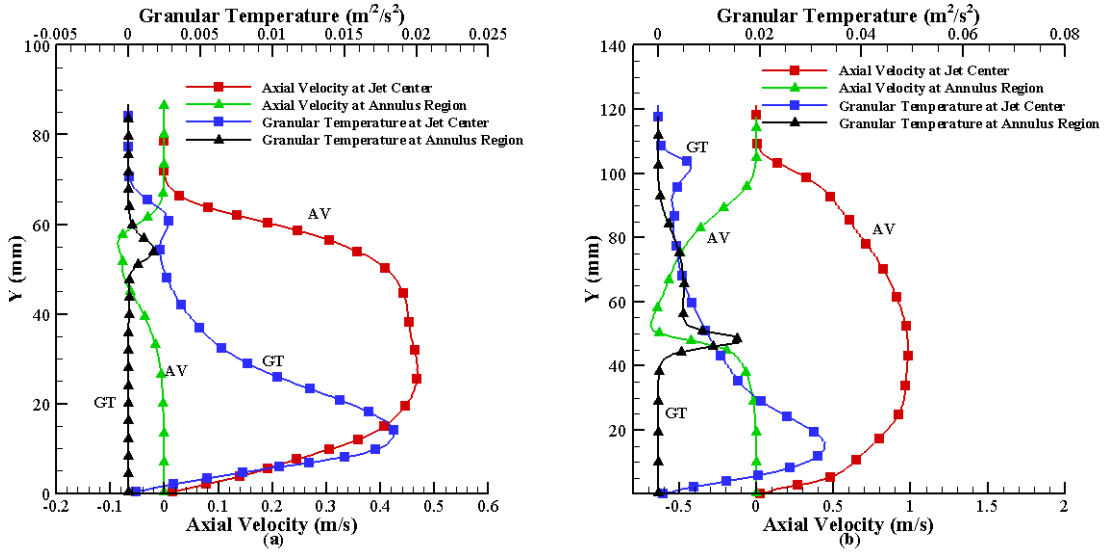

Figure 3.10: Granular temperature and Axial velocity variation with height for single jet (a) 1.6 U_{mf}, (b) 3 U_{mf}

At higher heights, small fluctuations in the granular temperature can be observed in the annulus region due to the formation of the vortical patterns of particle circulation. For both superficial velocities, the granular temperature in the annulus zone peaks at a height close to the maximum negative particle velocity.

Multiple jets

Double and triple jet configurations are simulated under two different superficial velocities of 1.6 U_{mf} and 3 U_{mf}, respectively. Here only the results for 3 U_{mf} are shown for brevity.

Void Fraction

Figure 3.11 shows the void fraction contour for double jet configuration with 3 times the minimum fluidization velocity. The close match with experimental void fraction contour provides a validation of the major fluidization characteristics of the double jets predicted by the simulation. Both the experiment and the simulation show a merging of jets close to the distributor plate. The jets merge together and form a gulf stream structure which eventually gets shaped into an inverted cup like formation at the top of the bed.

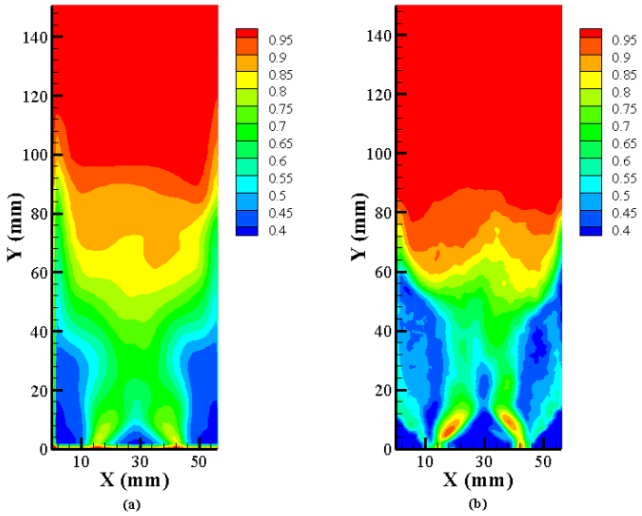

Figure 3.11: Void fraction contour plots for double jets and 3 U_{mf} (a) DEM Simulation, (b) Experimental (Brown, 2012)

The bed expansion is captured well in the simulation with some over prediction of the height to which the particles move up along the walls. Similarly, Figure 3.12 compares the predicted void fractions with experimental measurements for a triple jet configuration at 3 times the minimum fluidization velocity. A similar trend of the jets merging close to the distributor plate is observed for both the experiment and the simulation. In both dual and triple jet configurations, the central core of the jet is more dispersed in the simulation as compared to the experiment. One possible reason for this

could be a larger resistance encountered by the particles in the experiment against the walls which leads to the formation of slightly larger dead zones in the experiment, effectively decreasing the area of the central core of the jet. Experimental uncertainty in computing the void fraction could also contribute to the observed differences. Overall, the general trend of spouting and fluidization for multiple jet configurations is captured reasonably well by the DEM-CFD simulations.

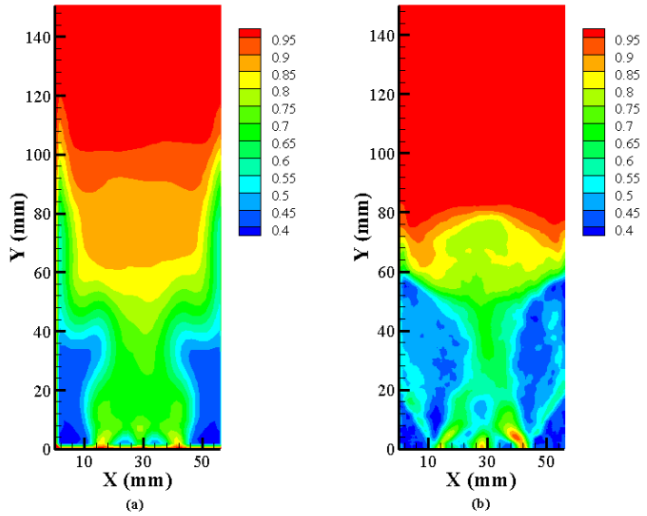

Figure 3.12: Void fraction contour plots for triple jets and 3 U_{mf} (a) DEM Simulation, (b) Experimental (Brown, 2012)

Expanded Bed Height

Figure 3.13 shows the variation of solid fraction profile averaged across distributor cross-sections with height for double and triple jet configurations and 3 times the minimum fluidization velocity.

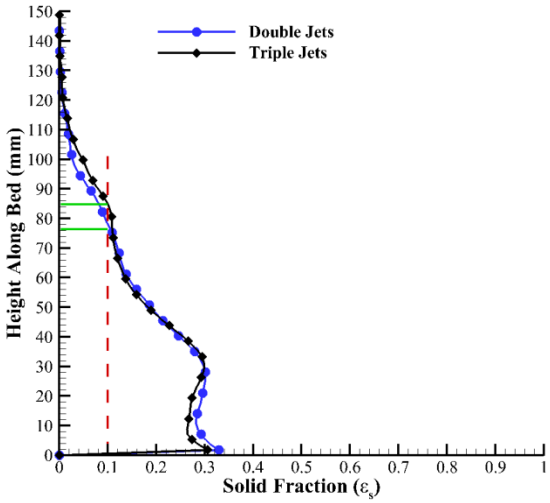

Figure 3.13: Variation of solid fraction along height for multiple jets

The solid fraction variation for double and triple jet configurations is almost similar to each other. The expanded bed height calculated from a cut off solid fraction value of 0.1 is close to 78.1 mm for the double jet configuration and 84.9 mm for the triple jet configuration. Table 3.5 lists the expanded bed heights from the simulations and available experiments. It can be seen that the simulations and experiments agree to within 10-15%.

Table 3.5: Expanded bed heights for multiple jet configurations

Jet Configuration	Double Jets		Triple Jets	
Superficial Velocity	1.6 U_{mf}	3.0 U_{mf}	1.6 U_{mf}	3.0 U_{mf}
Expanded Bed Height from Simulation, h_{exp} (mm)	58.22	78.09	63.35	84.93
Expanded Bed Height from Experiment (mm)	50.75	na	58.74	na

Particle Velocity

Figure 3.14 shows the particle velocity distributions for the double and triple jet configurations. The vectors are colored based on the absolute magnitude of particle velocity. The general circulatory pattern is quite similar to the single jet, except that the velocity magnitudes are lower in the core and that the dead zones which exist in the single jet are nearly eliminated. The triple jet has a slightly higher particle velocity in the

jet core as well as in the annulus region indicating that adding a central jet imparts additional momentum to the upward moving particles, even though with the same superficial velocity each jet has a lower velocity. As in the single jet, bed circulation is characterized by two distinct counter rotating vortical structures centered at about 40 mm from the distributor plate which entrain the solids back into the core flow. Figure 3.15 shows the variation of axial particle velocity at different heights for the double and triple jet configurations. The particle velocity at the jet core is higher for the triple jet configuration with the maximum value close to about 0.3 m/s at a height of 60 mm compared to 0.25 m/s for the dual jets. Both are less than the peak velocity of about 1 m/s in the single jet configuration. At a height of 10 mm, two peaks can be observed in the velocity profile for the double jet configuration and three peaks for the triple jet. The merged jets exhibit a single peak at 30 mm in the bed. The larger downward negative particle velocities at a height of 60 mm for the triple jets points to the fact that the circulation strength of the vortices for the triple jets must be higher compared to the double jets.

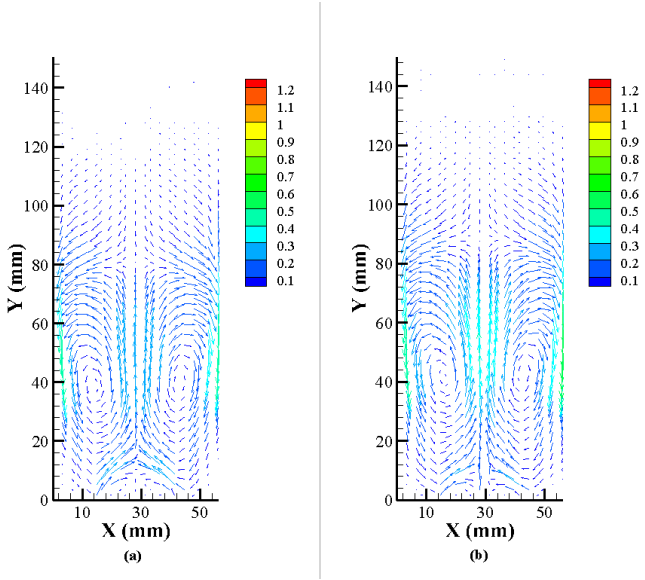

Figure 3.14: Velocity contour plots from simulation for 3 U_{mf} (a) Double jets, (b) Triple jets

As in the single jet, the entire spouting mechanism can be looked upon as a system of two elongated counter rotating vortices, engulfing, ejecting and entraining particles in their trajectories.

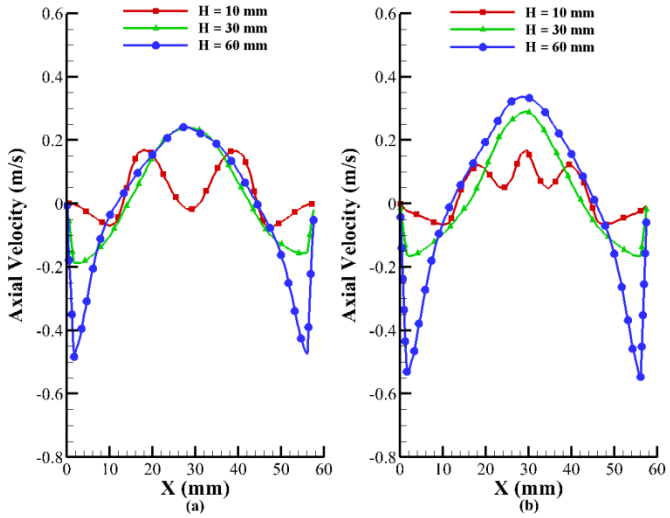

Figure 3.15: Axial particle velocity profiles at different heights for 3 U_{mf} (a) Double jets, (b) Triple jets

Granular Temperature

Figure 3.16 shows the granular temperature profiles at different heights for multiple jet configurations at 3 times the minimum fluidization velocity. Comparing Figure 3.16 with Figure 3.9(b) shows that the maximum granular temperature for the single jet case is almost 4 times larger than the maximum value attained by the triple jet system. The flatter granular temperature profile in case of double jets shows that due to the absence of a central jet, the jets diffuse quickly and the fluctuations in the particle velocities get spread out evenly. The granular temperature profile in the annulus zone is comparable between the double and the triple jet systems. At a height of 10 mm from the distributor plate, however, the granular temperature in the core of the jet for the triple jet system is almost 4 to 5 times larger than the double jet system. This is because the particles in the jet center experience large velocity fluctuations due to increased drag offered by the direct impingement of the central jet. This trend is in line with the single jet configuration in Figure 3.9(b). At higher heights, due to particles losing momentum at the center and falling down along the walls, the granular temperature is higher in the annulus zone compared to the center of the jet.

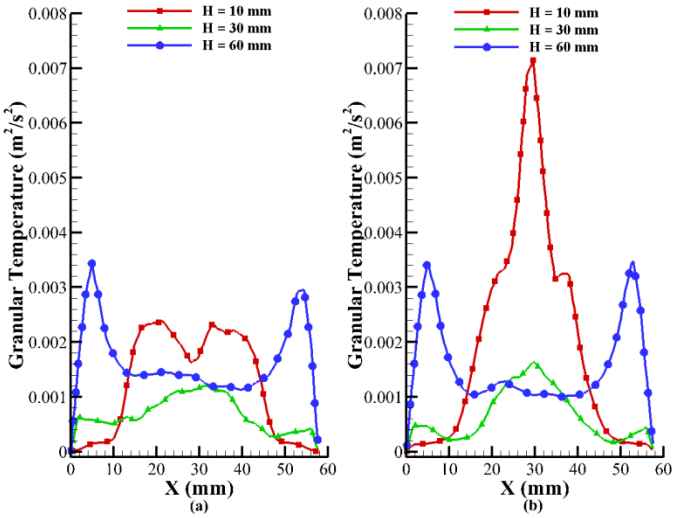

Figure 3.16: Granular Temperature profiles at different heights for 3 U_{mf} (a) Double jets, (b) Triple jets

Figure 3.17 shows the variation of the axial velocity and granular temperature with height along the center of the jet and annulus region, respectively, for 3 times the minimum fluidization velocity. From Figure 3.17, it can be seen that the variation in particle axial velocity along the jet center or bed center is almost similar for both the double and triple jet configurations. The particle axial velocity in the annulus region follows a similar trend for both. The granular temperature profiles for the double jet configuration are flat both in the jet core and the annulus region without much variation. Inclusion of a central jet in the triple jet configuration increases the granular temperature in the jet core, which decreases with increasing height. The granular temperature in the annulus zone for the triple jet shows similar trend of a flat profile like the double jet configuration.

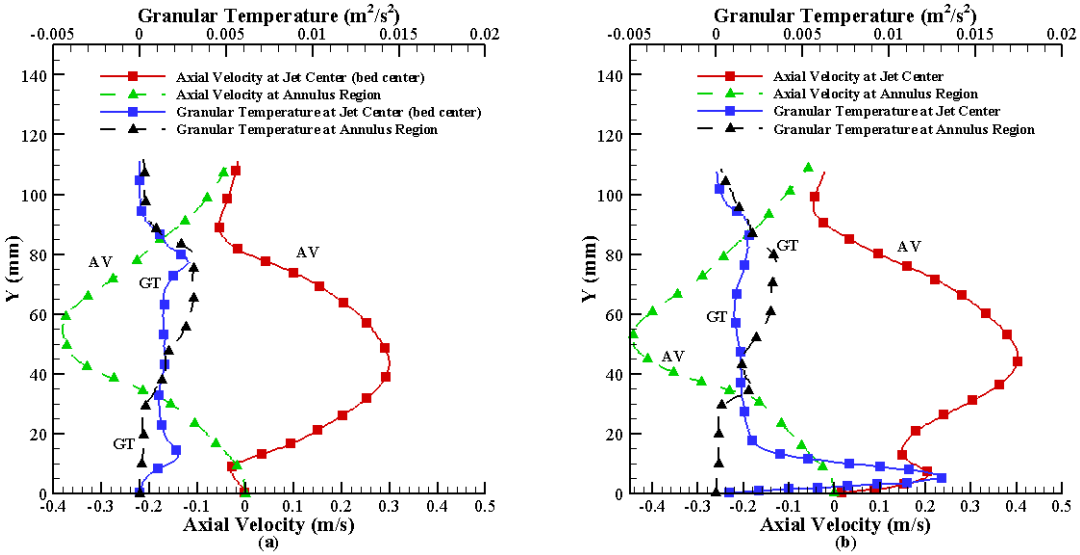

Figure 3.17: Granular temperature and Axial velocity variation with height for 3 U_{mf} (a) Double jets, (b) Triple jets

Analysis of Solid Circulation/Mixing

Various experimental techniques have been used by researchers in the literature (Mostoufi and Chaouki, 2001; Wirsum et al., 2001; Zhang et al., 2009; Zhang et al., 2011; Zhong et al., 2006; Zhong et al., 2007), to estimate mixing in a fluidized bed setup. Most of them follow a procedure of injecting tracer particles and following them throughout the flow in the bed. Calculation of solid diffusivities using tracer particles in the axial as well as radial directions has been proposed by (Mostoufi and Chaouki, 2001). They used Radioactive Particle Tracking (RPT) to track a single tracer particle in a cylindrical bed. Although tracking tracer particles provide information about solid mixing, it can be difficult and cumbersome to calculate the concentration of tracer particles at different locations inside the bed. Some new techniques such as image processing and calculation of Shannon entropy have also been used in the literature to estimate particle mixing (Zhang et al., 2008; Zhang et al., 2011). The terminology "mixing" is generally used for systems comprising of more than a single sized distribution of particles or particles with tracers for characterization. But in systems having mono-dispersed particles without any tracers, solid mixing can be generally investigated by quantifying the movement of particles in the bed, also known as solid circulation. Hence the terms "solid circulation" and "mixing" have been used

interchangeably in the present study. Calculation of solid circulation rates has been proposed using the counter-current model by (Geldart, 1986; Gidaspow, 1983; JJ, 1967; Morgan Iii, 1985). A concept of internal and gross solid circulations has been proposed as the main mechanisms of mixing in gas fluidized beds by (Moslemian, 1987). In a gross circulation, particles move from near the distributor plate towards the freeboard and then fall downward due to gravity ultimately reaching the distributor plate regions. This causes the particles to move in a closed loop almost of the scale of the bed thus enhancing solid circulation. Internal circulations on the other hand are of smaller scales where particles tend to form localized convective loops. Internal circulations give rise to localized solid mixing. In this study, conventional methods of estimating the mixing characteristics using horizontal mass flux distributions and the counter-current method are compared to measures of convective and diffusive mixing in the bed.

Horizontal Mass Flux

Horizontal mass flux gives an idea of lateral mixing in the bed by calculating the rate at which particles are entrained in the jet(s). Figure 3.18 shows the horizontal mass flux calculated at different heights according to the following formulation.

$$\dot{m}_x = \rho_p (1-\varepsilon) A \vec{v}_x \tag{3.5}$$

where, A and $\vec{v}_x$ are the area normal to the horizontal velocity of the particles and the aggregate horizontal particle velocity in a fluid cell, respectively.

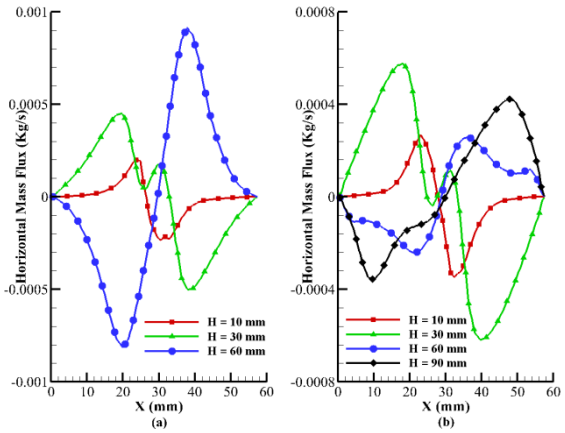

Figure 3.18: Horizontal solid mass flux profiles at different heights for single jet (a) 1.6 Umf, (b) 3 Umf

At the base y= 10 and 30 mm, the horizontal mass flux is positive at x<30 mm and negative for x>30 mm, signifying entrainment into the core of the jet. As the jet spout loses momentum higher in the bed, particles are transported from the center of the bed to the annular region as indicated by the profiles at y=60 and 90 mm facilitating the recirculation of the particles in the bed. It is interesting to note that while the horizontal mass flux entrained into the spout region is higher at 3 U_{mf}, the mass flux ejected at the top of the bed from the spout is lower. This is due to the formation of the fountain at the higher velocity which ejects particles out of the bed and which does not contribute to the horizontal flux.

Figure 3.19 shows the horizontal mass flux calculated at different heights for the multiple jet configurations. Comparing Figure 3.19 to Figure 3.18(b), a marked difference in the magnitude of the horizontal flux exists. The horizontal flux for the multiple jet systems is orders of magnitude larger than a single jet system with the same superficial velocity. This shows that much higher particle entrainment occurs close to the distributor plate with multiple jet configurations. This gives rise to a higher amount of lateral/radial mixing compared to a single jet setup. But at the same time, the mass flux of particles leaving the jet core at higher heights is also notably larger in a multiple jet configuration compared to single jet set up. Overall, this gives rise to a lower net particle entrainment in multiple jet configurations and thus lower amount of axial mixing compared to a single jet configuration. This is also validated by calculating the total solid circulation rates in different jetting configurations in a later section. The reason behind the higher horizontal mass flux near the distributor plate for multiple jets is that jets from the sides impart momentum to the particles sideward forcing them to get entrained in the centrally formed core. A single jet only imparts vertical momentum to the centrally located particles. Entrainment from the sides in a single jet is solely governed by the slow counter rotating vortical structures. On the other hand, in a multiple jet system, smaller dead zones are formed which aids in more particles to be entrained in the core near the distributor plate.

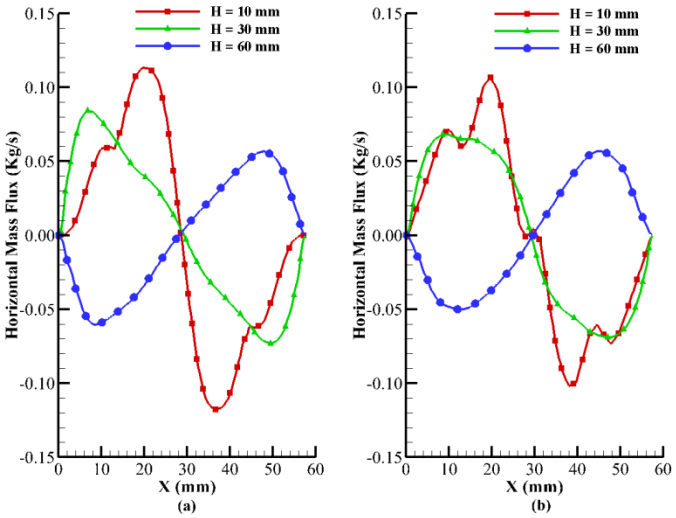

Figure 3.19: Horizontal solid mass flux profiles at different heights for 3 U_{mf} (a) Double jets, (b) Triple jets

Comparing Figure 3.19(a) to Figure 3.19(b) shows no significant differences in the solid fluxes between the double and triple jet systems. This shows that the centrally located jet in the triple jet configuration does little to affect horizontal particle entrainment/flux into the jet core from the annulus region.

Counter Current Model

A measure of solid circulation rates/axial mixing has been calculated in this study using the counter-current model proposed by (Geldart, 1986; Gidaspow, 1983; JJ, 1967; Morgan Iii, 1985). The net solid circulation rate as proposed in the counter-current model is given by the following formulation.

$$\dot{m}_{x,tot} = \rho_p \times (\varepsilon_{s,b}) \times (f_{r_{neg}}) \times (|v_{neg,avg}|) \times (A_d) \tag{3.6}$$

where, $\varepsilon_{s,b}$ represents the bulk solid fraction of the bed which is calculated based on the expanded height of the bed as follows

$$\varepsilon_{s,b} = \frac{mbed}{\rho_p \times h_{\exp} \times A_d} \tag{3.7}$$

where, $mbed, h_{\exp}, A_d$ represents total mass of particles inside the bed, expanded bed height and area of the distributor plate, respectively. In Eq. (3.6), $f_{r_{neg}}$ and $|v_{neg,avg}|$ represents the fraction of the bed moving downwards and the average downward velocity of the particles in the bed, respectively. Table 3.6 lists the values of the quantities used in calculating the solid circulation rates given by Eq. (3.6).

Table 3.6: Values used in calculating solid circulation rate

Jet Configuration	Single Jet		Double Jets		Triple Jets	
Superficial Velocity	1.6 Umf	3.0 Umf	1.6 Umf	3.0 Umf	1.6 Umf	3.0 Umf
Bulk Solid Fraction ($\varepsilon_{s,b}$)	0.518	0.353	0.536	0.401	0.493	0.368
Fraction of bed moving down ($f_{r_{neg}}$)	0.549	0.451	0.558	0.470	0.461	0.462
Average negative velocity ($\|v_{neg,avg}\|$) (m/s)	0.0328	0.117	0.0178	0.0623	0.0349	0.0671

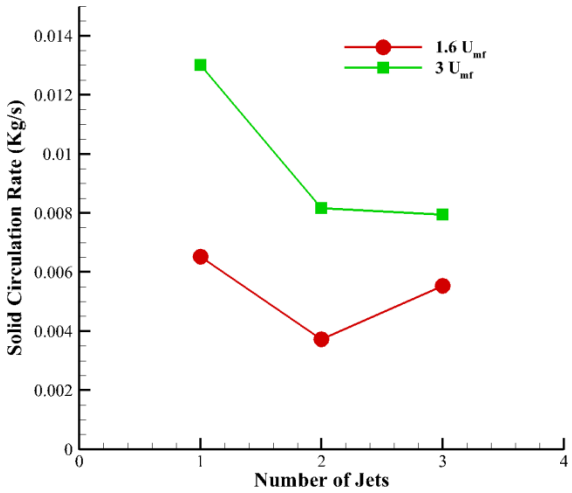

Figure 3.20: Solid Circulation Rate

Figure 3.20 shows that the solid circulation rate using Eq. (3.6) is highest for the single jet with 3 U_{mf}. With an increase in the number of jets, the solid circulation rate decreases which is consistent with the findings by (Agarwal et al., 2011a), with the exception of the triple jet configuration for 1.6 U_{mf}. The solid circulation rates for 1.6 U_{mf} cases are considerably smaller compared to 3 U_{mf} cases, proving that the solid circulation rates increase with an increase in superficial velocity (Agarwal et al., 2011a). This shows that even with higher horizontal mass fluxes/lateral mixing near the distributor plate for multiple jet configurations, the total solid circulation rates/axial mixing are lower compared to single jet configuration at the same superficial velocities.

Convective and Diffusive Mixing

The horizontal mass flux and the counter-current model give measures of mixing based on the horizontal entrainment of particles into the jet and the vertical downward movement of particles, respectively. Another measure of mixing based on the three-dimensional transport of solids in the bed in proposed. The measure captures two major processes inside the bed: a) the global circulation of particles (Convective rolls), b) small scale localized mixing. These measures have no directional bias and are average indicators of overall mixing in the bed and are applicable to jetting as well as uniform fluidized beds.

a) Convective mixing

Particle circulation patterns in spouted/jetting fluidized beds give rise to axial and radial mixing of particles inside the bed. This mixing can be characterized by

$$P_c = \sum_{Ncells} (|\dot{m}_x|v_x^2 + |\dot{m}_y|v_y^2 + |\dot{m}_z|v_z^2) \tag{3.8}$$

where, P_c, $\dot{m}_i$ and v_i (with i = x,y,z) represent the measure of convective mixing in Watts, averaged particle mass flow rate in a fluid cell in each of x, y and z directions, respectively, and averaged particle velocity magnitude in a fluid cell along x, y and z directions, respectively. $Ncells$ is the number of fluid cells in the entire domain. Figure 3.21 shows the distribution of convective strength for different jet configurations with 1.6 times the minimum fluidization velocity.

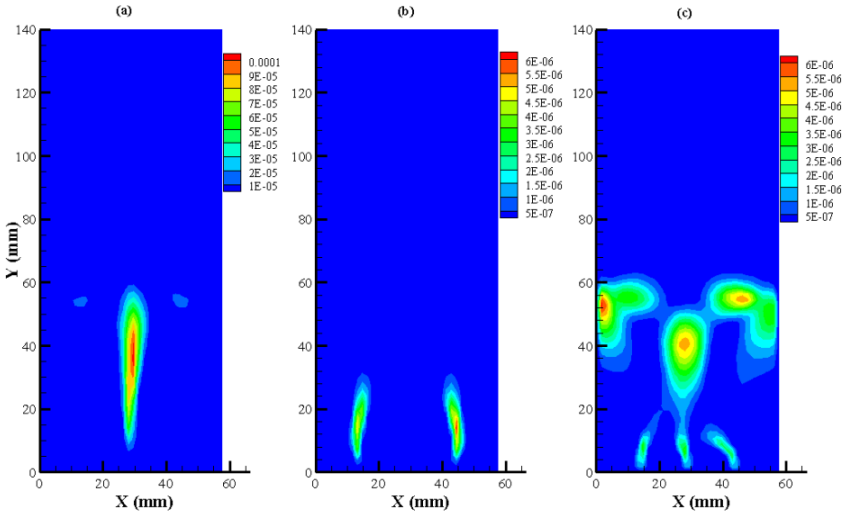

Figure 3.21: Figure showing comparative convective power for 1.6 U_{mf} (Watts) (a) Single jet, (b) Double jets, and (c) Triple jets

It is evident from Figure 3.21 that the particles in the single jet configuration exhibit the largest convective power in the central jet. Surprisingly, the convective power imparted to the particles reduces drastically for a double jet configuration indicating that the absence of a centrally located spout prevents the particles from forming strong circulation patterns. Even though a substantially high horizontal flux is present for a double jet system compared to a single jet system, the large horizontal flux of particles is not supported by a strong vertical momentum in the bed. A triple jet system on the other hand revives some of the centrally acting upward momentum due to the introduction of a central jet. This in turn gives rise to a higher overall convection compared to a double jet system. A similar trend can be observed for the higher superficial velocity of 3 times the minimum fluidization velocity, although the power expended in particle circulation is many times larger than the lower superficial velocity cases as shown in Figure 3.22 .

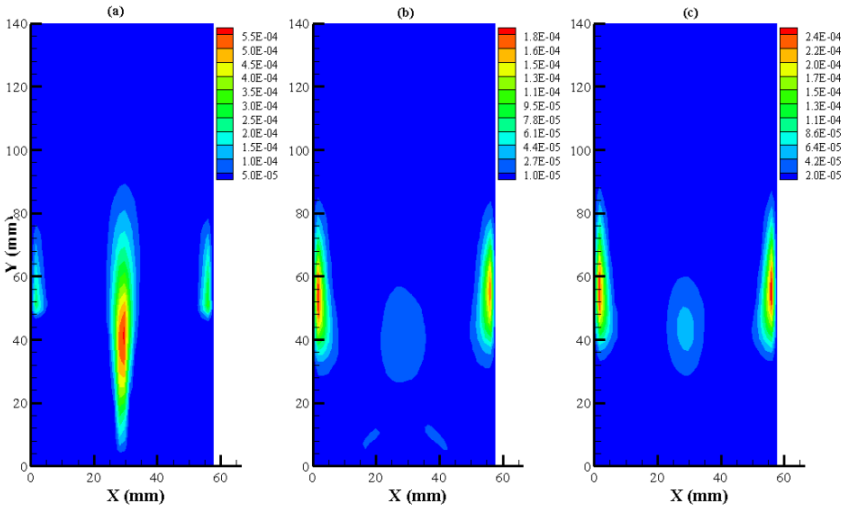

Figure 3.22: Figure showing comparative convective power for 3 U_{mf} (Watts) (a) Single jet, (b) Double jets, and (c) Triple jets

Figure 3.22 shows much higher solid convection near the walls compared to 1.6 U_{mf}. Due to the higher jet velocities, the jets merge earlier near the distributor plate in (b) and (c) compared to the lower superficial velocity multiple jet configurations. Figure 3.23 plots the net strength of solid convection for different jet configurations for the two superficial velocities used. The trend is similar to that seen in Figure 3.20 with maximum convective strength evident in the single jet configuration with 3 U_{mf}. As with the solid circulation rate, the solid convective power decreases for double jet configurations for both the higher and lower superficial velocities. For the triple jet configuration, there is a decrease in solid circulation rate from a double jet configuration for 3 U_{mf}, whereas the solid convection increases slightly over the double jets for the same superficial velocity. This might be because of the vertical momentum imparted to the centrally moving particles. Overall, the convective power as defined in Eq. (3.8) can also be used as an indicator of mixing inside the bed.

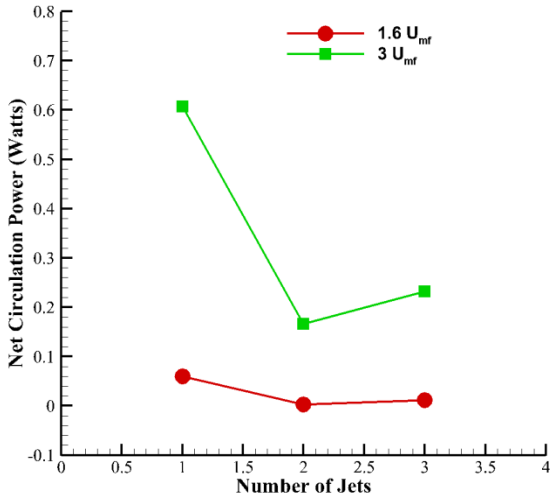

Figure 3.23: Plot showing comparative solid circulation power through bulk convective particle motion

b) Power expended in particle velocity fluctuations/Diffusive mixing

While convection in Eq. (3.8) is a measure of large scale motion of particles, the granular temperature of particles is a measure of small scale localized diffusive mixing.

$$P_d = \sum_{Ncells} \dot{M} \times \theta \tag{3.9}$$

where, $P_d, \dot{M}, \theta$ represents rate of energy diffusion through particle velocity fluctuations in Watts, net particle mass flow rate inside a fluid cell and granular temperature of particles inside a fluid cell, respectively. Figure 3.24 shows the variation of power dissipated through diffusive mechanisms. It is clear from Figure 3.24 that the single jet system with 3 times the minimum fluidization velocity diffuses the highest amount of power through localized particle velocity fluctuations. The trend is similar to that found in Figure 3.23 for convection. The double jet system has the lowest amount of diffusive mixing for both the 1.6 and 3 times the minimum fluidization velocity cases. With the introduction of a central jet, the power diffused due to velocity fluctuations increases in a triple jet system over double jets.

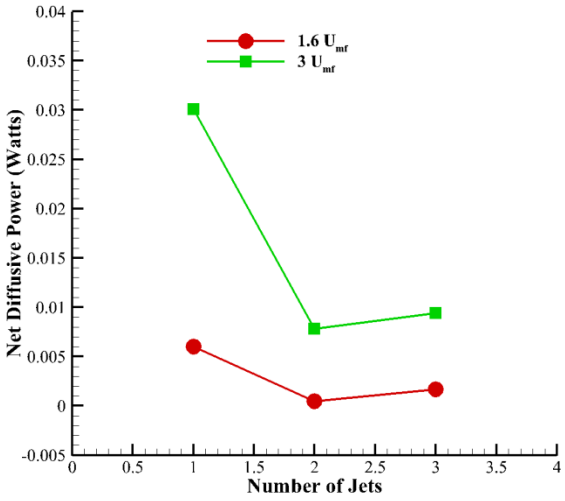

Figure 3.24: Plot showing comparative power diffusion through localized particle velocity fluctuations

Horizontal mass flux, solid circulation rate, and power expended in the bed have been measured, respectively, in order to perform a detailed investigation of particle mixing/circulation pattern in a flat bottomed jetting bed set up. Even though a higher horizontal mass flux/lateral mixing is predicted with larger number of jets, the net solid circulation/axial mixing is low compared to single jet setup at the same superficial velocity. This is because unlike single jet configurations, the particles fail to recirculate in counter rotating vortical patterns for multiple jets, which ultimately leads to lower solid circulation rates. A power analysis of the beds also predicts trends similar to that predicted by the solid circulation rates.

Summary and Conclusions

A detailed numerical study using CFD-DEM has been performed on lab-scale flat spouted beds with single, double and triple jet configurations with different superficial velocities. Important characteristics of the bed such as pressure drop, expanded bed height, void fraction, solids velocity, and granular temperature are analyzed. The predicted void fractions are validated with experimental results. The particle axial velocity at jet center increases with an increase in superficial velocity for single jet system. For the multiple jet systems, inclusion of a central jet in the triple jet system imparts additional momentum to the central particles causing a higher axial particle

velocity at the jet center compared to the double jet configuration for the same superficial velocity of 3 U_{mf}. Comparing the particle axial velocities at 3 U_{mf}, merging of jets for multiple jet systems diffuse the axial velocity of the particles, thus lowering it compared to a single jet system. The pressure drop across the bed is smaller for a single jet system compared to multiple jet systems for both superficial velocities due to a higher proportion of dead zones around the bed corners, but does not vary significantly with superficial velocities. The experimental pressure drops are smaller in magnitude due to the channeling effect of the jets which is not evident in the computations.

Mixing in the beds is analyzed using different criteria based on horizontal flux distributions, solid circulation rates using the counter-current model, and criterion based on power expended in convection and diffusion of solids. The horizontal mass flux closer to the distributor plate is weakly affected by a change in the superficial velocity as observed for single jet configuration. At higher heights however, the horizontal mass flux increases with an increase in superficial velocity. Considerably higher horizontal mass flux is observed for multiple jet configurations, both near the distributor plate and higher in the bed, compared to a single jet configuration for a superficial velocity of 3 U_{mf} . The central jet in the triple jet configuration does not affect horizontal particle entrainment/flux into the jet core from the annulus region. Solid circulation rates in the counter-current model increase with an increase in superficial velocity while showing a general decreasing trend with an increase in the number of jets. A power distribution analysis is performed to find an alternative method of investigating mixing in a spouted bed. The single jet configuration with the higher superficial velocity shows the highest solid convective power as well as the highest solid diffusive power indicating a better overall solid circulation in the bed, which is also verified by the counter-current model. Both the convective and diffusive power decreases with a decrease in superficial velocity for all the possible jet configurations studied. These results provide us with a fundamental understanding of the fluidization process for jetting systems and enable us to make prudent design decisions.

Chapter 4 Discrete Element Modeling and Validation of Fluidized Bed with Multiple Jets

Introduction

Jetting fluidized beds are used widely in various industries for good mixing and faster chemical reaction properties. The mass and heat transfer rates are enhanced in fluidized beds with multiple jets. Particle entrainment inside the jets enhances the solid-gas contact in the region above the distributor plate of a jetting fluidized bed leading to improved bed characteristics. Hence it is important to analyze the general flow hydrodynamics of the jetting zone. Several researchers have used experimental techniques to study the cold flow properties of jetting fluidized beds. A measurement of solid circulation in large jetting fluidized beds was conducted by (Yang et al., 1986). In their study, they employed high speed motion capture along with a force probe to study the bubble characteristics. This was the first study attempted at measuring the bubble characteristics, simultaneously with solid circulation in a large commercial scale jetting fluidized bed. A systematic study of the motion of solids, solid flow rates and local void fraction fluctuations in a large jetting fluidized bed has been done by (Ettehadieh et al., 1988). They analyzed local bed density fluctuations and determined that the solid circulation rate increases linearly with increasing jet velocities. The effects of a single bubble in the distributor regions of a fluidized bed have been studied by (Yates et al., 1984). They used X-ray analysis to study the gas bubbles entering a fluidized bed reactor. The flow characteristics of a large jetting fluidized bed with two nozzles have been studied by (Guo et al., 2000). They proposed an empirical correlation for the jet penetration depth based on experimental data. Fluidization regime maps were developed by (Sutanto et al., 1985), including fixed, bubbling, jet in fluidized bed, spout fluidization and spout with aeration. Flow regime transitions and jet penetration depth were studied in a binary mixture setup by (Guo et al., 2001). They presented a new correlation for predicting the jet penetration depth for different annular gas flow rates. Significant amount of research has been conducted on a single jet by (Basov et al., 1969; Huang and Chyang, 1991; Zhang et al., 2002). Recently (Guo et al., 2010) investigated the jet penetration depth and particle concentration profiles using optical fiber probes and acoustic assistance.

Getting detailed information about the entire space of the bed is difficult in the experiments, which generally requires invasive procedures that can alter the flow and particle dynamics in the bed. A full scale numerical simulation is often desired to understand the complicated gas-particle dynamics inside a jetting fluidized bed. Recent advances in computational capabilities have given rise to a wide variety of modeling strategies to model granular flows. Among the available modeling approaches, the most widely used are the Two Fluid Model (TFM) and the Discrete Element Model (DEM), respectively. TFM is an Eulerian-Eulerian approach where both the fluid and the particles are considered to be two distinct interpenetrating continua. This approach is suitable for modeling large industrial scale gasifiers with low to moderate resolution of the flow field. DEM on the other hand is a high fidelity Eulerian-Lagrangian approach which tracks each individual particle, providing a much better flow field resolution compared to TFM. DEM is more suited for small lab scale simulations as it is restricted by the computationally expensive and extremely time consuming calculations. DEM was first developed by (Cundall and Strack, 1979) and later coupled with CFD by (Tsuji et al., 1993). Since then, DEM has found its place as a viable modeling approach in a wide variety of applications including segregation of binary mixtures (Feng et al., 2004; Feng and Yu, 2010), capturing bubble dynamics (Kobayashi et al., 2000; Pain et al., 2002; Rong et al., 1999), modeling behavior of cohesive particles (Iwadate and Horio, 1998; Mikami et al., 1998) and so on. A comprehensive review focused on the research work done using DEM has been given by (Deen et al., 2007; Zhou et al., 2010; Zhu et al., 2008).

There have been several attempts in modeling jetting fluidized beds by several researchers. Semi-empirical correlations like fluidized bed grid zone model and Kunii-Levenspiel bubbling bed model were combined together and applied to a jetting fluidized bed coal gasifier by (Kimura and Kojima, 1992). They compared the local gas compositions in the grid zone to experimental results. Gas-solid flow behavior was investigated by (Szafran and Kmiec, 2004) for a spouted bed dryer with a draft tube. They utilized the Eulerian-Eulerian multi-fluid model to simulate the heat and mass transfer occurring during the drying of grain in a spouted bed. A combined numerical and experimental approach to investigate the gas-solid flow dynamics was done by (Zhang et

al., 2002). They validated their numerical model with experimental results in a 2D spouted bed with a single central jet. Using the Eulerian method, (Boemer et al., 1997) simulated bubble formation at a jet of a two dimensional fluidized bed. DEM was first used by (Tsuji et al., 1993) to simulate a 2D jetting fluidized bed with the depth of the bed being equal to a single particle diameter. The fluidization pattern compared well with their experiments with a slight over prediction of the calculated pressure drop signal by DEM. 2D CFD-DEM simulations, with the bed depth being equal to a single particle diameter, have been conducted by (Feng et al., 2004; Goldschmidt et al., 2004; Hoomans et al., 1996; Hoomans et al., 2001; Mikami et al., 1998; Tsuji et al., 1993). Recently, flow regime maps were reported by (van Buijtenen et al., 2011) using a DEM study, positron emission particle tracking and particle image velocimetry for double and triple spout fluidized beds. Numerical simulation and verification were done by (Ruoyo et al., 1996) on a jetting fluidized bed.

In spite of the vast amount of data available on fluidized beds, numerical simulation of jetting fluidized bed with more than three jets has not been investigated extensively. In this work, we apply the Discrete Element Model (DEM) methodology to a 9 jet bed. Both two and three dimensional computations have been performed. A full scale 3D simulation of multiple jets comprising millions of particles has not been attempted previously. The computational results are compared with experimental measurements from (Agarwal et al., 2011b) and (Agarwal et al., 2011a). Particle fluxes, solid fraction and particle velocities near the jets are some of the quantities compared. The chapter is structured as follows. The methodology section provides an overview of DEM followed by a brief outline of the experimental setup. The next two sections give the computational details and results, respectively, followed by a concluding section.

Experimental setup

The bed was 0.76m high and 0.25m wide with a depth of 12.7 mm in the experiments. High optical clarity glass was used to make the bed walls. The back side of the bed had a light absorbing black sheet. Two halogen lamps each rated 500 W were used to illuminate the bed homogeneously. Double frame digital images of the bed were taken using a Flowsense MKII (4 Megapixel) PIV camera. Detailed information on the experimental setup is given in (Agarwal et al., 2011b).

Computational Details

Details of Jets

The computational results are validated with experiments done by (Agarwal et al., 2011b). Both 2D and 3D simulations have been performed. In the 2D computations, the depth of the bed has been reduced from 12.7 mm to a single particle diameter. This has been done to reduce the number of particles being simulated and in essence reducing the computational time. The width of the bed has been kept the same as in the experiment. In the 3D computation, the full experimental geometry has been simulated.

A single test case having 9 jets has been simulated and compared with the experiment. 550 μm particles have been used in both the experiment and the simulations. The superficial velocity has been kept the same as in the experiment. Table 4.1 lists the details of the cases being simulated.

Table 4.1: Jet Properties (W = Width, D = Depth)

Case	Number of jets	Superficial velocity (m/s)	Jet velocity (m/s)	Jet Dimensions	Jet area (m^2)	Jet pitch (m)
A1(2D)	9	0.315	4.37	W: 2.015 mm D: 0.550 mm	1.11E-6	0.028
A1(3D)	9	0.315	35.28	W: 2.015 mm D: 1.590 mm	3.20E-6	0.028

Case A1 corresponds to distributor type A1 in the experiment. In the experiment, circular holes were used for the jets. Simulating circular holes in the computational framework would have been difficult in a 3D framework since a circular hole would require very fine grid resolution which would be detrimental for the particle phase in terms of its stability. For a 2D setup with the depth of the bed being reduced to a single particle diameter, modeling circular holes is not possible. Instead the width of each jet in the 2D setup has been kept considerably close to the diameter of the holes from the experiments, resulting in a width of 2.015 mm for each jet. The corresponding hole

diameters for the distributor type A1 is 2 mm in the experiment. Rectangular slots having the same area as the circular holes have been modeled for the 3D setup. This ensures the same flow-rate through the distributor plate as in the experiment. The pitch of the jets has been kept equal to the experiments in both the cases. Since the cross-sectional area of the bed has been reduced in the 2D simulation, the jet velocities are lower in the computation than in the experiment. Figure 4.1 shows the distributor plate design for the experimental setup, 3D simulation and 2D simulation, respectively.

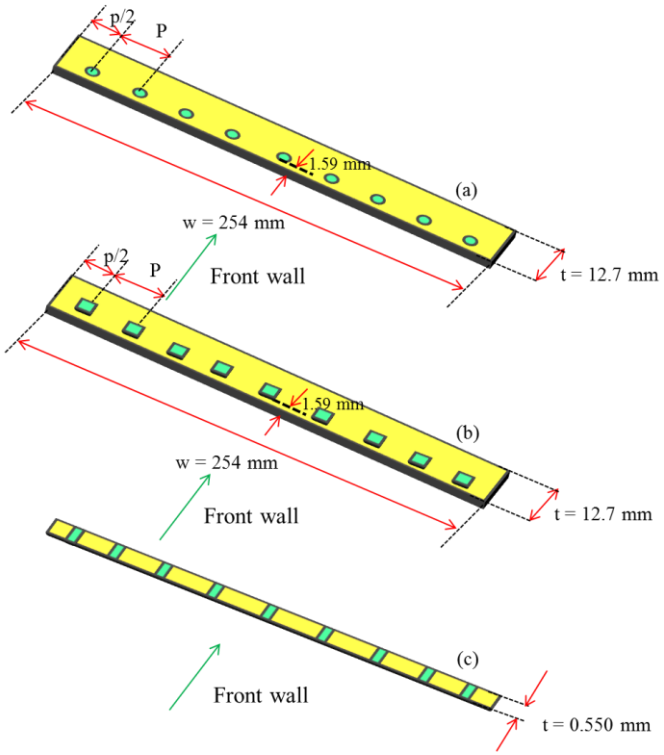

Figure 4.1: Jet configurations for (a) Experimental setup, (b) 3D Simulation and (c) 2D Simulation

Boundary Conditions

No slip boundary condition has been imposed on the fluid at the side walls. The bottom of the bed is the distributor with velocity inlet as the boundary condition. The top portion of the domain has been given a boundary condition of mass outlet. The front and the back portions of the bed are walls for the 3D setup and have periodic conditions instead of walls for the 2D setup.

Grid Size

The minimum grid size is restricted by the need to have more than 3 particles in each direction of a fluid cell (Muller et al., 2009) to satisfy the volume averaged momentum and continuity equations as derived by (Anderson and Jackson, 1967a). The other restriction on the grid size is the width of a single jet. In order to facilitate calculations, the grid size along the width of the bed has been kept close to the jet width. Uniform grid size has been used throughout. Table 4.2 lists the number of fluid cells used along each direction of the bed.

Table 4.2: Number of fluid cells

Case	Along width	Along height	Along depth
A1(2D)	126	248	1
A1(3D)	126	248	8

Particle Properties

Glass particles of 550 μm with a density of 2500 kg/m^3 have been used in the simulations. The minimum fluidization velocity of the particles is 0.22m/s. The superficial velocity used is 1.43 times that of the given minimum fluidization velocity in accordance with the experiment. The particles fall in Geldart group B classification. The initial bed height is close to 130 mm, which is similar to the experiment. Table 4.3 lists the above mentioned particle properties used.

Table 4.3: Particle Properties

Case	Diameter (mm)	Density (kg/m^3)	U_{mf} (m/s)	Number of particles
A1(2D)	0.550	2500	0.22	126864
A1(3D)	0.550	2500	0.22	2900016

DEM parameters for modeling collisions

The input parameters required for Discrete Element Method to model inter particle collisions are the spring constants in both normal and tangential directions, the

coefficient of restitution of the particles and the coefficient of friction between the particles. The spring constants are considered same in both the normal and tangential directions. Numerical simulations performed by (Muller et al., 2009) suggest that DEM simulations are more or less insensitive to the coefficient of restitution as well as the coefficient of friction as long as there exists some energy dissipating route for particle-particle and particle-wall collisions. So standard values used frequently in DEM literature have been considered in the computation. In our analysis, the motion of the particles are restricted to a 2D x-y plane for the 2D setup, as the bed is just one particle diameter deep in the z direction. For the 3D setup, no such restrictions apply to the motion of the particles. Table 4.4 enumerates the various DEM parameters used. The same property values have been used for particle-wall interactions.

Table 4.4: Parameters used in DEM

Case	Coeff. of Restitution (e)	Coeff. of Friction (μ)	Spring Constant (k_n, k_t)
A1(2D)	0.90	0.10	800 N/m
A1(3D)	0.90	0.10	800 N/m

Time step

The maximum time step is restricted by the need to resolve the particle collisions without causing instability in the calculations. The critical time step for inter particle collision is based on (Tsuji et al., 1993), given by

$$t_{cr} = \frac{\pi}{[\frac{k_n\left(1-\gamma^2\right)}{m_{eff}}]^{1/2}} \tag{4.1}$$

where γ denotes a constant given by

$$\gamma = \frac{-\ln(e)}{[\pi^2 + \{\ln(e)\}^2]^{1/2}} \tag{4.2}$$

and m_{eff} is the effective mass of the colliding pair. Based on the above formulations, the critical time step for collision is 3.23E-05 seconds. $1/10^{th}$ of this critical time step or 3.23E-06 seconds has been taken as the particle as well as the fluid time step. This extremely small time step makes the computations extremely time consuming. For the 2D case, a single simulation took around 45 days (1080 hours) to complete using 9 processors in a MPI framework. For the 3D case, a single simulation running using 18 processors in MPI framework took about 7 months of computational time. A significant amount of time goes in the detection, packing and un-packing of ghost or halo particles across processor boundaries required for neighbor list creation.

Results and Discussion

The simulation is run for a total of 8.38 seconds for the 2D setup. Time-averaged data is obtained during the last 3.38 seconds after the initial transients have passed. For the 3D setup, due to excessive computational time requirements, results were averaged only for 2.38 seconds after the initial 3 seconds of transients have passed. Figure 4.2, Figure 4.3 and Figure 4.4 show snapshots of the instantaneous bed profile from the experiment (Agarwal and Lattimer, 2011), the 2D simulation and the 3D simulation, respectively.

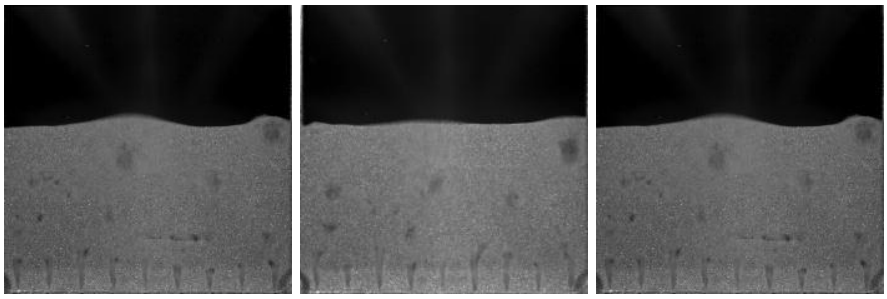

Figure 4.2: Instantaneous bed characteristics from experiment (Agarwal and Lattimer, 2011).

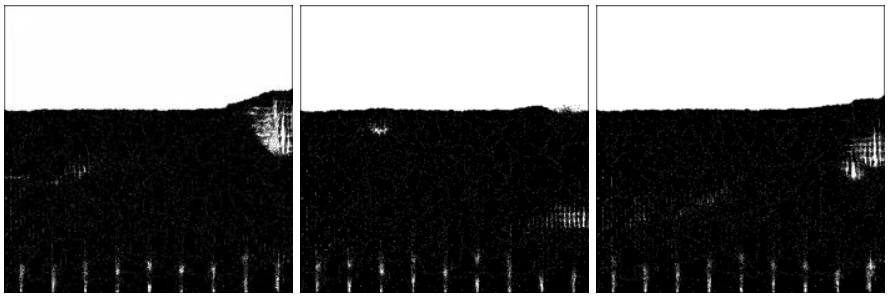

Figure 4.3: Instantaneous bed characteristics from 2D simulation

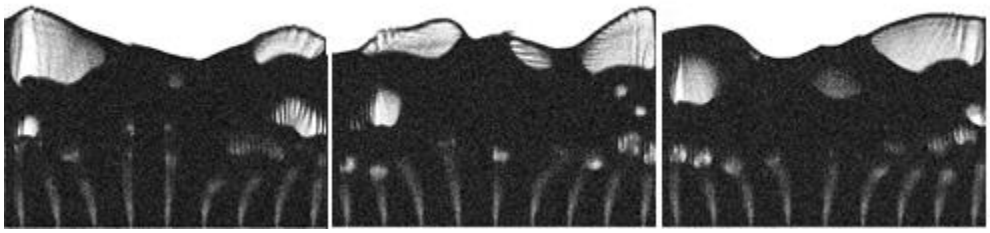

Figure 4.4: Instantaneous bed characteristics from 3D simulation

The discrete jets are clearly visible in both the experiment and the simulations together with bubbles that rise through the particle bed. The smaller number of bubbles in the bed in the 2D simulation is attributed to the smaller number of particles and the two-dimensionality of the bed. The tendency to form larger and more frequent bubbles increases with an increase in the number of particles in the bed as well as with the three dimensionality of the bed. This leads to more frequent bubble formation in the experimental bed and the 3D simulation, respectively, as is shown in Figure 4.2 and Figure 4.4. Both the experiment and the 2D simulation show that the jets do not merge but maintain their separate identities. A certain amount of jet interaction could be seen for the 3D simulation, especially near the walls where the bubbles form. In the 3D simulation, the jet penetration into the bed is greater compared to the experiment and the 2D simulation. Bubble eruption at the freeboard could be distinctively seen in the 3D simulation, which is less frequent in the 2D simulation. The typical particle raining effect (Rowe and Partridge, 1965) inside the bubbles could also be distinctively observed near the freeboard of the 3D simulation. Figure 4.5 shows the instantaneous iso-surface contour plot of void fraction in the bed for the 3D simulation. An iso-surface void

fraction value of 0.42 has been chosen for this plot, in order to accentuate the jets as well as the bubbles forming inside the bed.

The iso-surface plots show the grooves that are getting formed near the front wall due to the jets moving through the particles. A zoomed in view of the grooves essentially show a cylindrical contour, which gradually widens due to jet diffusion as the jets move up, away from the distributor plate. It is also evident from the iso-surface contour that change in properties along the depth (along z) in the bed is negligible, since the particles mostly move in the plane of the jets (along x-y plane). The main function of the depth is to provide room for the bubbles to form, coalesce and burst at the freeboard.

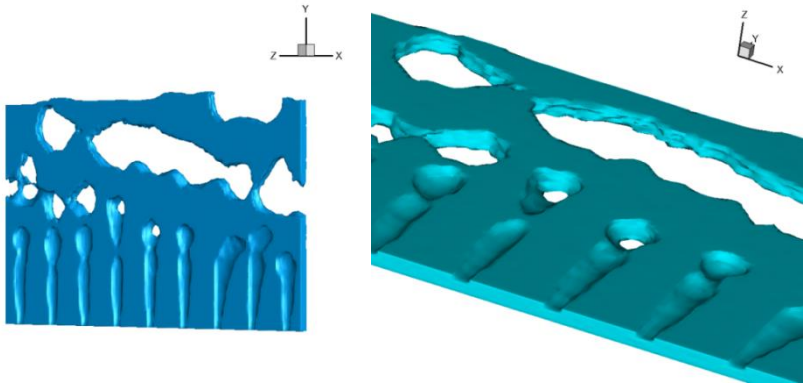

Figure 4.5: Instantaneous iso-surface contour of void fraction in 3D simulation

Solid Fraction Profiles

The time averaged solid fraction contour plot is shown in Figure 4.6. It clearly shows that the jets do not merge and remain separate for the 2D simulation and the experiment. The solid fraction in between the jets is that typical of compact packing at 0.62. The jet lengths are comparable between the experiment and the 2D simulation. No large bubbles are formed in the domain for the 2D simulation, whereas clear bubble formation could be seen near the walls for the 3D simulation as well as the experiment. This is confirmed from the instantaneous snapshots and the lower solid fractions near the walls compared to the center of the bed. The freeboard region near the fourth and the ninth jet in the 2D simulation shows lower solid fraction values compared to the rest of the bed signifying more frequent bubble eruptions at these locations. This is because the bubbles tend to move up and erupt at the free board more frequently at those two specific locations in the simulation. One of the contributing factors to this asymmetry in the bed

could be the overall short averaging time in the simulation and the small number of particles which would be more prone to larger instantaneous variations than a 3D bed with more particles. This is also evident from the symmetric patterns predicted by the 3D simulation.

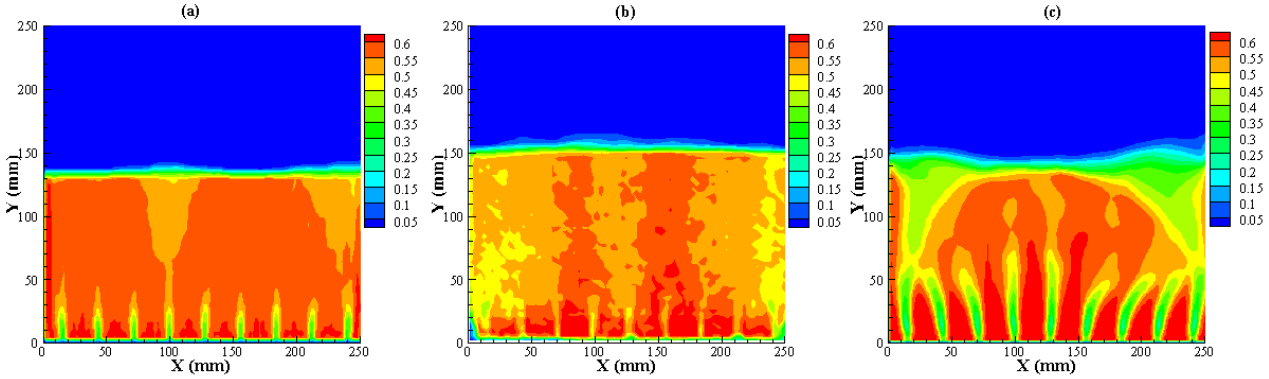

Figure 4.6: Solid fraction contour plot (a) 2D Simulation, (b) Experimental (Agarwal and Lattimer, 2011) and (c) 3D Simulation (The color range is from 0.05 to 0.65)

The solid fraction profiles across the cross section of the bed at different heights from the distributor plate are shown in Figure 4.7(a-c). Figure 4.7(a) compares the solid fraction at a height of 10 mm from the distributor plate. It can be seen that the values from the simulations match reasonably well with the experiment. With an increase in height from the plate, discrepancies in the solid fraction values start emerging near the walls for the 2D simulation. 2D DEM simulation over-predicts the amount of solid present near the walls. 3D simulation on the other hand predicts solid fraction values near the walls which agree well with the experimental values. In the experiment, bubbles tend to form near the walls and merge at the center of the bed near the free board. Similar bubble characteristics are observed in the 3D simulation but not in the 2D simulation due to a smaller number of particles. Also the frequency of bubble formation is much lower in the 2D simulation due to a smaller orifice velocity. This leads to higher solid concentrations along the walls. Given these discrepancies near the freeboard, the jet characteristics close to the distributor plate for the 2D simulation are in good comparison with the experiment whereas the 3D simulation near the distributor plate deviate from the experiment. A plausible reason might be not including any turbulence modeling for jet breakup near the distributor plate. But overall, a 2D simulation is capable of predicting jet

characteristics near the distributor plate whereas a 3D simulation captures the central bed and freeboard effects of bubble formation and eruption.

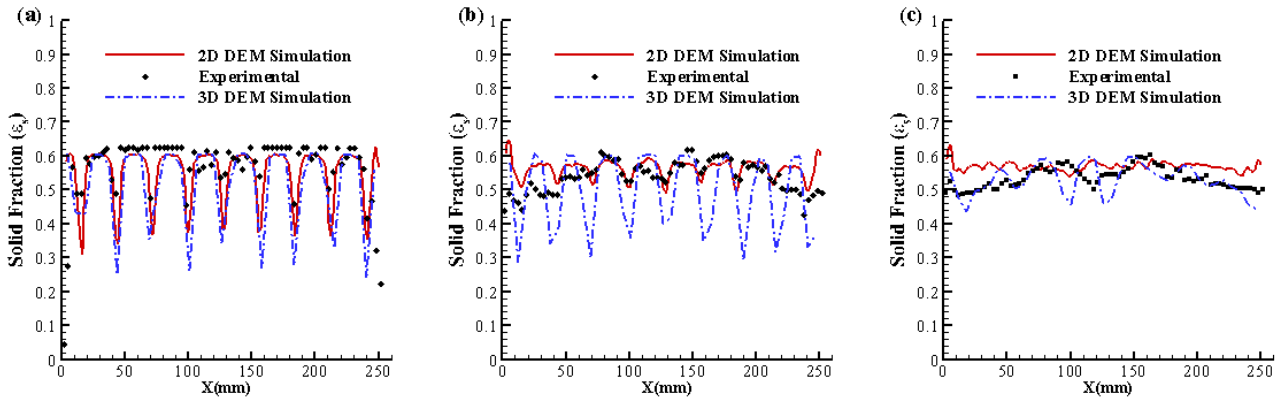

Figure 4.7: Solid fractions at a height of (a) 10 mm (b) 30 mm (c) 60 mm.

Particle Velocity Field

The particle velocity field in the simulations is based on the average velocity of the particles present inside a fluid cell.

$$\vec{V}_{av} = \sum_{N} \vec{V}_p \Big/ N \tag{4.3}$$

In the experiment, the particle velocity field is obtained by averaging over a PIV interrogation area. The number of particles present inside a fluid cell in the simulation is almost 27 and it is about 30 in the experimental PIV interrogation area. The experimental orifice velocity for the 9 jets case was 35.37 m/s. Due to the reduction in the depth of the domain from 12.7 mm to 0.550 mm in the 2D simulation, the simulated orifice velocity through each jet was 4.37 m/s to maintain the same superficial velocity of 0.315 m/s as in the experiments. Due to the lowering of the inlet velocity, the particle velocities are lower in the 2D simulation compared to the experiment. So, in order to compare velocities between the experiment and simulations, all velocities are normalized by the orifice or inlet velocity. Figure 4.8(a) and (c) show the contour plots of normalized absolute magnitude of particle velocity obtained from the 2D and the 3D simulations, respectively. Figure 4.8(b) shows the velocity magnitude profile from the experiment. It is seen that

the experimental jet velocities are much lower than in the simulations. This is because the PIV, which was used for velocity measurement in the experiment, favored the slow moving particles entraining in the vicinity of the jet and could not capture the high velocities at the center.

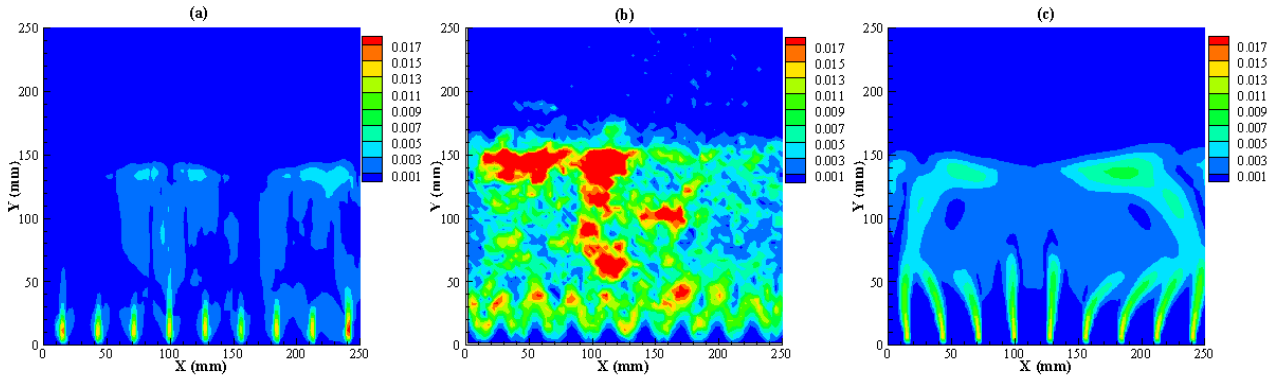

Figure 4.8: Normalized particle velocity magnitude contours from (a) 2D simulation (b) Experimental (Agarwal and Lattimer, 2011) and (c) 3D Simulation (The color range is from 0.001 to 0.0018)

However, the particle velocities at the periphery of the jet are well resolved in the experiment. Comparing Figure 4.8(a) and (b), it can be seen that the normalized particle velocities are comparable in and around the jetting zone. In the 2D simulation, lower normalized particle velocities are seen in the freeboard region compared to the experimental result and could be the direct consequence of the two-dimensional simulations. On the other hand, Figure 4.8(c) shows higher velocity near the freeboard region. It also clearly shows the path taken by the bubbles. They start forming due to jets merging near the walls, start moving up the bed along the walls and finally erupt at the freeboard. The bubbles do not grow in size in the 2D simulation; rather they are small and dispersed throughout the bed. This prevents the particles from reaching high velocities at the freeboard in the 2D simulation. But the velocity values close to the jets in the grid zone region match fairly well with the experiments. In industrial applications using jetting fluidized beds, the zone containing the jets is important as most of the heat and mass transfer occurs in this zone. Figure 4.9 shows the comparison of normalized particle velocity magnitudes between the experiment and the simulations at different heights. The velocity comparison with experiment is reasonable along the jet boundaries for the 2D simulation. The region around the jets is important as it is the region of particle entrainment. Figure 4.9 shows that the 2D DEM simulation is able to capture the jet

velocities fairly well closer to the distributor plate as compared to farther away from it. This is because near the jets, there are very few 3D structures. The 3D simulation, on the other hand predicts better normalized velocity values higher up the bed. The velocity prediction close to the walls in the 3D simulation compares well with the experiment even at higher height from the distributor plate. For the height of 60 mm, there is a sudden jump in the velocity at the center of the bed in the experiment, which is not captured in the 3D simulation. An accurate reasoning for this is difficult to provide, but it might be due to more energetic bubble eruptions at the freeboard in the experiment near the center of the bed as compared to the 3D simulation.

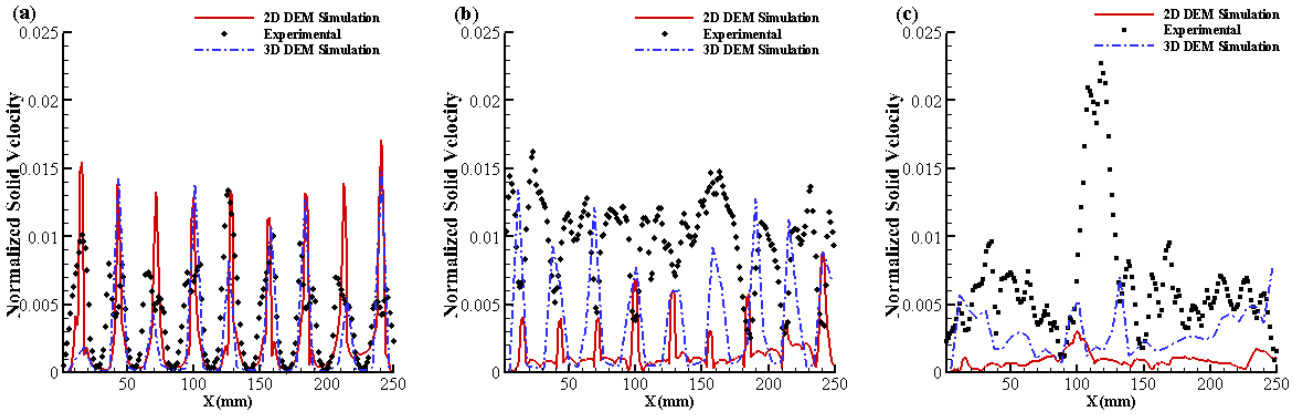

Figure 4.9: Normalized particle velocities at a height of (a) 10 mm, (b) 30 mm and (c) 60 mm.

As the bubbles rise up in the bed, they begin to grow in size and extend to more than one particle diameter along the depth of the bed. This expansion of bubbles along the depth is not getting captured in the 2D DEM simulation. The velocity magnitude in the experiment starts deviating from the 2D simulation at heights greater than the jet height.

Particle Flux

Figure 4.10 compares the normalized horizontal particle flux at different heights from the distributor plate for the experiment and the simulations. The particle flux entraining along the jets is calculated based on the following formulation:

$$\dot{m}_p = \varepsilon_s \times U_s^* \tag{4.4}$$

where U_s^* is the normalized horizontal solids velocity across the jets.

The horizontal particle flux is an indication of particle entrainment along the jets. In the experiment, the jets are almost cylindrical and the particle entrainment is effectively three dimensional. Unlike the experiment (Agarwal et al., 2011a), the particle entrainment in the 2D simulation is essentially two dimensional and thus the magnitude of horizontal fluxes is lower in the 2D simulation compared to the experiment. The overall trends predicted by the 3D simulation match fairly well with the experiment, especially at higher heights from the distributor plate. The horizontal particle velocity at the jet centers is almost zero as particles move into the jets horizontally and move up vertically at the center of the jets. This circulation pattern gives rise to enhanced fluid-solid mixing close to the distributor plate. Compared to the 2D simulation, the 3D simulation predicts a better particle flux higher up the bed than near the distributor plate. Close to the distributor plate, the horizontal particle flux predicted by the 3D simulation is lower than that predicted by the 2D simulation. The reason for this might be the existence of larger dead zones between the jets in the 3D simulation as is evidenced in Figure 4.8.

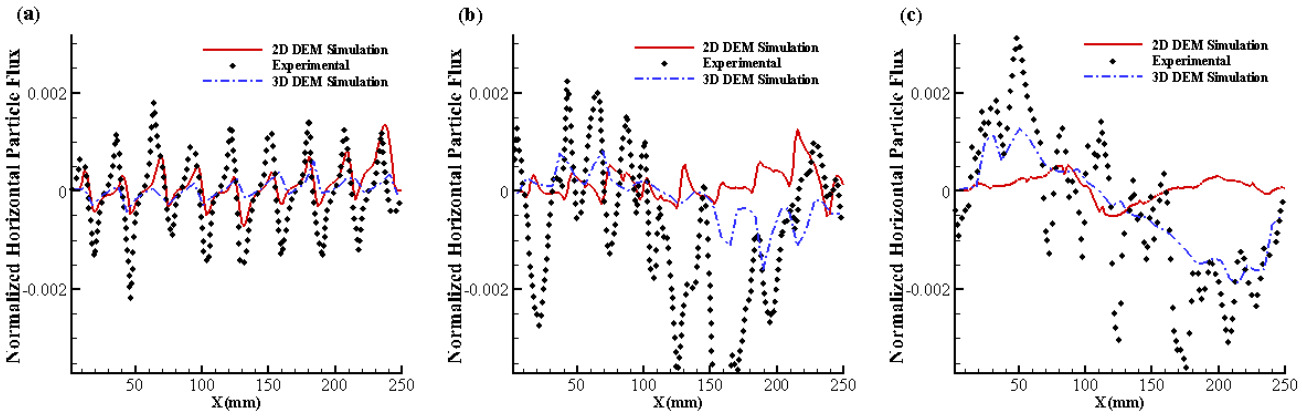

Figure 4.10: Normalized horizontal particle flux at a height of (a) 10mm, (b) 30 mm and (c) 60 mm.

Bed Expansion

The bed expansion is calculated based on the variation of average solid fraction value across the bed cross sectional area with height. The average solid fraction initially increases with height due to the upward movement of solids close to the jets. Then there is the region of bubbles, where the average solid fraction remains almost constant and

finally at the freeboard the bubbles burst and the particles flow downwards thus decreasing the solid fraction at that height. Figure 4.11 shows the comparison of bed expansion between the experiment and the computations.

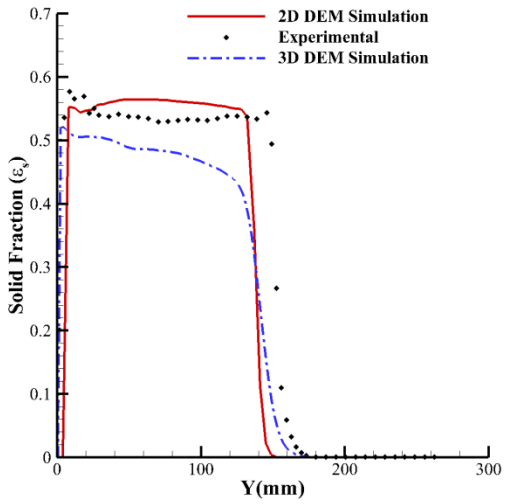

Figure 4.11: Comparison of average solid fraction along height.

The variation of average solid fraction across the bed with height in both the 2D and the 3D simulations follow similar trend as in the experiment. It is observed in Figure 4.11 that the maximum solid fraction in the 3D simulation is low compared to the 2D simulation and the experiment. The initial bed in the simulations is setup to match the starting height of the bed in the experiment. This results in the total particle mass in the 3D simulation to be 631.58 grams and the 2D simulation to be 27.63 grams, respectively. The total mass of the particles used in the experiment for the same initial bed height is 667.40 grams. The difference in mass occurs due to the particles in the experiment being not exactly spherical, which leads to higher particle mass at the same starting height. Based on the mass of particles and the obtained expanded height, the bulk solid fraction, calculated using Eq. (4.5), is found to be 0.452 for the 3D simulation, 0.476 for the experiment and 0.527 for the 2D simulation, respectively. Due to a lower bulk solid fraction obtained for the 3D simulation, a lower maximum solid fraction value is seen in Figure 4.11 for the 3D simulation compared to the 2D simulation and the experiment.

$$\varepsilon_{s,bulk} = \frac{M_p}{\rho_p \times A_c \times h_{\exp}} \tag{4.5}$$

where M_p, A_c, $h_{\exp}$ represent the total mass of the particles inside the bed, the total cross-sectional area of the distributor plate and the expanded bed height, respectively.

Due to a lower freeboard particle velocity, the actual bed expansion is lower in the 2D simulation compared to the experiment. Figure 4.12 shows a zoomed in view of the expanded bed height. It is clear from Figure 4.12 that the bed height after expansion is close to 150 mm in the 2D simulation whereas it is close to 174 mm in the experiment (~13% difference). On the contrary, the expanded bed height is predicted very well in the 3D simulation. The 3D simulation predicts an expanded bed height of 173 mm (<1% difference).

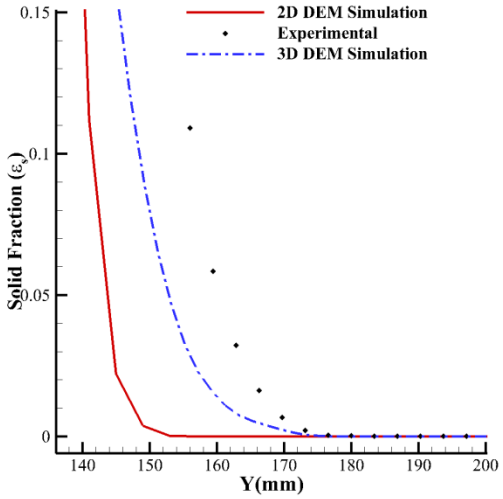

Figure 4.12: Zoomed in view of expanded bed height

Jet Height

Various researchers have used different ways of calculating the jet height. One of the established definitions of jet height is the height at which the initial bubble detaches from the jet (Merry, 1975; Müller et al., 2009; Rees et al., 2006; Wen et al., 1982). The maximum length from the highest point in the jet to the bed bottom has been used as the jet height by (Hong et al., 2003). Concept of momentum dissipation location has been

used by (Raghunathan et al., 1988) as their definition for jet penetration height. In the experiment (Agarwal et al., 2011b) the jet entrainment angles were used for detecting the location of jet penetration length which proved to be an extension of the first method. In our computational analysis, the first definition of initial bubble detachment from the jet has been used as the jet height. The average of the jet heights of the 9 jets comes to 22.1 mm in the 2D simulation. Figure 4.2 shows the extent of the jet penetration. The experimental value for the jet penetration height comes close to 21.32 mm with an uncertainty of +/- 1.70 mm for an orifice velocity of 35.37 m/s. The jet height predicted in the 3D simulation differs significantly from the 2D simulation and the experiment. The average jet height is about 43 mm in the 3D simulation. This discrepancy arises because the jets in the 3D simulation do not break and interact with each other at lower heights. This might be a direct consequence of non-inclusion of turbulence models in the analysis.

Summary and Conclusions

Two and three dimensional simulations of a jetting fluidized bed have been performed using the Discrete Element Method. Various bed characteristics have been compared with experiment. The 2D results compare relatively well with the experiments close to the distributor plate which is essentially the jetting zone. The solid fraction profiles match closely with experiment at a height of 10 mm from the distributor plate. The normalized velocity magnitudes are higher at the freeboard in the experiment compared to the 2D simulation while showing similar trends near the jets. The average bed expansion in the 2D simulation is smaller than that of the experiment due to the effects of lower orifice velocity. Higher up in the bed, the discrepancies between the 2D computational and experimental values increase. This is due to the 2D nature of the simulation which is not capable of capturing the three dimensional structures near the freeboard. The simulation results help us to understand the trends in solid fraction, particle velocities and solid fluxes near the jetting zone of an actual jetting fluidized bed.

A full scale 3D simulation of the experimental setup having close to 3 million particles has been conducted to bring out the differences and the similarities with the 2D modeling of the jets. Instantaneous plots of 3D solid fraction profile have been shown in order to get an overall trend of the jetting fluidization process. The time averaged solid

fraction profiles match well with the experiment. The normalized particle velocities are predicted fairly well in the 3D simulation, especially at higher heights from the distributor plate. The 2D simulation performed could not predict high particle velocities near the freeboard of the bed. The normalized horizontal particle fluxes far away from the distributor plate are predicted fairly well in the 3D simulation. The expanded bed height predicted by the 3D simulation matches closely with the experiment. These results show that a full scale 3D simulation is able to capture the essential characteristics of jetting fluidized beds far away from the distributor plate. Surprisingly, closer to the distributor plate, the results predicted by the 2D simulation match well with the experiment compared to the 3D simulation. This shows that the jetting region close to the distributor plate is essentially 2D in nature which can be modeled using 2D simulations with a fair amount of accuracy. On the other hand, a detailed 3D simulation is needed to capture the complex bubble dynamics occurring near the freeboard of the bed. Given the discrepancies near the freeboard region arising out of the assumptions in a 2D model, the fundamental particle-jet interactions near the distributor plate could be captured and analyzed with considerable accuracy and in much lesser time in a 2D simulation compared to a computationally expensive 3D simulation.

Performing a full scale 3D simulation with close to 3 million particles is excessively time consuming and difficult at the same time. An effort has been made in this present work to bring out the similarities and the differences between the 2D and 3D modeling of jetting fluidized beds with multiple jets. A 3D simulation for multiple jets with such a large number of particles has not been attempted previously in literature. Improvements in the 3D model can be suitably done in future work to establish the effects of model parameters in predicting the results.

Chapter 5 A Novel Two Grid Formulation for Fluid-Particle Systems using the Discrete Element Method

Introduction

Recent advances in computational power enable us to perform high fidelity numerical simulations on granular flows. Discrete Element Modeling (DEM) and Two-Fluid-Model (TFM) are the two most widely used numerical methodologies for modeling granular flows like fluidized beds and spouted beds. The two methods differ fundamentally in the approach they follow. DEM is an Eulerian-Lagrangian approach where the fluid flow is solved in an Eulerian framework while tracking each individual particle in a Lagrangian fashion. On the other hand, TFM considers the gas and solid to be two interpenetrating media and solves for their interaction in an Eulerian-Eulerian approach. DEM provides higher resolution compared to TFM as it resolves the complete dynamics of each particle in the flow. Additional closure equations are required in TFM to account for the continuum description of particles. No such closure laws are required in DEM as it treats the particles individually. DEM was first developed by (Cundall and Strack, 1979) and later adopted for simulation of fluidized beds and coupled with CFD by (Tsuji et al., 1993). Since then, DEM has been used in investigating a wide variety of applications including surface diffusion problems (Kuwagi et al., 2000; Limtrakul et al., 2004), modeling behavior of cohesive particles (Iwadate and Horio, 1998; Mikami et al., 1998), segregation of binary particle mixtures (Feng et al., 2004; Feng and Yu, 2010), capturing bubble dynamics in fluidized beds (Kobayashi et al., 2000; Pain et al., 2002; Rong et al., 1999) and so on. A comprehensive review focusing on the research work done using DEM has been given by (Deen et al., 2007; Zhou et al., 2010; Zhu et al., 2008). Two broad categories of Discrete Particle Methods (DPM) are available for modeling fluid-particle interactions namely resolved and unresolved, respectively. A resolved discrete particle model (RDPM) is much like a direct numerical simulation (DNS), where fluid boundary conditions are prescribed on the boundary of each individual particle. Arbitrary Lagrangian Eulerian (ALE) and Immersed Boundary Method (IBM) are two of the most popular techniques used to specify the no-slip

boundary conditions on the particle surface for RDPM. RDPM is generally used to model flows at very small scales, without the requirement of fluid drag closures on the particle surface. The unresolved DPM (UDPM) on the other hand does not require fluid boundary conditions to be specified on the particle surface as they use drag closure equations. UDPM's have become popular due to their ability to predict fluid-particle interactions with considerable accuracy without the need to have sophisticated grid resolution techniques near particle surfaces. A detailed review on the different numerical techniques adapted to model gas-solid flows at different scales has been given by (van der Hoef et al., 2008).

Till now mostly a single-grid approach has been used for DEM-CFD calculations, i.e, the particle and fluid calculations are done on the same grid. This has an inherent problem in that the resolution requirements for the particle and fluid fields are contradictory to each other. Generally, fine grids are required to resolve the fluid flow field. Fine grids for flow resolution become particularly important to resolve small geometrical features which influence the flow, when the interstitial flow is turbulent, and when velocity and temperature gradients need to be resolved at surfaces for calculating wall shear stresses and heat transfer coefficients. The fine fluid grids however, conflict with particle field resolution requirements which require that the grid size should be large enough to represent the local volume fraction of the particulate phase properly (Anderson and Jackson, 1967a). Too few particles in a cell result in sharp changes of the solid fraction field across cells whenever particles cross cell boundaries. This can lead to large spatial and temporal fluctuations in the fluid volume fraction across cells ultimately making the numerical integration unstable.

This aspect has been worked on in the literature by (Link et al., 2005; Link et al., 2008) who performed a combined experimental and computational study to find flow regimes in a spouted fluidized bed using a DEM-CFD methodology. In their method performed on a single grid finer than the particle diameter, they have represented each individual particle within a porous cube halo of predetermined size which moves with the particle. The solid fraction representing the particle is spread over the porous cube and then distributed over the finer fluid cells in a volume weighted manner. This is done for all particles. In doing so, they prevent numerical instabilities arising due to the presence

of finer fluid cells in comparison to particle size by smoothing out the variation in solid fraction. The porous cube halos can intercept a fluid cell in any possible fashion which requires a calculation of the fraction of the finer cells being intercepted by the porous cube. For a 3D simulation having millions of particles, the calculation of this cell fraction at every time step can be computationally expensive. The other difficulty arising out of the porous cube method is the communication overhead across inter block/inter processor boundaries, needed for parallelization, where information regarding these fraction of cells intercepted need to be communicated between processors. Depending on the position of a particle near an inter processor boundary, varying volumes of the porous cube could be present on a neighboring processor. This scenario would necessitate determining the number of cells influenced by the porous cube on the adjoining processor for each particle in the vicinity of the boundary, followed by packing and communication. This can cause inefficient parallelization and thus severely limit the parallel scalability.

In this work, we have developed a two-grid formulation for systems involving DEM-CFD coupling in a parallel processing framework. In this formulation, the fluid flow equations are solved on a fine grid which is independent of the particle size, whereas the discrete particle equations are solved on a coarser grid in which each coarse particle cell is composed of multiple fluid cells. Recently, a similar technique has been used by (Farzaneh et al., 2011) to conduct 2D Lagrangian modeling of fuel mixing in fluidized beds. The approach that they have used is similar to what we independently propose in our present work. One important difference lies in the way the void fractions are calculated in each of the fluid cells. In their work, the exact void fractions are calculated based on the volume of particles intercepted at each fluid cell. This is time consuming, and extremely complicated for a three-dimensional fluid-particle coupled problem involving thousands of particles. To avoid this, we calculate the void fractions at the particle cell and map the same value back to each of the fluid cells that fall within that particular particle cell. This present approach might result in small inaccuracies, but for a domain having tens of thousands of particles; the inaccuracies would be negligible compared to the ease and swiftness of the simulations.

The new scheme is tested in a jetting fluidized bed and the results have been validated with experiments (Brown and Lattimer, Unpublished results) performed on the

same geometry. Relatively large, 750 μm particles have been used for the tests. Single, double and triple jet configurations have been studied using the new two-grid formulation. Each jet is of size 1.6×4.95 mm^2. Using a single grid is not possible for the large particle size of 750 μm as the requirement of having 3-4 particles in each direction of a fluid cell (Muller et al., 2009) is not satisfied. In the single grid formulation, the grid size at the jet entrance plane should be equal to the jets or smaller than it. But in the case of 750 μm particles and 1.6 mm jet width, even the largest possible grid size using a single grid cannot satisfy the discrete phase requirement of having a smooth void fraction. The two-grid formulation overcomes this limitation by allowing the jets to be resolved on the fluid grid as well as satisfying the requirements of a smooth void fraction on the particle grid. The method proposed in this chapter avoids the complications of the porous cube method by considering two separate fixed grid definitions, which intercept each other in a regular pattern thus facilitating inter-processor communications. The calculation overhead of calculating a very high number of cell fractions is also not required in this method thus aiding in simpler and faster calculations, needed for a large number of particles in three-dimensions. The chapter is structured as follows. The next section describes the methodology used in the single-grid and two-grid DEM followed by a section on results and discussion, and the conclusions.

Two-grid formulation

In this method, two separate grids are considered, a fine grid for the fluid calculation, and a coarse grid consisting of multiple fluid grid cells for the particles as shown in Figure 1. The fluid fields (velocity and temperature) are calculated on the fine grid and mapped to the particle grid for interphase momentum and energy exchange. The solid fraction, momentum and energy interphase exchange terms are calculated on the particle grid and mapped back to the fluid grid.

As shown in Figure 5.1, the particle cells are coarse enough to have sufficient particles inside them to represent the local averaged solid fraction properly.

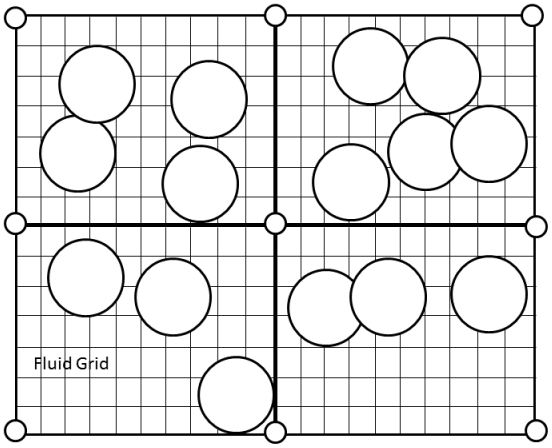

Figure 5.1: Particles inside coarse particle cells with several finer fluid cells

In our present work, the length of the particle cell is kept to 3 times the particle diameter in each direction according to (Muller et al., 2009). This allows for sufficient number of particles in each particle cell.

Fluid-Particle coupling algorithm

At the start of a time step, first the fluid velocity field is advanced in time using a fractional-step method with void fractions and interphase exchange terms calculated at the new particle locations from the previous time step. The discrete phase calculation is then invoked using the following steps:

1. Locate particles with known (x,y,z) coordinates by assigning them (i,j,k) values on the background particle grid. During this step particles which have travelled to another processor and cannot be found are packed and sent to the appropriate neighboring processor where they reside.
2. Fluid velocity and temperature are interpolated from the fluid grid to particle locations for calculation of interphase momentum and energy transfer.
3. Particles which lie in boundary cells on processors are exchanged between adjoining processors to construct a list of ghost particles on each processor. The ghost particles are used to construct the neighbor list for collision force calculation on each processor.

4. The neighbor list of colliding particles is constructed by binning the particles in individual particle cells and then cycling through all particles in neighboring cells to identify overlapping or colliding particles.
5. Particle-particle collision forces and particle-wall collision forces are calculated based on the soft sphere model.
6. Other forces characterizing interphase drag and energy transfer and gravitational forces are calculated.
7. Interphase momentum and energy terms are transferred to the fluid grid for inclusion in the fluid momentum and energy equations.
8. Void fractions are calculated on the particle grid and transferred to the fluid grid for inclusion in the fluid momentum and energy equations.
9. Particle acceleration is calculated and new particle (x,y,z) locations are calculated.

Fluid-particle grid mapping

The fluid velocities calculated on the fluid grid are averaged over all the fluid cells in a particle cell and put at the center of the particle cell following step 2 from previous section. All the particles contained inside a particle cell experience the same fluid velocity.

Once the fluid velocity is obtained for a particle cell, drag forces are calculated on each individual particle following step 6 from previous section. The drag forces acting on all the particles in a particle cell are summed up and based on Newton's 3rd Law, the net drag force is redistributed back to the fluid cells contained within that particle cell following step 8 from previous section. The redistribution is done by volume weighting of the fluid cells as shown.

$$\vec{f}_{Drag} = -(\sum_{N} \vec{F}_{p,Drag}) \times \frac{V_{fg}}{V_{pg}} \tag{5.1}$$

where $\vec{F}_{p,Drag}, V_{pg}$ represent drag force on a particle, and volume of a particle cell, respectively.

The solid volume fractions are calculated on the particle grid as follows:

$$\varepsilon_s = \sum_N V_p \Big/ V_{pg} \tag{5.2}$$

where ε_s, N, V_p are the solid fraction, number of particles in any particle cell, and the volume of a particle, respectively. Once the solid fraction in a particle cell is calculated, the fluid volume fraction in the particle cell is straightforward to calculate as shown below.

$$\varepsilon = 1 - \varepsilon_s \tag{5.3}$$

Following step 9 from previous section, the fluid volume fractions are mapped back to the fluid cells contained inside a particle cell. The mapping scheme for the fluid volume fractions from the particle to fluid grids inside can be given as

$$\varepsilon_{fluid\_cell} = M_{p \to f}\{\varepsilon\} \tag{5.4}$$

where $\varepsilon_{fluid\_cell}, M_{p \to f}\{\}$ represent the fluid volume fractions in the fluid cells, and the mapping function or distribution function from particle to fluid grid. In our analysis, the mapping function maps the same value of ε to all the fluid cells inside a particular particle cell, thus giving

$$\varepsilon_{fluid\_cell} = \varepsilon \tag{5.5}$$

This completes the coupling between the coarse particle and fine fluid grids. Figure 5.2 shows the complete methodology involved in the two-grid framework. $\vec{u}_{pg}, N_{fg}$ represent fluid velocity in a particle cell (averaged from velocities in fluid cells contained inside a particle cell) and number of fluid cells inside a particle cell, respectively.

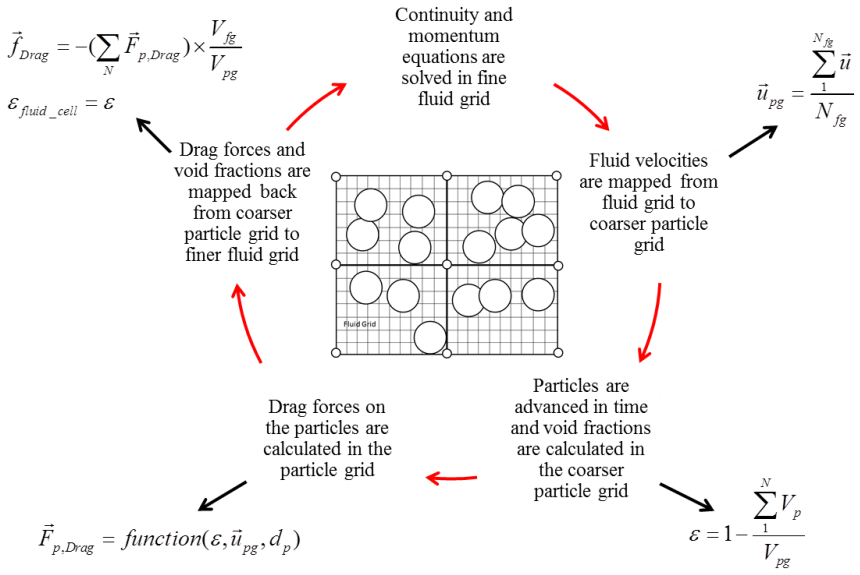

Figure 5.2: Flow diagram of fluid-particle grid mapping in two-grid framework

Computational Details

Figure 5.3 shows the bed geometry with dimensions $56.4mm \times 280mm \times 4.95mm$ in the x, y and z-directions, respectively. The two-dimensional jets (slits) are 1.6 mm wide and extend through the depth of the bed.

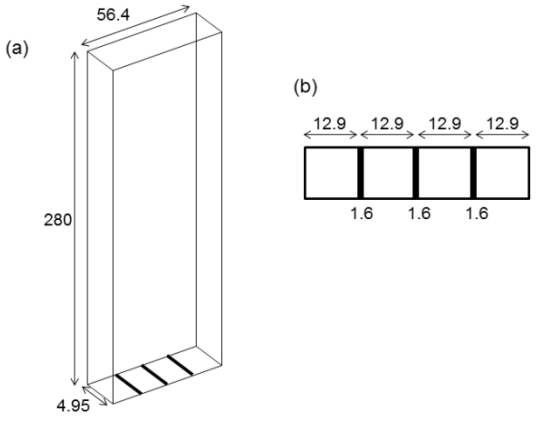

Figure 5.3: (a) Dimensions of the jetting fluidized bed (in mm), (b) Slit distribution on distributor plate

Details of jets

The slits are placed at a pitch of 12.9 mm from each other and from the side walls in the experiments and simulations. Superficial velocities of 1.6 and 3 times the minimum fluidization velocity have been used for comparison with experiments. The minimum fluidization velocity is calculated based on Kozeny-Carman equation as follows

$$U_{mf} = \frac{(\rho_p - \rho_g) g d_p^2}{150 \mu_g} \frac{\varepsilon^3}{1-\varepsilon} \tag{5.1}$$

Table 5.1 below describes the various cases run.

Table 5.1: Details of jet running conditions

Particle Diameter (μm)	No. of Jets	Superficial Velocity (m/s)	Jet Velocity (m/s)
750	1	0.688 (1.60 U_{mf})	24.47
750	1	1.294 (3.01 U_{mf})	45.30
750	1	1.294 (3.01 U_{mf}) [With high wall friction]	45.30
750	2	1.294 (3.01 U_{mf})	22.65
750	3	1.294 (3.01 U_{mf})	15.10

Boundary conditions

No slip condition for the fluid phase has been imposed on all the walls of the bed. The jet velocity is set to the value given in Table 5.1 as inlet boundary condition. A mass conserving uniform velocity profile is applied at the top outlet.

Grid Details

The actual physical grid is that of the fluid, where the Navier-Stokes equations are solved. The particle grid is virtual which is created within the code and mapped to the physical fluid grid. Each particle cell is a cube with $3 \times d_p$ as the length. In the present case, the length of each side of a particle cell is 2.25 mm for 750 μm particles. The physical grid is made finer with $175 \times 200 \times 5$ cells across the entire domain of the bed. This makes each fluid cell of size $0.322mm \times 1.40mm \times 0.99mm$. A single particle cell contains close to 25 fluid cells, based on their volumes. The finer fluid cells aid in

resolving the jets properly which would not have been possible with a single grid formulation.

Particle properties

Glass particles of 750 μm diameter with a density of 2500 kg/m^3 have been used in the simulations and the experiments. The particles fall in Geldart group D classification. The initial bed height is close to 60 mm and the number of particles is about 50,000 in both the experiments and the simulations. Table 5.2 lists the above mentioned particle properties.

Table 5.2: Particle properties

Diameter (μm)	Density (kg/m^3)	U_{mf} (m/s)	Number of particles
0.750	2500	0.43	50,000

DEM parameters for modeling collisions

The input parameters required for DEM to model inter particle collisions are the coefficient of restitution of particles during collision, the spring constants in both normal and tangential directions and the coefficient of friction between particles. The spring constants are considered to be the same in both normal and tangential directions. Standard values of coefficient of restitution and spring constants have been used in the present analysis. The same property values have been used for particle-wall interactions. Table 5.3 lists the parameters used for DEM.

Table 5.3: Parameters used in DEM

Coefficient of restitution (e)	Coefficient of friction (μ)	Spring constant (k_n, k_t)
0.90	0.10, 0.50	800 N/m

Time step used

The maximum time step that can be used is restricted by the time scale of particle collisions. The critical time step for inter particle collision is based on (Tsuji et al., 1993) as follows

$$t_{cr} = \frac{\pi}{[k_n(1-\gamma^2)/m_{eff}]^{1/2}} \tag{5.2}$$

where γ denotes a constant given by

$$\gamma = \frac{-\ln(e)}{[\pi^2 + \{\ln(e)\}^2]^{1/2}} \tag{5.3}$$

m_{eff} is the effective mass or reduced mass of the colliding particle pair. Based on the above formulations, the critical time step comes out to be 5.838E-05 seconds for 750 μm particles. The time step used in the simulations is 1/10th of this critical value. The fluid and the particle time steps are kept the same.

.

Results and Discussion

Two different superficial velocities have been tested with single, double and triple jet configurations. The calculations are allowed to reach a steady state till 5 seconds, after which time-averaged results are calculated for an additional 3 seconds. Time-averaged void fraction distribution and solids-velocity are compared to experimental measurements (Brown and Lattimer, Unpublished results). Particle Image Velocimetry (PIV) and Digital Image Analysis (DIA) were used as noninvasive experimental techniques to measure particle velocities and bed solid fractions, respectively. PIV bases its computation on statistically averaged displacement of a cluster of particles present in a predefined interrogation area. DEM on the other hand tracks each individual particle and so the resolution of particle velocities calculated by DEM is higher than that of PIV. This can lead to discrepancies between the computational and experimental particle velocities. The velocity vectors in the jet regions were masked in the experiments as the PIV resolution (time delay of CCD cameras) was not sufficient to capture the high particle velocities inside the jets. Uncertainty is present in the detection of particle displacement in PIV measurements. Digital Image Analysis (DIA) was used to convert the pixels obtained from PIV into intensity matrices. The final intensity matrices obtained from DIA were then used to calculate solid fraction values in the bed. The particles near the front wall are captured as high intensities. The particles behind them have progressively lower intensities. Various correlation functions have been used in literature (Brown, 2012) to

obtain solid volume fractions from intensity matrices. Uncertainty in the experimentally calculated solid volume fractions are introduced through these correlation functions.

Single Jet

Figure 5.4 shows the time-averaged void fraction contours for the case with a single jet and 1.6 times the minimum fluidization velocity. The general features of the bed are in good agreement between the experiments and computations. The central spout is more dispersed in the computations, which also over predicts the bed height. This might be due to particles experiencing higher drag near the center of the freeboard as compared to the experiment.

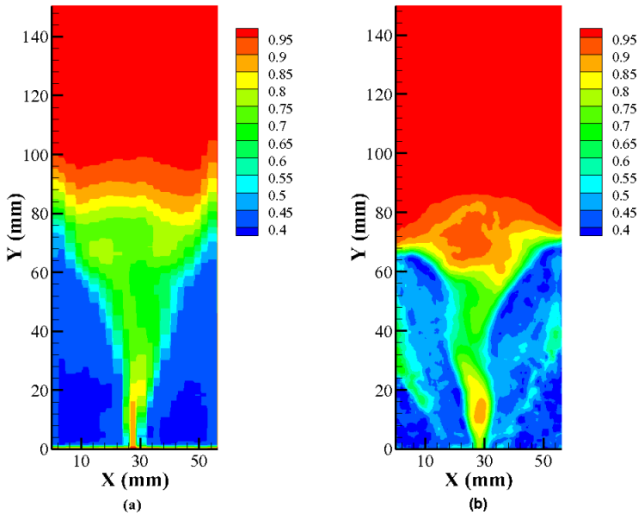

Figure 5.4: Void fraction contour plots for single jet and 1.6U_{mf} (a) DEM Simulation, (b) Experimental

Figure 5.5 shows the particle (solid) velocity vectors. The solid velocity vectors indicate the particle recirculation zones and their movement patterns in the entire domain. Distinct recirculation patterns can be seen in the computational result, which suggests strong particle mixing along the jet near the freeboard. The particles at the center of the jet possess higher momentum which forces them up along the bed, which after losing the momentum fall back into the bed. No such distinctive recirculating patterns can be observed in the experimental result. The experimental results suggest that the particles are pushed further up by the jet into the freeboard where they change direction and collapse back into the bed with a high downward velocity.

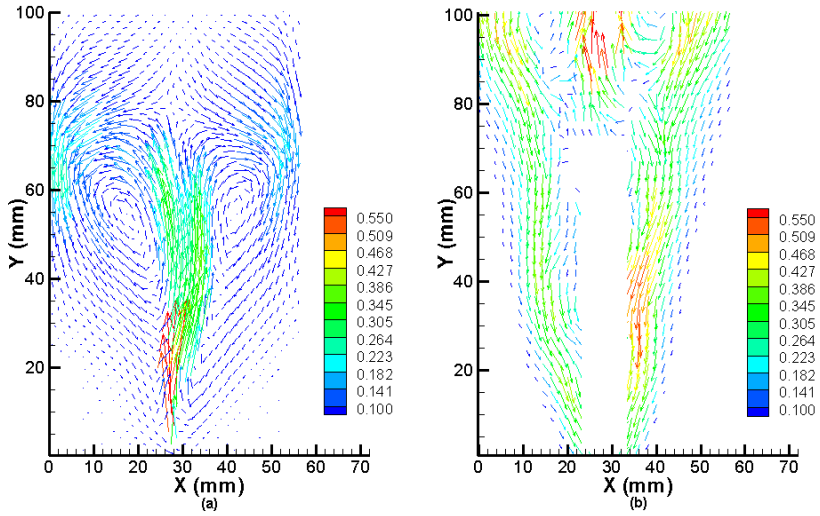

Figure 5.5: Particle velocity vectors for single jet and 1.6U_{mf} (a) DEM Simulation, (b) Experimental (Vectors are colored by velocity magnitude in m/s)

It is noted that the existence of particles between 80-100 mm in the experiments as indicated in Figure 5.5 is somewhat inconsistent with the void fraction distribution in Figure 5.4, which possibly could be attributed to the difficulty in accurately measuring the solid velocity in the bed. Another difference between experiments and computations is the existence of much larger dead zones near walls in the experiments, which could have contributed to the absence of recirculating zones in the bed by reducing the mobility of particles near the wall. The larger dead zones in the experiment indicate that a significant amount of particles near the walls experience larger frictional resistance to movement. In the experimental set-up, the side walls were painted with black paint for subsequent heat transfer analysis. It is hypothesized that the presence of the paint increased the coefficient of friction between the particles and the walls. To test this hypothesis, an additional simulation using a higher coefficient of friction was performed. The higher wall friction led to the formation of larger dead zones in the simulation but failed to eliminate the recirculating regions (see Figure 5.11 for 3U_{mf}).

As the jet velocity increases to 3 times the minimum fluidization velocity, a fountain like structure appears in the freeboard which is a result of a cluster of particles being carried out from the bed in the central region (Figure 5.6).

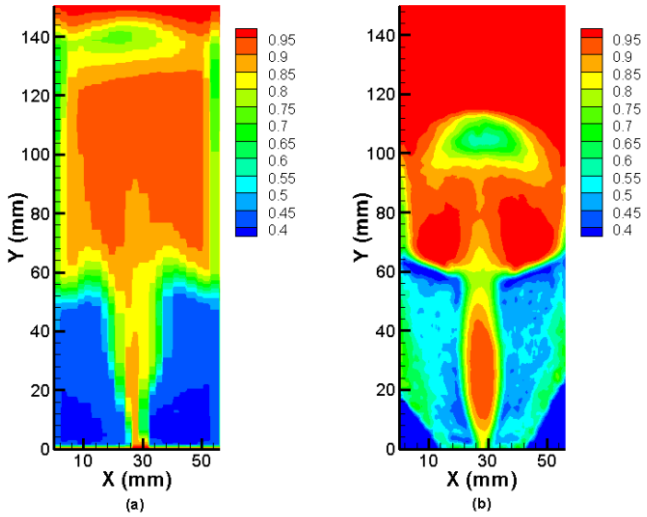

Figure 5.6: Void fraction contour plots for single jet and $3U_{mf}$ (a) DEM Simulation, (b) Experimental

The height to which the fountain rises is higher in the simulation as compared to the experiment. The main reason for this is the high drag force experienced by the central particles on increasing the fluidization velocity. Figure 5.7 shows the corresponding particle (solid) velocity in the domain.

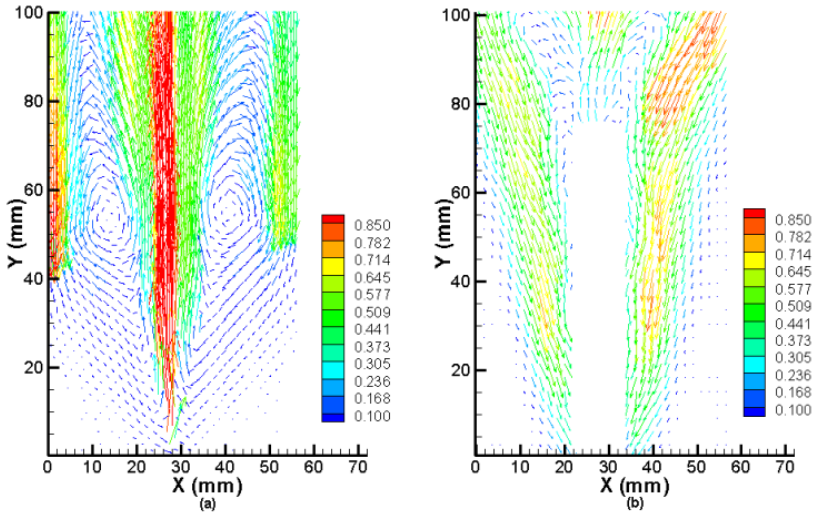

Figure 5.7: Particle velocity vectors for single jet and $3U_{mf}$ (a) DEM Simulation, (b) Experimental (Vectors are colored by velocity magnitude in m/s)

The particle velocity in the simulation shows two distinct particle recirculation zones along the jet. The central solid velocity has increased from about 0.55 m/s for 1.6 times the minimum fluidization velocity to about 0.85 m/s in this case. Figure 5.7(a) also shows

higher downward velocity of the particles closer to the walls and a smaller dead zone compared to the experiment. Again, we note that the experimental results are not consistent between Figure 5.6 and Figure 5.7. Figure 5.6 shows a high void fraction in the corners implying particle movement (a packed static bed would have a void fraction of approximately 0.4), whereas Figure 5.7 implies a large dead zone in the corners. The reason for this discrepancy in the experiments can be explained based on Figure 5.8.

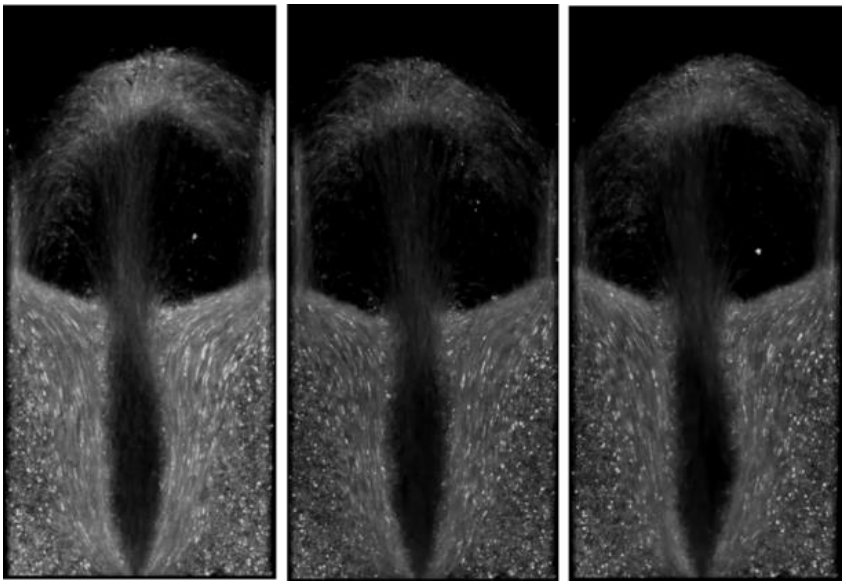

Figure 5.8: Snapshots of particle motion from experiment for single jet and $3U_{mf}$

Figure 5.8 shows snapshots of particle recirculation in the experiment. From Figure 5.8, it can be seen that no clear vortical recirculation occurs near the freeboard and the jet spout is straight without any swaying movement. This leads to a larger dead zone formation near the walls. Particles with high downward velocities fall down the bed along the sides of the jet. There exists a band of particles outside these higher velocity particles. The band of particles moves extremely slowly and dissipates the momentum of the faster particles. The extremely slow moving particles form a bridge between the faster moving particles and the particles in the dead zone region. The PIV resolution is not suited to capture these slow moving particles properly as there is a high velocity gradient across the slow moving band. The PIV detects these velocities as almost zero. This leads to a larger dead zone region based on particle velocity vectors as in Figure 5.7(b). The presence of solid particles with some amount of gas in the slow moving band is still

detected properly by the CCD camera. This leads to a slightly higher void fraction in that band compared to a static bed. But in essence, the void fraction plots show a smaller dead zone region compared to the velocity vectors as shown in Figure 5.6(b).

Figure 5.9 shows particle snapshots from the simulation. The spout formed in the simulation sways from side to side. This gives rise to vortical particle recirculation zones near the freeboard as shown in Figure 5.7(a). This also leads to greater momentum dispersion near the freeboard of the bed, thus giving rise to a wider spout.

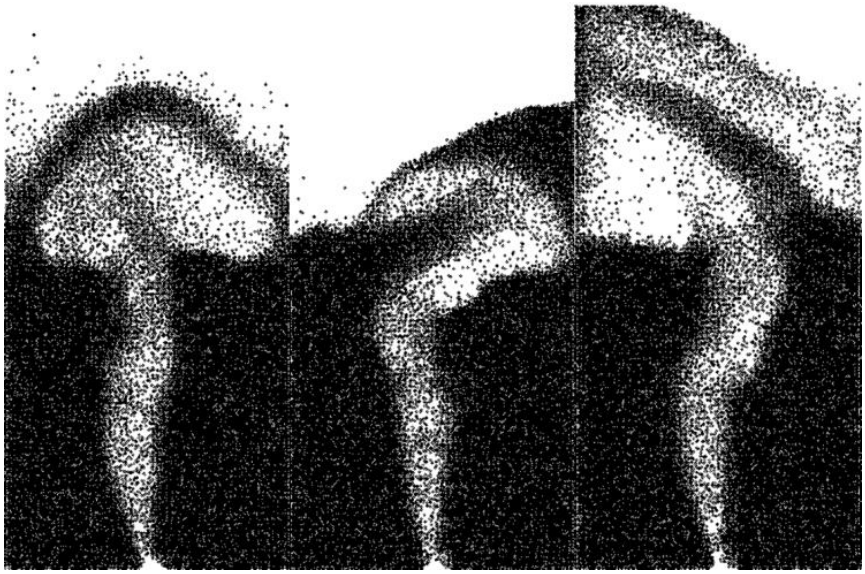

Figure 5.9: Snapshots of particle motion from simulation for single jet and $3U_{mf}$

To illustrate the effect of the friction coefficient, the friction between the particles and wall was changed from 0.1 to 0.5 for a fluidization velocity of 3 times the minimum fluidization.

From Figure 5.10, it is evident that the fountain height has come close to the experimental result on increasing the coefficient of friction for the wall-particle interactions. Comparing Figure 5.10(a) to Figure 5.6(a) demonstrates the influence of wall friction on the overall dynamics of a jetting fluidized bed. Clearly, the two grid scheme is able to capture these details where a single grid framework would have failed to produce any result. Figure 5.11 shows the particle (solid) velocity profile comparing the simulation with the experiment. There is an increase in the frictional resistance acting on the particles closer to the walls due to an increase in the coefficient of friction between the walls and the particles.

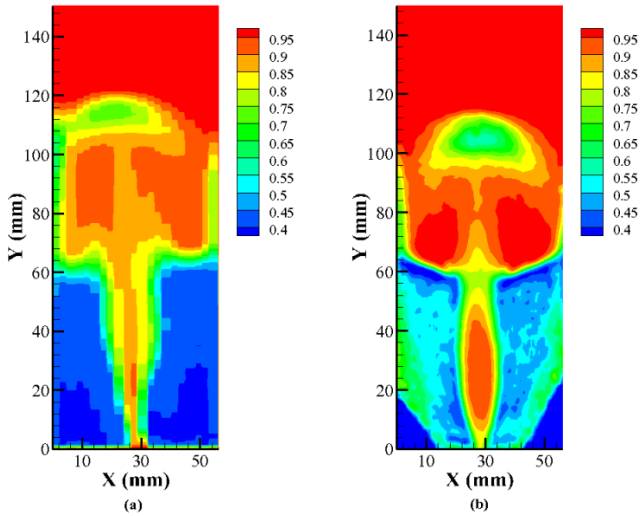

Figure 5.10: Void fraction contour plots for single jet and $3U_{mf}$ with higher coefficient of friction between the particles and walls (a) DEM Simulation, (b) Experimental

This results in limiting the movement of particles close to the walls which is evident by the increase in the area of the dead zone formation in Figure 5.11(a) compared to Figure 5.7(a). Particles tend to sweep along the walls falling down from the fountain to the bed. This phenomenon can be observed in both the simulations and the experiment. Although there has been a slight increase in the dead zone area with an increase in friction, the nature of particle recirculation stays the same as in the case with lower friction. The only major change has been the lowering of the fountain height for the higher friction case compared to the lower one. This happens because of an overall increase in the resistance for the particles to move up the bed. Figure 5.12 compares the velocity vectors between the simulations having low and high coefficients of wall friction. It is evident from the figure that the central particles move to a much higher height in the case of lower coefficient of friction due to an overall decrease in resistance. But the circulation characteristics remain similar in both the cases.

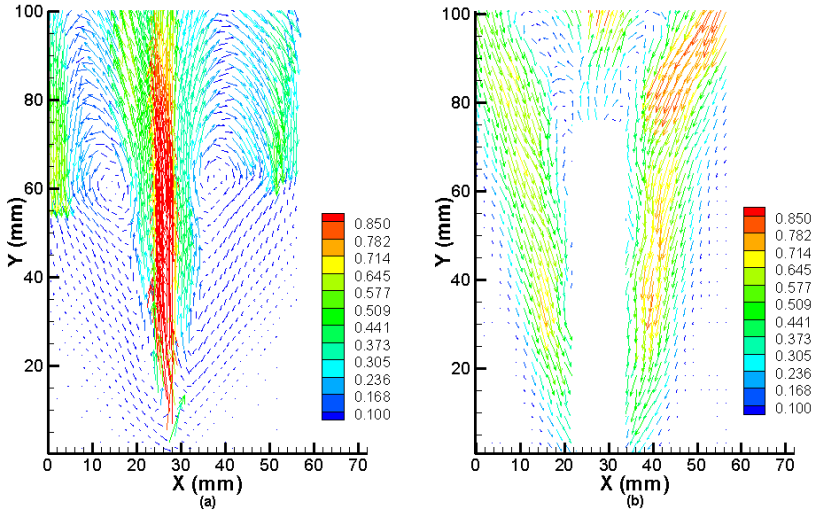

Figure 5.11: Particle velocity vectors for single jet and $3U_{mf}$ with higher coefficient of friction between the particles and walls (a) DEM Simulation, (b) Experimental (Vectors are colored by velocity magnitude in m/s)

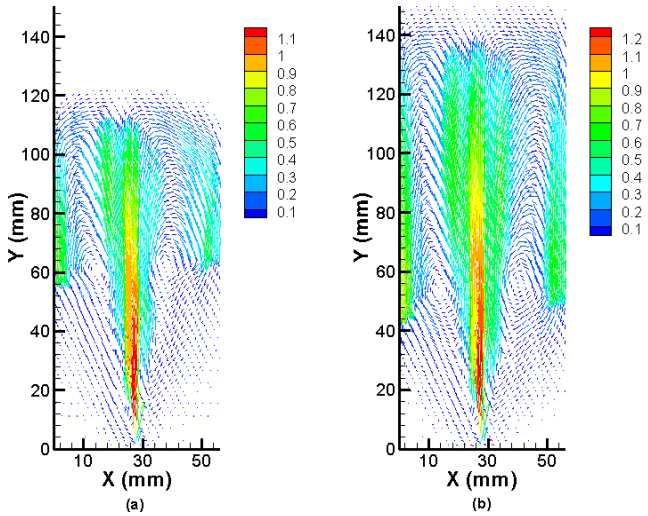

Figure 5.12: Comparison of particle velocity vectors for single jet and $3U_{mf}$ (a) Simulation with high coefficient of wall friction , (b) Simulation with low coefficient of wall friction (Vectors are colored by velocity magnitude in m/s)

Multiple Jets

The two grid scheme has been tested with multiple jets and compared to experimental results. Two different fluidization velocities of 1.6 and 3.0 times the minimum fluidization velocity have been used, but for brevity, only the higher fluidization results are shown in this chapter.

Double Jets

Figure 5.13 shows the void fraction field for the simulation and the experiment, respectively, for a fluidization velocity which is 3 times the minimum fluidization velocity.

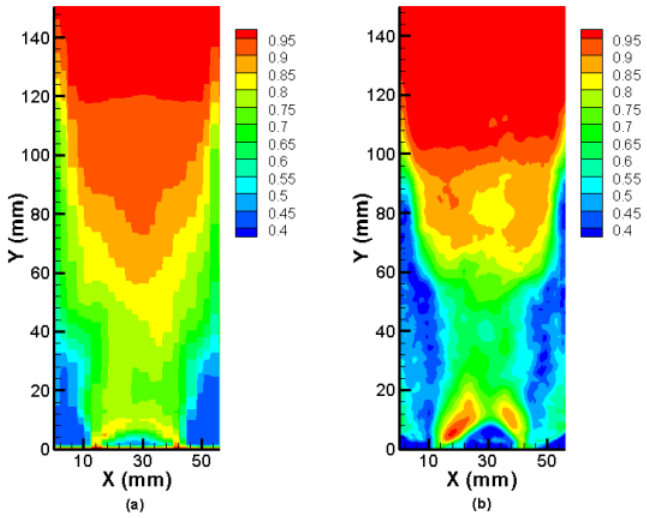

Figure 5.13: Void fraction contour plots for double jets and 3Umf (a) DEM Simulation, (b) Experimental

The simulation compares closely to the experimental result in showing the merging of the two jets near the distributor plate and forming a cup like void fraction structure near the center of the bed close to the freeboard. The horizontal dispersion of the void fraction field is slightly higher in the computation compared to the experiment. This might be due to the same effect of a higher wall friction coefficient in case of the experiment, which leads to a somewhat larger dead zone formation in the experiment compared to the simulation. No fountain formation can be seen in either the experiment or the simulation as the velocity of individual jets has halved and they merge near the distributor plate thus diffusing their momentum. But overall a fairly good agreement is obtained through the simulation using a two grid framework.

Triple Jets

Finally all the three jets have been tested out with the two grid framework and compared to experiment. Figure 5.14 shows the void fraction field for the simulation and

the experiment, respectively for a fluidization velocity which is 3 times the minimum fluidization velocity.

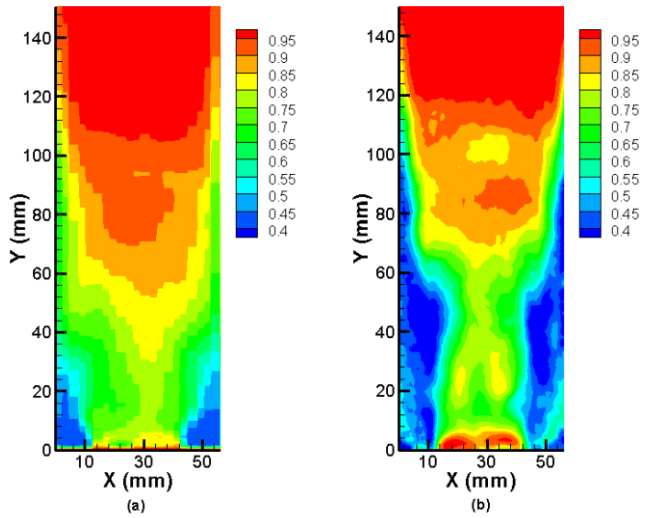

Figure 5.14: Void fraction contour plots for triple jets and 3Umf (a) DEM Simulation, (b) Experimental

Similar to the double jets, the triple jets setup also show that the jets merge very close to the distributor plate. The experiment show a streamlined channeling effect of the central particles flowing up the domain. The simulation shows a more dispersed effect. The height to which the particles rise along the wall compares well with the experiment.

Grid Sensitivity

A simple grid sensitivity analysis has been performed on the single jet case with higher wall friction. The superficial velocity is 3 times the minimum fluidization velocity. A rigorous grid sensitivity analysis is difficult to perform in a DEM-CFD framework, due to excessive computational time requirement. A coarser fluid grid having $105 \times 150 \times 3$ cells has been used to compare results with the finer grid having $175 \times 200 \times 5$ cells. The finer grid resolved the jet with 5 fluid cells along x direction, whereas the coarser grid has 3 fluid cells in the jet, along x direction. Figure 5.15 shows the void fraction profile for the two grid types. It can be seen that the void fraction profiles are similar for both the coarse and the fine grids. The height to which the fountain rises is close to 120 mm for both the coarse and the fine grids.

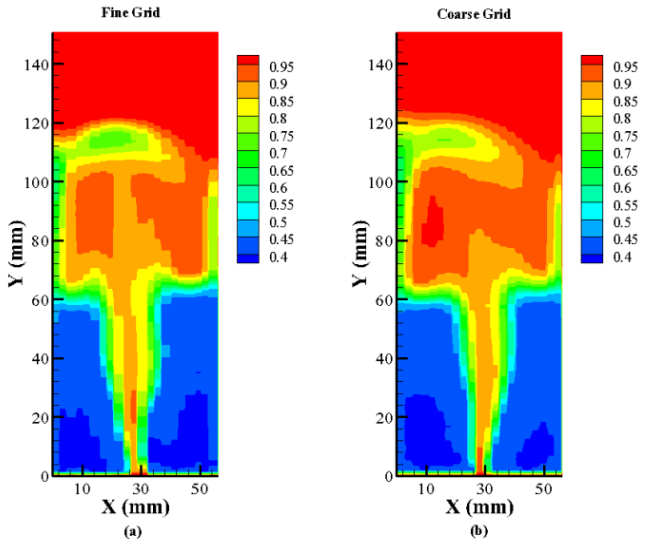

Figure 5.15: Void fraction contour plots for single jet and 3Umf (a) fine grid, (b) coarse grid

The void fraction just above the jet in the fine grid is small compared to the coarse grid, due to larger number of particles moving up because of the higher particle velocities in the jet center of the fine grid. Figure 5.16 shows the particle velocity vectors for the respective grids. It can be seen from Figure 5.16 that the jet center for the finer grid has higher particle velocities compared to the coarser grid. This is due to the higher resolution provided by the finer fluid grid, especially in the region of high particle velocities in the jet center.

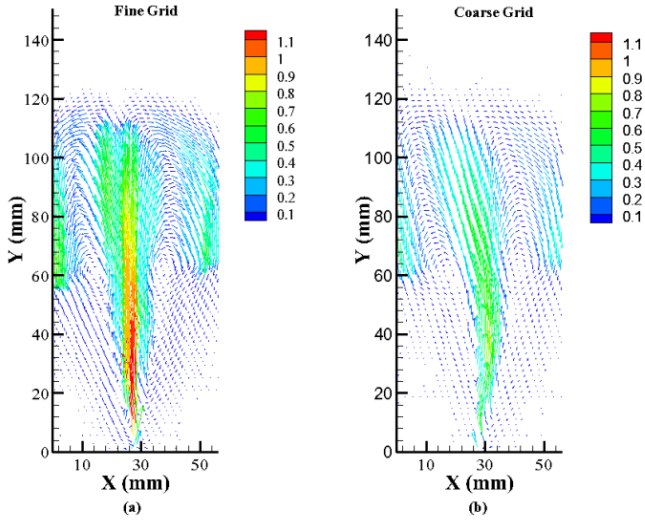

Figure 5.16: Particle velocity vectors for single jet and 3Umf (a) fine grid, (b) coarse grid

Summary and Conclusions

The commonly used single grid approach in coupled CFD-DEM calculations can limit the fluid flow resolution. To overcome this limitation, a novel two-grid method has been implemented and tested on jetting fluidized beds using the discrete element method. In this approach, the Eulerian field is calculated on a finely resolved fluid grid, whereas the particle field is evolved on a coarser grid more appropriate for the smooth variation of void fraction. Fluid field variables such as velocity and temperature are transferred from the fluid to the particle grid, and particle field variables such as the interphase transfer terms and void fractions are transferred to the fluid grid using suitable mappings.

The approach, by necessity, is tested in a jetting fluidized bed with particles of diameter $750\mu m$. A single-grid approach could not be used here due to the contradictory conditions posed on the grid size by the particles and the resolution of the jet. Two different superficial velocities of 1.6 and 3 times the minimum fluidization velocity are used. The two-grid scheme predicts a void fraction distribution similar to experiments for the single jet case with 1.6 times the minimum fluidization velocity. The bed height predicted is slightly higher than that of the experiment. Particle velocity vectors show two distinct counter rotating vortical structures in the simulation, which are the result of particles entrained in the jet moving up in the central region of the jet and falling down along the walls. For the $3U_{mf}$ and single jet case, DEM predicts a higher fountain height compared to the experiment. A calculation with a higher coefficient of friction between the walls and particles gives much better agreement of the predicted fountain height with the experiment. The dead zone areas along the walls increase with an increase in the wall friction. Overall, considering the uncertainty in experimental measurements, the predictions by the two-grid scheme are in agreement with experimental observations, particularly for multiple jets. A simple grid sensitivity study has been performed to show the effects of grid resolution on the void fraction and particle velocities. The finer grid shows higher particle velocities near jet center due to better resolution of the fluid field, but overall particle dynamics remain the same.

Chapter 6 Transient Heat Transfer Analysis

Introduction

Fluidized beds due to their vigorous mixing property and availability of large interfacial surface area for the particulate phase are highly suited for intensive heat and mass transfer operations. Applications of these beds are widespread in industries ranging from gasification, to catalytic pyrolysis and chemical processing (Jesse et al., 2005). This has resulted in an intense research initiative to find reliable models for capturing the essential heat transfer characteristics of a fluidized bed. A review of various mechanistic and empirical models have been given by (Yusuf et al., 2005). Mechanistic models are limited by the assumptions that they use while the empirical models are bound within the range of experimental data with which the model has been derived. Recent developments in the field of Computational Fluid Dynamics (CFD) allow researchers to apply full blown Navier- Stokes equations along with energy equations to capture complicated bed hydrodynamics as well as heat transfer characteristics, like bed to wall effective heat transfer coefficients and transient particle temperature distributions.

Several studies, both experimental and computational have been performed to investigate heat transfer characteristics of a fluidized bed. Early experimental studies on wall to bed heat transfer coefficients were carried out by (Klassen and Gishler, 1958; Petrovic and Thodos, 1968). An early attempt in developing a numerical scheme based on the concept of Two Fluids Model (TFM), where both the particles and the fluid are considered to be continuous and interpenetrating have been developed by (Kuipers et al., 1992). They were able to calculate the local wall to bed heat transfer coefficients without using any turbulence models. DEM has been used by (Kaneko et al., 1999) to model temperature behavior of gas and particles in a fluidized bed reactor for polyolefin. They used the Ranz-Marshall correlation to estimate heat transfer from particles to gas. Heat transfer characterization using DEM in pneumatic transport was performed by (Li and Mason, 2000). 2D calculations using 25000 Geldart group B particles to estimate the heat transfer coefficient on a circular probe were performed by (Di Maio et al., 2009). More recently, (Zhou et al., 2004) used a DEM-LES approach to model heat transfer and chemical kinetic reactions for coal combustion in a fluidized bed. Liquid fluidized beds

with heated walls have been investigated by (Malone and Xu, 2008) using large sized particles. In spite of a vast amount of work which has already been done in this field, proper heat transfer validation with lab scale experiments is lacking in literature.

The motivation for this proposed work lies in the need to have a detailed computational analysis of heat transfer characteristics and validate results with experiments inside a manageable lab scale setup. In-house lab scale experiments have been performed by (Brown, 2012). Availability of temperature and heat flux information at individual particle scale could be used to analyze heat transfer dynamics in the areas of the bed which are not accessible to the experiments. This will give us a more comprehensive picture of fluid-particulate heat transfer characteristics in a jetting fluidized bed. Two-grid framework has been used for the heat transfer analysis. The use of two-grid framework explained earlier would help in resolving the fluid field properly along with a finer resolution of the jets. The heat transfer coefficients are also expected to be predicted better than the single grid framework commonly used in DEM literature. The simulation performed in this study was aimed at testing out the two-grid formulation for heat transfer calculations. In order to do that, larger diameter particles of 750 μm in a 1.6 mm jetting fluidized bed setup have been used which would not be possible to simulate in a single grid framework. The data reduction and analysis for 750 μm particles have not been performed thoroughly in the experiment. This made it difficult to compare the computational results directly with the experiment.

Break up of Heat Transfer Analysis

The experiments performed by (Brown, 2012) highlight on two broad aspects of the heat transfer analysis as follows. These broad classifications have been laid down by (Kunii and Levenspiel, 1991) to reduce complexities involved in heat transfer analysis of a fluidized bed system.

- Investigating transient localized bed to wall heat flux distribution.
- Investigating transient temperature distribution of particles inside the bed.

A thermo-transient analysis has been done in the experiments by heating up the air entering the distributor plate using a temperature ramp as shown in Figure 6.1. Particle Image Velocimetry (PIV) and Digital Image Analysis (DIA) have been used to investigate

the bed hydrodynamics. The wall heat flux and particle temperature distribution have been captured using Infrared camera operating in the range of 7.5-13.0 μm (Brown, 2012).

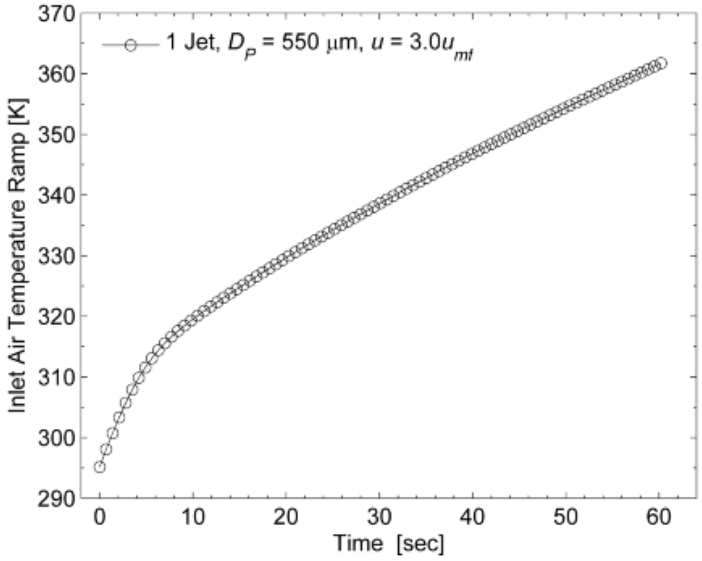

Figure 6.1: Transient inlet air temperature ramp for a single jet (Brown, 2012)

The computation investigates both the transient bed to wall heat flux and the transient particle temperature distribution. For calculating the transient localized heat flux distribution on the wall, a conjugate heat transfer model has been used.

Thermal DEM

Various modes of heat transfer manifests in a fluidized bed system. The particulate phase mainly experiences particle-particle heat conduction, conduction through the particle gaps to the surrounding gas (gas lens and liquid bridge effect), convective heat transfer with the surrounding gas, particle-wall conduction heat transfer, particle-particle/wall frictional heating and radiative heat transfer with the surrounding gas and bed walls. Heat transfer through radiation is significant for high temperatures (typically > 700 K). Details of the formulations for thermal DEM in our in-house code GenIDEST has been given in (Amritkar et al., 2012).

Computational Details

Figure 6.2 shows the bed geometry with dimensions $56.4mm \times 280mm \times 4.95mm$ in the x, y and z-directions, respectively. The centrally located two-dimensional jet (slit) is 1.6 mm wide and extends through the depth of the bed. The front wall of the bed has been made 1.52 μm thick in accordance with the experimental setup. The red arrow in the diagram represents the direction of view for DIA and PIV analysis in the experiments. In the computation, temperature variations of the external air has been considered in the domain marked as B. Domain B has the same size as domain A (the jetting fluidized bed). Conjugate heat transfer has been imposed on the front wall and suitable inlet boundary conditions have been imposed on the faces of the outer domain. These conditions together with heat transfer from the wall lead to natural convection being setup in the air contained inside domain B.

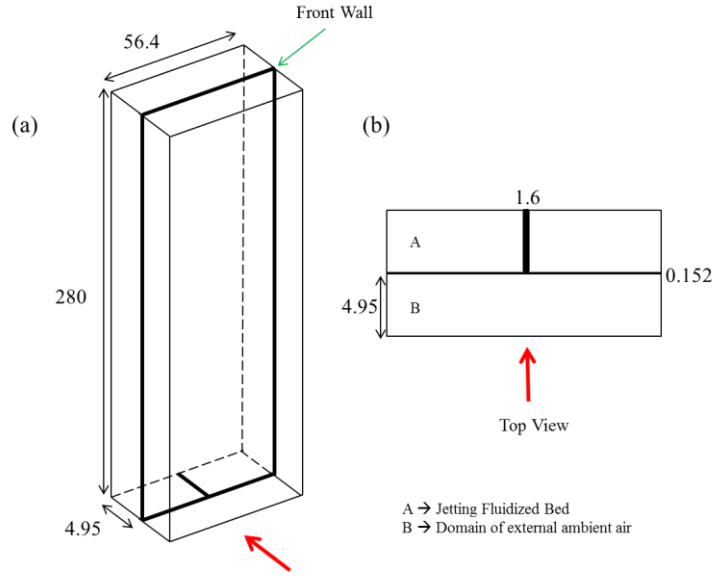

Figure 6.2: (a) Dimensions of the jetting fluidized bed (in mm), (b) Slit distribution on distributor plate

Details of jets

The slit is placed centrally for a single central jet. The width of the slit (jet) is 1.6 mm in the experiments and in the simulation. Superficial velocity of 3 times the minimum fluidization velocity has been used in the simulation.

Boundary conditions

For Domain A (Jetting fluidized bed)

No slip condition for the fluid phase has been imposed on all the walls of the bed. The jet velocity is set to 45.30 m/s (3 times the minimum fluidization velocity) as inlet boundary condition. A mass conserving uniform velocity profile is applied at the top outlet.

For Domain B (External ambient air)

The ambient air will heat up due to energy transfer from the wall. Due to this, a natural convection will set in and slow moving convective rolls of air would form. A Boussinesq approximation has been used where variations in density have been considered and the effect of that has been incorporated as a buoyancy source term in the Navier-Stokes equation. All the sides of the domain have been assigned a uniform velocity inlet boundary condition with extremely small velocities in all the directions to account for air flow inside the domain.

For the front wall

A conjugate heat transfer boundary condition has been applied to the front and back faces of the front wall. The wall having a thickness of 0.152 mm has been modeled using obstacles (solid regions inside fluid field, where N-S equations are not solved for). In a conjugate heat transfer problem, energy equation is solved both in the fluid as well as the solid sides. Continuity of heat flux at the wall surface from the fluid and the solid sides forms the boundary condition for a conjugate heat transfer problem as shown.

$$-k_s \left.\frac{\partial T}{\partial n}\right|_{w,s} = -k_f \left.\frac{\partial T}{\partial n}\right|_{w,f} \tag{6.1}$$

where, k_s, k_f and n are the thermal conductivities of the solid (wall), the fluid (air) and the surface normal to the wall surface, pointing outwards, respectively. All other walls have adiabatic boundary conditions in both the experiment and the simulation.

Grid Size

Both domains A and B have been discretized using $105 \times 150 \times 10$ fluid cells along the width, height and depth, respectively. Two-grid formulation (Deb and Tafti, 2013) has been used to resolve the fluid-particle interactions. The front wall, modeled as obstacles, has been discretized using $105 \times 150 \times 5$ cells.

Particle properties

Glass particles of 750 μm diameter with a density of 2500 kg/m^3 have been used in the simulation and the experiment. The particles fall in Geldart group D classification. The initial bed height is close to 60 mm and the number of particles is about 50,000 in both the experiment and the simulation. Table 6.1 lists the particle properties.

Table 6.1: Particle properties for heat transfer analysis

Diameter (μm)	Density (kg/m^3)	U_{mf} (m/s)	Number of particles
0.750	2500	0.43	50,000

DEM parameters for modeling collisions

The input parameters required for DEM to model inter particle collisions are the coefficient of restitution of particles during collision, the spring constants in both normal and tangential directions and the coefficient of friction between particles. The spring constants are considered to be the same in both normal and tangential directions. Standard values of coefficient of restitution and spring constants have been used in the present analysis. The same property values have been used for particle-wall interactions. Table 6.2 lists the parameters used for DEM.

Table 6.2: Parameters used in DEM for heat transfer analysis

Coefficient of restitution (e)	Coefficient of friction (μ)	Spring constant (k_n, k_t)
0.90	0.10, 0.50	800 N/m

Time step used

The maximum time step that can be used is restricted by the time scale of particle collisions. The critical time step for inter particle collision is based on (Tsuji et al., 1993) as follows

$$t_{cr} = \frac{\pi}{[k_n(1-\gamma^2)/m_{eff}]^{1/2}} \tag{6.2}$$

where γ denotes a constant given by

$$\gamma = \frac{-\ln(e)}{[\pi^2 + \{\ln(e)\}^2]^{1/2}} \tag{6.3}$$

m_{eff} is the effective mass or reduced mass of the colliding particle pair. Based on the above formulations, the critical time step comes out to be 5.838E-05 seconds for 750 μm particles. The time step used in the simulations is 1/10th of this critical value. The fluid and the particle time steps are kept the same.

Results and Discussion

Transient results till 8 seconds have been analyzed in the simulation and the experiment. The data reduction for the experimental runs has not been performed completely for the 750 μm case. This has prevented in a detailed comparison of the computational results with the experimental results. Nevertheless an effort has been made to simulate the complicated heat transfer process inside a jetting fluidized bed.

Particle Temperature Distribution

Figure 6.3 shows the transient evolution of particle temperature inside the bed obtained from the simulation. Particles entrained by the hot jet are heated as they are pushed upwards through the bed. These particles fall and gather near the walls and exchange heat with other particles through conduction and convection. Clear bands of low temperature particles could be seen at the dead zones surrounding the jet. These particles possess the minimum velocity and do not get entrained in the jet. As a result, they encounter a slow increase in their overall temperature due to conduction from neighboring particles.

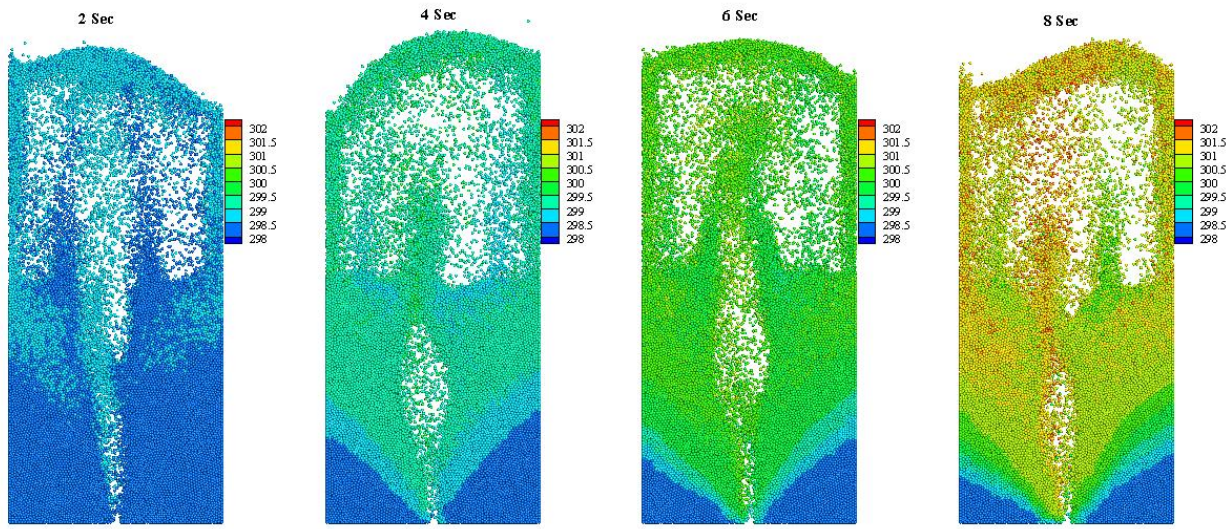

Figure 6.3: Transient particle temperature evolution inside the bed (K)

On the other hand, particles which directly encounter the heated jet gain energy through convection resulting in a rapid increase in their temperature. Due to lack of final experimental results for particle temperature evolution of 750 μm particles, only a qualitative comparison could be performed. Figure 6.4 shows the transient evolution of particle temperature in the experiment with 550 μm particles (Brown and Lattimer, 2013) .

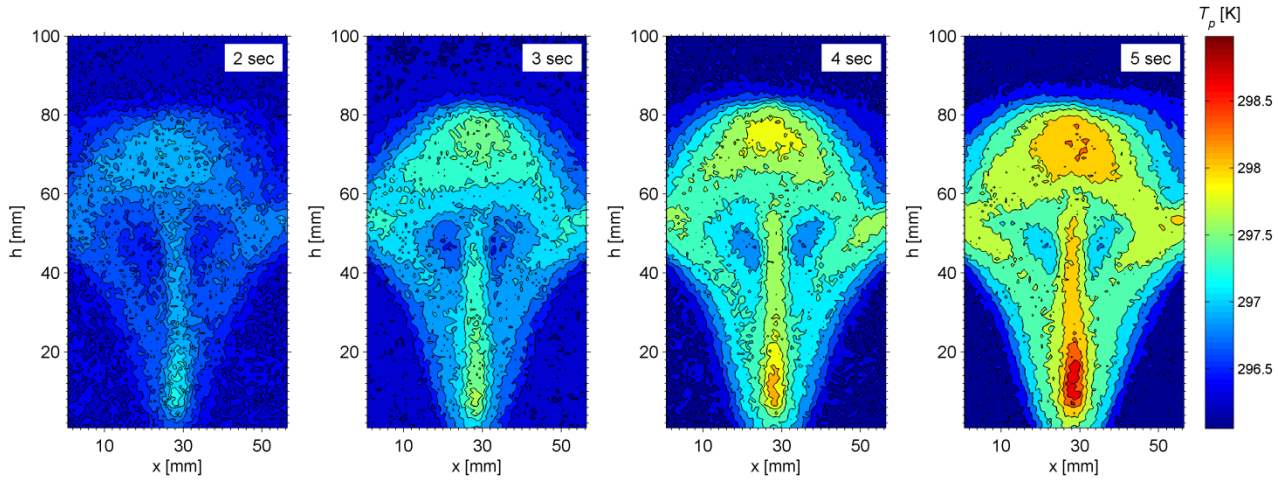

Figure 6.4: Transient particle temperature evolution obtained from experiment for 550 μm particles for 3 times the minimum fluidization velocity (Brown, 2012)

Figure 6.4 shows a fountain like structure close to what is seen in the simulation. A larger dead zone is observed in the experiment, but bands of heated particles near the

dead zones could be seen in the experiment as well. The differences in the dead zone area, the shape of the fountain and the magnitudes of the temperature between the experiment and the simulation are probably due to the two different conditions of the beds.

Wall Heat Flux Distribution

Figure 6.5 shows the transient heat flux distribution on the front wall obtained from the simulation. The fluxes predicted by the simulation are orders of magnitude smaller than the experimental result which is shown in Figure 6.6. This is because the temperature gradients near the wall are not getting resolved properly. A much finer grid is needed near the walls, or a relatively coarser grid with wall modeling strategy could be used. From the figure, it is clear that the wall heat flux is maximum at the center of the jet, with smaller values surrounding it. It could be also seen that the wall heat flux at the center of the jet becomes higher with time. This might be because of the time that it takes to set in the convective motion of the air outside the wall. Once the air is naturally convected, higher heat transfer would occur between the wall and the surrounding, thus giving rise to higher heat fluxes.

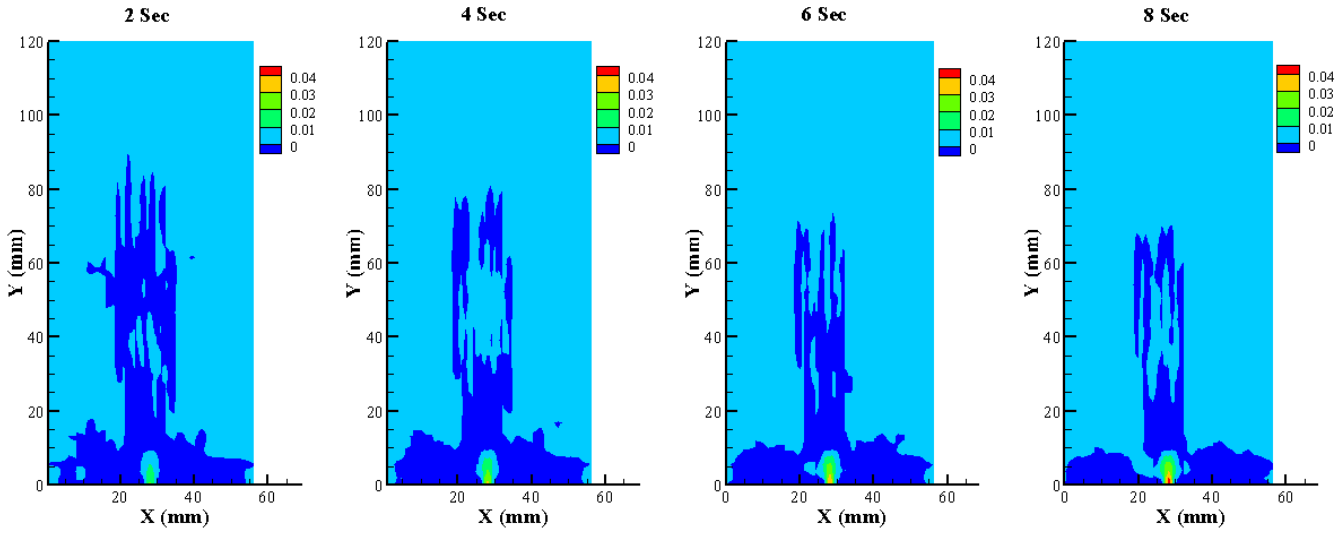

Figure 6.5: Transient wall heat flux distribution from simulation (W/m^2)

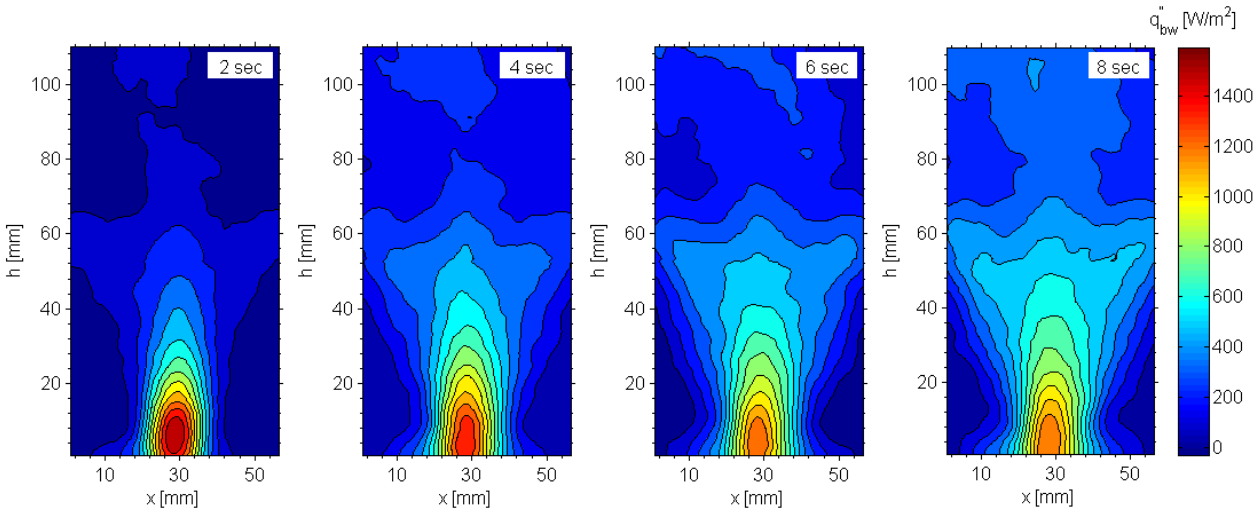

Figure 6.6: Transient wall heat flux distribution obtained from experiment for 750 μm particles for 3 times the minimum fluidization velocity (Brown, 2012)

Summary and Conclusions

This chapter focuses on the heat transfer characteristics of a jetting fluidized bed with a single central jet. Transient particle temperature distributions and transient wall heat flux distributions have been looked into. The particles falling inside the jet possess maximum temperature due to the combined effects of fluid convection and surrounding particle-particle conduction, whereas particles near the dead zones possess the minimum temperature due to a lack of convective effects in those regions. The particles in the dead zones fail to get entrained into the jet which prevents them from attaining high temperatures. The wall heat flux distributions show a high heat flux zone at the center of the jet, with lower values surrounding it. There is an increase of heat flux on the walls with time due to the convective effects of surrounding air outside the wall, which takes some time to set in. A rigorous analysis has not been done and there is enormous scope for improvements. A better wall heat flux prediction is guaranteed with finer mesh near the walls or with wall modeling approach. A lack of detailed experimental results also prevented critical comparisons between the results obtained from the simulation and the experiment. The aim of this chapter is to provide a base for performing complicated conjugate heat transfer simulations in future and improvements and modifications on this

base framework will lead to a more in-depth understanding and better prediction of transient heat transfer characteristics inside jetting fluidized beds.

Chapter 7 Conclusions and Future Scope

The main purpose of this work is to develop a robust framework for DEM-CFD modeling of granular flows. The present work focuses on the application of DEM-CFD framework in fluidized bed systems. The novelty of the work lies in the development and implementation of a two-grid framework for removing the contradictory resolution requirements of conventional DEM-CFD framework. Basic validations have been performed with experiments for both the conventional and the two-grid framework. The conclusions from the current work for each of the objectives put as separate chapters in the dissertation are presented below.

DEM Formulation and Validation

Discrete Element Modeling has been implemented in the in-house CFD solver GenIDLEST. Basic validation and verification checks have been performed with DEM (without CFD) to establish correct implementation. Next the coupled DEM-CFD framework has been used to simulate established experiments in literature. The computational results in terms of void fraction profiles and pressure fluctuations match well with the experimental results.

Investigation of flat bottomed spouted bed with multiple jets using DEM-CFD framework

A detailed numerical study using CFD-DEM has been performed on lab-scale flat spouted beds with single, double and triple jet configurations with different superficial velocities. Mixing in the beds has been analyzed using different criteria based on horizontal flux distributions, solid circulation rates using the counter-current model, and criterion based on power expended in convection and diffusion of solids. The single jet configuration with the higher superficial velocity showed the highest solid convective power as well as the highest solid diffusive power indicating a better overall solid circulation in the bed.

Discrete Element Modeling and Validation of Fluidized Bed with Multiple Jets

Two and three dimensional simulations of a jetting fluidized bed have been performed using the Discrete Element Method. Various results have been compared with experiment. The 2D results compare relatively well with the experiments close to the distributor plate which is essentially the jetting zone. On the other hand, a detailed 3D simulation is needed to capture the complex bubble dynamics occurring near the freeboard of the bed.

A Novel Two Grid Formulation for Fluid-Particle Systems using the Discrete Element Method

The commonly used single grid approach in coupled CFD-DEM calculations can limit the fluid flow resolution. To overcome this limitation, a novel two-grid method has been implemented and tested on jetting fluidized beds using the discrete element method. The approach, by necessity, is tested in a jetting fluidized bed with particles of diameter $750\mu m$. A single-grid approach could not be used here due to the contradictory conditions posed on the grid size by the particles and the resolution of the jet. The two-grid scheme predicts a void fraction distribution similar to experiments for the single jet case with 1.6 times the minimum fluidization velocity. Overall, considering the uncertainty in experimental measurements, the predictions by the two-grid scheme are in agreement with experimental observations, particularly for multiple jets.

Transient Heat Transfer Analysis

Transient particle temperature distributions and transient wall heat flux distributions have been looked into this chapter. The particles falling inside the jet possess maximum temperature due to the combined effects of fluid convection and surrounding particle-particle conduction, whereas particles near the dead zones possess the minimum temperature due to a lack of convective effects in those regions. The wall heat flux distributions show a high heat flux zone at the center of the jet, with lower values surrounding it.

Future Scope

One of the main future scope of this work lies in the application of the principal tools developed here in problems related to actual combustion of coal/biomass particles inside fluidized bed systems. Before such applications can be performed, chemical-kinetics model has to be incorporated in the present framework.

Some of the other future scope of this work are investigating the effects of fluid-particle turbulence in fluidized bed systems, performing detailed analysis of heat transfer in single and multiple jetting fluidized bed framework, investigating fundamental rheological properties of granular flows using the two-grid framework and analyzing the effects of fluid-particle drag correlations to come up with better drag models supporting experimental results.

Bibliography

Agarwal, G., Lattimer, B., 2011. Experimental Data on 9 jets in: Deb, S., Tafti, D. (Eds.), Private Communication ed, Blacksburg.

Agarwal, G., Lattimer, B., Ekkad, S., Vandsburger, U., 2011a. Experimental study on solid circulation in a multiple jet fluidized bed. Aiche J, Accepted for publication.

Agarwal, G., Lattimer, B., Ekkad, S., Vandsburger, U., 2011b. Influence of multiple gas inlet jets on fluidized bed hydrodynamics using Particle Image Velocimetry and Digital Image Analysis. Powder Technol. 214, 122-134.

Amritkar, A., Tafti, D.K., Deb, S., 2012. Particle Scale Heat Transfer Analysis in Rotary Kiln, Proceedings of the ASME 2012 Summer Heat Transfer Conference. ASME, Rio Grande, Puerto Rico.

Anderson, T.B., Jackson, R., 1967a. A fluid mechanical description of fluidized beds. Industrial and Engineering Chemistry Fundamentals. 6, 527-534.

Anderson, T.B., Jackson, R., 1967b. Fluid Mechanical Description of Fluidized Beds. Equations of Motion. Industrial & Engineering Chemistry Fundamentals 6, 527-539.

Basov, V.A., Markhevka, V.I., Melik-Akhnazarov, T.K., Orochko, D.I., 1969. Investigation of the structure of a nonuniform fluidized bed. Int. Chem. Eng. 9, 263-266.

Boemer, A., Qi, H., Renz, U., 1997. Eulerian simulation of bubble formation at a jet in a two-dimensional fluidized bed. Int J Multiphas Flow 23, 927-944.

Brown, L.S., 2012. Hydrodynamics and Transient Heat Transfer Characteristics in Fluidized and Spouted Beds Mechanical Engineering. Virginia Polytechnic Institute and State University, Blacksburg, VA.

Brown, L.S., Lattimer, Y.B., Unpublished results. Experimental Hydrodynamics of Multiple Jet Systems in a Fluidized and Spouted Bed. Int J Multiphas Flow submitted.

Brown, S.L., Lattimer, B.Y., 2013. Transient gas-to-particle heat transfer measurements in a spouted bed. Experimental Thermal and Fluid Science 44, 883-892.

Chapman, S., Cowling, T.G., 1970. The mathematical theory of non-uniform gases. Cambridge University Press.

Chiesa, M., Mathiesen, V., Melheim, J.A., Halvorsen, B., 2005. Numerical simulation of particulate flow by the Eulerian–Lagrangian and the Eulerian–Eulerian approach with application to a fluidized bed. Computers & Chemical Engineering 29, 291-304.

Cundall, P.A., Strack, O.D.L., 1979. Discrete Numerical-Model for Granular Assemblies. Geotechnique 29, 47-65.

Deb, S., Tafti, D.K., 2013. A novel two-grid formulation for fluid–particle systems using the discrete element method. Powder Technol. 246, 601-616.

Deen, N.G., Annaland, M.V., Van der Hoef, M.A., Kuipers, J.A.M., 2007. Review of discrete particle modeling of fluidized beds. Chem. Eng. Sci. 62, 28-44.

Di Maio, F.P., Di Renzo, A., Trevisan, D., 2009. Comparison of heat transfer models in DEM-CFD simulations of fluidized beds with an immersed probe. Powder Technol. 193, 257-265.

Enwald, H., Almstedt, A.E., 1999. Fluid dynamics of a pressurized fluidized bed: comparison between numerical solutions from two-fluid models and experimental results. Chem. Eng. Sci. 54, 329-342.

Epstein, N., Grace, J.R., 1997. Spouting of Particulate Solids, 2 ed. Chapman & Hall, New York.

Ergun, S., 1952. Fluid flow through packed columns. Chem. Eng. Prog. 48, 89.

Ettehadieh, B., Yang, W.-C., Haldipur, G.B., 1988. Motion of solids, jetting and bubbling dynamics in a large jetting fluidized bed. Powder Technol. 54, 243-254.

Farzaneh, M., Sasic, S., Almstedt, A.-E., Johnsson, F., Pallarès, D., 2011. A novel multigrid technique for Lagrangian modeling of fuel mixing in fluidized beds. Chem. Eng. Sci. 66, 5628-5637.

Feng, Y.Q., Xu, B.H., Zhang, S.J., Yu, A.B., Zulli, P., 2004. Discrete particle simulation of gas fluidization of particle mixtures. Aiche J 50, 1713-1728.

Feng, Y.Q., Yu, A.B., 2010. Effect of Bed Thickness on the Segregation Behavior of Particle Mixtures in a Gas Fluidized Bed. Ind. Eng. Chem. Res. 49, 3459-3468.

Geldart, D., 1986.

Gera, D., Gautam, M., Tsuji, Y., Kawaguchi, T., Tanaka, T., 1998. Computer simulation of bubbles in large-particle fluidized beds. Powder Technol. 98, 38-47.

Gidaspow, D., 1983. Fluidization in two-dimensional beds with a jet. 2. Hydrodynamic modeling. Ind Eng Chem Fundam. 22, 193-201.

Gidaspow, D., 1994. Multiphase Flow and Fluidization. Academic Press, San Diego.

Gidaspow, D., Jung, J., Singh, R.K., 2004. Hydrodynamics of fluidization using kinetic theory: an emerging paradigm: 2002 Flour-Daniel lecture. Powder Technol. 148, 123-141.

Gilbertson, M.A., Yates, J.G., 1996. The motion of particles near a bubble in a gas-fluidized bed. J. Fluid Mech. 323, 377-385.

Goldschmidt, M.J.V., Beetstra, R., Kuipers, J.A.M., 2004. Hydrodynamic modelling of dense gas-fluidised beds: comparison and validation of 3D discrete particle and continuum models. Powder Technol. 142, 23-47.

Guo, Q., Liu, Z., Zhang, J., 2000. Flow Characteristics in a Large Jetting Fluidized Bed with Two Nozzles. Ind. Eng. Chem. Res. 39, 746-751.

Guo, Q., Si, C., Zhang, J., 2010. Flow Characteristics in a Jetting Fluidized Bed with Acoustic Assistance. Ind. Eng. Chem. Res. 49, 7638-7645.

Guo, Q., Yue, G., Zhang, J., Liu, Z., 2001. Hydrodynamic characteristics of a two-dimensional jetting fluidized bed with binary mixtures. Chem. Eng. Sci. 56, 4685-4694.

Hoef van der, M.A., Sint Annaland van, M., Deen, N.G., Kuipers, J.A.M., 2008. Numerical Simulation of Dense Gas-Solid Fluidized Beds: A Multiscale Modeling Strategy. Annu Rev Fluid Mech 40, 47-70.

Hong, R.Y., Guo, Q.J., Luo, G.H., Zhang, J.Y., Ding, J., 2003. On the jet penetration height in fluidized beds with two vertical jets. Powder Technol. 133, 216-227.

Hoomans, B.P.B., Kuipers, J.A.M., Briels, W.J., van Swaaij, W.P.M., 1996. Discrete particle simulation of bubble and slug formation in a two-dimensional gas-fluidised bed: A hard-sphere approach. Chemical Engineering Science 51, 99-118.

Hoomans, B.P.B., Kuipers, J.A.M., Mohd Salleh, M.A., Stein, M., Seville, J.P.K., 2001. Experimental validation of granular dynamics simulations of gas-fluidised beds with homogenous in-flow conditions using Positron Emission Particle Tracking. Powder Technol. 116, 166-177.

Huang, C.-C., Chyang, C.-S., 1991. Gas Discharge Modes at a Single Nozzle in Two-Dimensional Fluidized Beds. Journal of Chemical Engineering of Japan 24, 633-639.

Huilin, L., Yurong, H., Gidaspow, D., Lidan, Y., Yukun, Q., 2003. Size segregation of binary mixture of solids in bubbling fluidized beds. Powder Technol. 134, 86-97.

Ishii, 1975. Thermo-Fluid Dynamic Theory of Two-Phase Flow. Eyrolles, Paris.

Iwadate, M., Horio, M., 1998. Agglomerating fluidization of wet powders and group C powders: a numerical analysis, in: Fan, L.S., Knowlton, T. (Eds.), Fluidization IX, Engineering Foundation, Durango, USA, p. 298.

Jesse, Z., Bo, L., Yi, C., John, G., 2005. Fluidized Beds, Multiphase Flow Handbook. CRC Press, pp. 5-1-5-93.

JJ, v.D., 1967. The counter-current flow model of a gas-solids fluidized bed, Proceedings of the International Symposium on Fluidization, Eindhoven, pp. 334–347.

Kafui, K.D., Thornton, C., Adams, M.J., 2002. Discrete particle-continuum fluid modelling of gas–solid fluidised beds. Chem. Eng. Sci. 57, 2395-2410.

Kaneko, Y., Shiojima, T., Horio, M., 1999. DEM simulation of fluidized beds for gas-phase olefin polymerization. Chem. Eng. Sci. 54, 5809-5821.

Kawaguchi, T., Kajiyama, S., Tanaka, T., Tsuji, Y., 2002. DEM Simulation of 2-D Fluidized Bed using Similarity Model, in: Cook, B.K., Jensen, R.P. (Eds.), 40647 ed. ASCE, Santa Fe, New Mexico, USA, pp. 30-30.

Kawaguchi, T., Sakamoto, M., Tanaka, T., Tsuji, Y., 2000. Quasi-three-dimensional numerical simulation of spouted beds in cylinder. Powder Technol. 109, 3-12.

Kawaguchi, T., Tanaka, T., Tsuji, Y., 1998. Numerical simulation of two-dimensional fluidized beds using the discrete element method (comparison between the two- and three-dimensional models). Powder Technol. 96, 129-138.

Kimura, T., Kojima, T., 1992. Numerical model for reactions in a jetting fluidized bed coal gasifier. Chem. Eng. Sci. 47, 2529-2534.

Klassen, J., Gishler, P.E., 1958. Heat transfer from column wall to bed in spouted fluidized and packed systems. The Canadian Journal of Chemical Engineering 36, 12-18.

Kobayashi, N., Yamazaki, R., Mori, S., 2000. A study on the behavior of bubbles and solids in bubbling fluidized beds. Powder Technol. 113, 327-344.

Konduri, R.K., Altwicker, E.R., Morgan Iii, M.H., 1999. Design and scale-up of a spouted-bed combustor. Chem. Eng. Sci. 54, 185-204.

Kuipers, J.A.M., Prins, W., Van Swaaij, W.P.M., 1992. Numerical calculation of wall-to-bed heat-transfer coefficients in gas-fluidized beds. Aiche J 38, 1079-1091.

Kuipers, J.A.M., Vanduin, K.J., Vanbeckum, F.P.H., Vanswaaij, W.P.M., 1993. Computer-Simulation of the Hydrodynamics of a 2-Dimensional Gas-Fluidized Bed. Comput Chem Eng 17, 839-858.

Kunii, D., Levenspiel, O., 1991. Fluidization Engineering. Butterworth-Heinemann, Boston.

Kuwagi, K., Mikami, T., Horio, M., 2000. Numerical simulation of metallic solid bridging particles in a fluidized bed at high temperature. Powder Technol. 109, 27-40.

Li, J., Mason, D.J., 2000. A computational investigation of transient heat transfer in pneumatic transport of granular particles. Powder Technol. 112, 273-282.

Limtrakul, S., Boonsrirat, A., Vatanatham, T., 2004. DEM modeling and simulation of a catalytic gas–solid fluidized bed reactor: a spouted bed as a case study. Chem. Eng. Sci. 59, 5225-5231.

Link, J., Zeilstra, C., Deen, N., Kuipers, H., 2004. Validation of a discrete particle model in a 2D spout-fluid bed using non-intrusive optical measuring techniques. Can J Chem Eng 82, 30-36.

Link, J.M., Cuypers, L.A., Deen, N.G., Kuipers, J.A.M., 2005. Flow regimes in a spout-fluid bed: a combined experimental and simulation study. Chemical Engineering Science 60, 3425-3442.

Link, J.M., Deen, N.G., Kuipers, J.A.M., Fan, X., Ingram, A., Parker, D.J., Wood, J., Seville, J.P.K., 2008. PEPT and discrete particle simulation study of spout-fluid bed regimes. Aiche J 54, 1189-1202.

Malone, K.F., Xu, B.H., 2008. Particle-scale simulation of heat transfer in liquid-fluidised beds. Powder Technol. 184, 189-204.

Mathur, K.B., Epstein, N., 1974. Spouted Bed. Academic Press, New York.

Merry, J.M.D., 1975. Penetration of vertical jets into fluidized beds. Aiche J 21, 507-510.

Mikami, T., Kamiya, H., Horio, M., 1998. Numerical simulation of cohesive powder behavior in a fluidized bed. Chem. Eng. Sci. 53, 1927-1940.

Morgan Iii, M.H., 1985. Spout voidage distribution, stability and particle circulation rates in spouted beds of coarse particles—I. Theory. Chem Eng Sci. 40, 1367-1377.

Moslemian, D., 1987. Study of Solids Motion, Mixing, and Heat Transfer in Gas-fluidized Beds. University of Illinois at Urbana-Champaign.

Mostoufi, N., Chaouki, J., 2001. Local solid mixing in gas–solid fluidized beds. Powder Technol. 114, 23-31.

Müller, C.R., Holland, D.J., Davidson, J.F., Dennis, J.S., Gladden, L.F., Hayhurst, A.N., Mantle, M.D., Sederman, A.J., 2009. Geometrical and hydrodynamical study of gas jets in packed and fluidized beds using magnetic resonance. The Canadian Journal of Chemical Engineering 87, 517-525.

Muller, C.R., Scott, S.A., Holland, D.J., Clarke, B.C., Sederman, A.J., Dennis, J.S., Gladden, L.F., 2009. Validation of a discrete element model using magnetic resonance measurements. Particuology 7, 297-306.

Pain, C.C., Mansoorzadeh, S., Gomes, J.L.M., de Oliveira, C.R.E., 2002. A numerical investigation of bubbling gas–solid fluidized bed dynamics in 2-D geometries. Powder Technol. 128, 56-77.

Patil, D.J., Annaland, M.V., Kuipers, J.A.M., 2005a. Critical comparison of hydrodynamic models for gas-solid fluidized beds - Part I: bubbling gas-solid fluidized beds operated with a jet. Chem. Eng. Sci. 60, 57-72.

Patil, D.J., van Sint Annaland, M., Kuipers, J.A.M., 2005b. Critical comparison of hydrodynamic models for gas–solid fluidized beds—Part II: freely bubbling gas–solid fluidized beds. Chem. Eng. Sci. 60, 73-84.

Peng, Z.B., Doroodchi, E., Evans, G., 2010. DEM simulation of aggregation of suspended nanoparticles. Powder Technol. 204, 91-102.

Petrovic, L.J., Thodos, G., 1968. Effectiveness factors for heat transfer in fluidized beds. The Canadian Journal of Chemical Engineering 46, 114-118.

Raghunathan, K., Mori, H., Whiting, W.B., 1988. A technique for measurement of jet penetration in hot fluidized beds with a modified Pitot-tube probe. Ind. Eng. Chem. Res. 27, 1011-1016.

Rees, A.C., Davidson, J.F., Dennis, J.S., S Fennell, P., Gladden, L.F., Hayhurst, A.N., Mantle, M.D., Müller, C.R., Sederman, A.J., 2006. The nature of the flow just above the perforated plate distributor of a gas-fluidised bed, as imaged using magnetic resonance. Chem. Eng. Sci. 61, 6002-6015.

Rong, D., Mikami, T., Horio, M., 1999. Particle and bubble movements around tubes immersed in fluidized beds – a numerical study. Chem. Eng. Sci. 54, 5737-5754.

Rowe, P.N., Partridge, B.A., 1965. An x-ray study of bubbles in fluidised beds. Transactions of the Institution of Chemical Engineers 43, 157-175.

Ruoyo, H., Hongzhong, L., Maoyu, C., Jiyu, Z., 1996. Numerical simulation and verification of a gas-solid jet fluidized bed. Powder Technol. 87, 73-81.

Shuyan, W., Huanpeng, L., Huilin, L., Wentie, L., Ding, J., Wei, L., 2005. Flow behavior of clusters in a riser simulated by direct simulation Monte Carlo method. Chem Eng J 106, 197-211.

Sun, J., Battaglia, F., Subramaniam, S., 2007. Hybrid Two-Fluid DEM Simulation of Gas-Solid Fluidized Beds. Journal of Fluids Engineering 129, 1394-1403.

Sutanto, W., Epstein, N., Grace, J.R., 1985. Hydrodynamics of spout-fluid beds. Powder Technol. 44, 205-212.

Swarbrick J, B.J.C., 1992. Fluid bed dryer, granulator and coaters, Encyclopedia of pharmaceutical technology. Marcel Dekker INC, New York.

Swasdisevi, T., Tanthapanichakoon, W., Charinpanitkul, T., Kawaguchi, T., Tanaka, T., Tsuji, Y., 2004. Investigation of Fluid and Coarse-Particle Dynamics in a Two-Dimensional Spouted Bed. Chem Eng Technol 27, 971-981.

Szafran, R.G., Kmiec, A., 2004. CFD Modeling of Heat and Mass Transfer in a Spouted Bed Dryer. Ind. Eng. Chem. Res. 43, 1113-1124.

Tafti, D.K., 2001. GenIDLEST - A scalable parallel computational tool for simulating complex turbulent flows., ASME-IMECE, American Society of Mechanical Engineers, New York, NY 10016–5990, United States, pp. 347–356.

Takeuchi, S., Wang, S., Rhodes, M., 2004. Discrete element simulation of a flat-bottomed spouted bed in the 3-D cylindrical coordinate system. Chemical Engineering Science 59, 3495-3504.

Toomey, R.D., Johnstone, H.F., 1952. Gaseous fluidization of solid particles. Chem Eng Prog 48, 220.

Tsuji, T., Chiba, T., Shibata, T., Uemaki, O., Itoh, H., 1999. Flow regime map for two dimensional spouted bed and comparison with simulation by discrete element method. Kag. Kog. Ronbunshu 25, 1037-1039.

Tsuji, Y., Kawaguchi, T., Tanaka, T., 1993. Discrete Particle Simulation of 2-Dimensional Fluidized-Bed. Powder Technol. 77, 79-87.

van Buijtenen, M.S., Buist, K., Deen, N.G., Kuipers, J.A.M., Leadbeater, T., Parker, D.J., 2012. Numerical and experimental study on spout elevation in spout-fluidized beds. Aiche J 58, 2524-2535.

van Buijtenen, M.S., van Dijk, W.-J., Deen, N.G., Kuipers, J.A.M., Leadbeater, T., Parker, D.J., 2011. Numerical and experimental study on multiple-spout fluidized beds. Chemical Engineering Science 66, 2368-2376.

van der Hoef, M.A., Annaland, M.V., Deen, N.G., Kuipers, J.A.M., 2008. Numerical simulation of dense gas-solid fluidized beds: A multiscale modeling strategy. Annu Rev Fluid Mech 40, 47-70.

Wen, C.Y., Deole, N.R., Chen, L.H., 1982. A study of jets in a 3-dimensional gas-fuidized bed. Powder Technol. 31, 175-184.

Wen, C.Y., Yu, Y.H., 1966. Mechanics of fluidization. Chem. Eng. Prog.Symp.Ser. 62, 100-111.

Wirsum, M., Fett, F., Iwanowa, N., Lukjanow, G., 2001. Particle mixing in bubbling fluidized beds of binary particle systems. Powder Technol. 120, 63-69.

Yang, W.-C., Ettehadieh, B., Haldipur, G.B., 1986. Solids circulation pattern and particles mixing in a large jetting fluidized bed. Aiche J 32, 1994-2001.

Yates, J.G., Rowe, P.N., Cheesman, D.J., 1984. Gas entry effects in fluidized bed reactors. Aiche J 30, 890-894.

Yusuf, R., Melaaen, M.C., Mathiesen, V., 2005. Convective Heat and Mass Transfer Modeling in Gas-Fluidized Beds. Chem Eng Technol 28, 13-24.

Zhang, K., Zhang, H., Lovick, J., Zhang, J., Zhang, B., 2002. Numerical Computation and Experimental Verification of the Jet Region in a Fluidized Bed. Ind. Eng. Chem. Res. 41, 3696-3704.

Zhang, Y., Jin, B., Zhong, W., 2008. Experimental Investigations on the effect of the tracer location on mixing in a spout-fluid bed. Int. J. Chem. React. Eng. 6, A46.

Zhang, Y., Jin, B., Zhong, W., 2009. Experiment on particle mixing in flat-bottom spout–fluid bed. Chemical Engineering and Processing: Process Intensification 48, 126-134.

Zhang, Y., Zhong, W., Jin, B., 2011. New method for the investigation of particle mixing dynamic in a spout-fluid bed. Powder Technol. 208, 702-712.

Zhao, X.L., Li, S.Q., Liu, G.Q., Yao, Q., Marshall, J.S., 2008. DEM simulation of the particle dynamics in two-dimensional spouted beds. Powder Technol. 184, 205-213.

Zhong, W., Xiao, R., Zhang, M., 2006. Experimental study of gas mixing in a spout-fluid bed. Aiche J 52, 924-930.

Zhong, W., Zhang, M., Jin, B., Zhang, Y., Xiao, R., Huang, Y., 2007. Experimental investigation of particle mixing behavior in a large spout–fluid bed. Chemical Engineering and Processing: Process Intensification 46, 990-995.

Zhou, H., Flamant, G., Gauthier, D., 2004. DEM-LES simulation of coal combustion in a bubbling fluidized bed Part II: coal combustion at the particle level. Chem. Eng. Sci. 59, 4205-4215.

Zhou, Z.Y., Kuang, S.B., Chu, K.W., Yu, A.B., 2010. Discrete particle simulation of particle-fluid flow: model formulations and their applicability. J. Fluid Mech. 661, 482-510.

Zhu, H.P., Zhou, Z.Y., Yang, R.Y., Yu, A.B., 2008. Discrete particle simulation of particulate systems: A review of major applications and findings. Chem. Eng. Sci. 63, 5728-5770.